WETTING OF ALUMINA-BASED CERAMICS BY ALUMINUM ALLOYS

Thomas Lebeau

Department of Mining and Metallurgical Engineering
McGill University
Montreal, Canada

December 1993

A thesis submitted to the Faculty of Graduate Studies and Research
in partial fulfilment of the requirements for
the degree of Master of Engineering

A Sophie, et à mes mères.

ABSTRACT

During the last 20 years, ceramic fiber reinforced metal matrix composites, referred to as MMCs, have provided relatively new way of strengthening metals. High specific modulus and a good fatigue resistance in dynamic loading conditions or for high temperature applications make these composites very attractive for replacing classic alloys. The first requirement for the fabrication of MMCs, especially by processes involving liquid metals, is a certain degree of wetting of fibers by the liquid metal which will permit a good bonding between the two phases.

The conventional experimental approach to wettability consists of measuring the contact angle of a drop of the liquid metal resting on flat substrate of the ceramic reinforcement materials.

This work deals with the fabrication of eutectic ZrO_2/Al_2O_3 (ZA), $ZrO_2/Al_2O_3/TiO_2$ (ZAT), and $ZrO_2/Al_2O_3/SiO_2$ (ZAS) ceramic substrates and the study of their wetting behavior by different classes of Al alloys. Wetting experiments were performed under high vacuum or under ultra high purity Ar atmosphere. Four major variables were tested to study the wetting behavior of the different ceramic/metal systems. Variables include holding time, melt temperature, alloy and ceramic compositions.

Ceramic materials were sintered under vacuum at temperatures ranging from 1500°C to 1790°C for 2.5 hours, and achieved over 96% of the theoretical density. An experimental set-up was designed to measure *in-situ* contact angles using the sessile drop method. For any ceramic substrate, a temperature over 950°C was necessary to observe an equilibrium wetting angle less than 90° with pure Al; by alloying the aluminum, wetting could be observed at lower temperatures (θ = 76-86° at 900°C for Al-10wt%Si, $\theta \sim 72°$ at 850°C for Al-2.4wt%Mg). Finally, ZAS specimens reacted with molten Al alloys over 900°C to produce Zr-Al based intermetallics at the metal/ceramic interface.

RÉSUMÉ

Au cours des 20 dernières années, les composites à matrice métallique et à renfort céramique se sont imposés comme un procédé relativement nouveau pour renforcer les alliages métalliques. Grâce à un haut module spécifique et une bonne résistance à la fatigue, ce matériau est voué à remplacer les alliages conventionnels dans le cadre d'utilisations en charge dynamique. Lors de la fabrication d'un tel composite, et en particulier pour les procédés d'élaboration par voie liquide, la première exigence est d'avoir un certain degré de mouillage de la fibre par le métal liquide pour permettre une bonne cohésion entre les deux phases.

Une approche conventionnelle pour les expériences de mouillabilité consiste à mesurer l'angle de contact d'une goutte de métal liquide reposant sur un substrat de céramique de la même nature que les fibres du matériau composite.

Cette thèse porte sur la fabrication de substrats de trois céramiques eutectiques (ZrO_2/Al_2O_3 (ZA), $ZrO_2/Al_2O_3/TiO_2$ (ZAT), $ZrO_2/Al_2O_3/SiO_2$ (ZAS)) et sur l'étude de leur comportement de mouillage par différentes catégories d'alliage d'aluminium. Les expériences de mouillage ont été pratiquées sous vide et sous Ar ultra pur. L'étude à porté sur l'effet de quatre paramètres expérimentaux principaux sur le comportement de mouillage de plusieurs systèmes métal/céramique: le temps de maintien en température, la température de fusion de l'alliage, la composition des alliages et des céramiques.

Les substrats de céramiques ont été frittés sous vide à des températures allant de 1500°C à 1790°C pendant 2.5 heures. Un dispositif expérimental fut conçu pour mesurer *in-situ* les angles de contact entre la goutte et le substrat. Quelque soit la nature du substrat, un angle de contact inférieur à 90° ne fut observé seulement qu'au dessus de 950°C avec de l'aluminium pur; en incorporant des éléments d'addition à l'aluminium, un comportement de mouillage fut observé à des températures moins élevées (θ = 76-86° à 900°C pour Al-Si10, θ~ 72° à 850°C pour Al-Mg2.4). Pour finir, des composés intermétalliques de type Zr-Al furent produits à l'interface ZAS/Al au-dessus de 900°C.

ACKNOWLEDGMENTS

I would like to express my sincere gratitude to Professor Robin Drew for his supervision, encouragement, and patience throughout the course of this thesis. I would also like to thank Professor John Strom-Olsen - and his group, "the people from physics up there"- for his co-supervision, and for the material facilities he offered me -and probably also for his sarcastic sense of humor which froze me during the first group meetings, and that I progressively and definitely appreciated with time-. I also wish to especially thank Professor John Gruzleski for his co-supervision and for having welcomed me from my very first contacts with McGill.

Special thanks go to H.Campbell, C.Edovas, M.Knoepfel, and all the machine shop personnel for their assistance and helpful technical support.

I would like to acknowledge Y. Baik for his assistance in many fields which were sometimes quite obscure to me, as well as D.Muscat, M.Entezarian, A.Hadian, and M.Allahverdi for their helpful suggestions which often enabled me to take one step ahead when I was on the edge of the abyss.

To all the members of the ceramic research group for their helpfulness and team-like disposition, and for having ignored me during my moments of mild madness in the office (in front of the computer).

Finally, I would like to thank L.Gavoret and E.Benguerel for their endless psychological support.

I have only two regrets:

I do not speak Maltese, Korean, and Persian even after two years of serious efforts.

I had to translate my abstract into French myself.

TABLE OF CONTENTS

LIST OF FIGURES

LIST OF TABLES

Chapter 1: INTRODUCTION

Over the past two decades, modern technology has given rise to an increasing need for new materials, espe· ially for dynamic structural applications where a high mechanical strength is no longer the only requirement; the efficiency of dynamic structures met in automotive, aircraft, or aerospace industries can be affected by an improvement in the structural efficiency of the materials.

One of the key properties in structural design is stiffness or rigidity. However, the stiffness and strength of a structure expand with the square of the linear dimension, whereas the weight increases with the cube of the linear dimension (square-cube relationship[1]). These structural considerations have therefore led to the search for new design techniques, and high-strength stiffer materials with tailored properties: composite materials.

Composites can be defined in many different ways. However, the definition can be restricted to materials that contain a reinforcement (fiber or particle) surrounded by a binding phase (matrix). The principle of reinforcing one material with particles or fibers of another is not new, and examples can be found both in early technology and in nature; e.g. bamboo made up of a low modulus plastic lignin matrix (E~7 GPa) tightly associated with high modulus cellulose filaments (E~25 GPa), is a composite material which exhibits amazing properties[2]. This natural example points out the main function of fiber reinforcement: load transfer from matrix to fibers.

Part of the most promising emerging materials, fiber reinforced metal matrix composites (MMCs) provide a relatively new way of strengthening metals. They have been under development since the early 1970s and are now reaching the point at which costs are decreasing; high volume industrial applications are for instance currently being developed for metal matrix composites to take advantage of the availability of relatively low cost, strong, high modulus ceramic fibers. A graphical comparison of the properties of these new materials with metals and alloys is given in Fig.1.1[3]; metal matrix composites and superalloys compete for the area of high temperature resistance, the former having higher specific strengths.

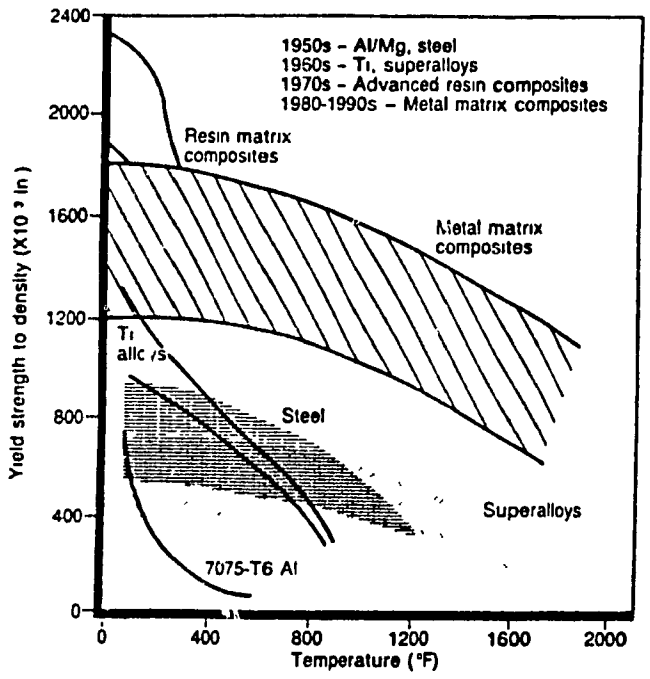

Fig. 1. Specific strength of fiber-reinforced composites and metals at elevated temperatures (1 in = 2.54 cm, T (°C) = (T (°F) − 32)/1.8)

Among metal matrix composites, fiber reinforced Al-alloys are receiving attention for possible structural applications ranging from automotive engine parts to missile structure, depending on the nature of the reinforcement (Table 1.1). Combined with various fibers, aluminum alloys, which provide matrices having high strength and quite high stiffness at low weight, can lead to a broad class of materials with good performance characteristics (Table 1.2).

Because of the high temperature resistance and high modulus value, Al_2O_3 based fibers represent the largest volume of production in the metal oxide fibers. Although there is a strong incentive to make aluminosilicate fibers with a high Al_2O_3 content, addition of one or two elements is often considered in order to

Table 1.1. Examples of Al matrix composite applications

Reinforcement	Applications
Carbon fiber	missile structures satellite, aircraft, bearing
B filaments, SiC, Borsic	turbine blades high temperature structures
SiC, Al_2O_3 fibers	high temperature structures engine parts (automotive)

Table 1.2. Densities, σ^R, and elastic modulus of ceramic fiber reinforced aluminum composites (Vf= 0.5)

Matrix	Reinforcement	d ($g.cm^{-3}$)	σ^R (MPa)	E (GPa)
Al	C fibers	2.25	1515	224
	SiC fibers	2.63	1240	130
	Al_2O_3 (FP)	3.3	875	220
	B filament	2.5	2015	234
	SiC filament	3	2065	248
Al	--	2.7	80	67.5
Al-7Si-0.6Mg	--	2.7	340	74

modify the fiber microstructure, to improve particular intrinsic properties (Table 1.3), or to allow the process of the fiber using a specific technique. Therefore, addition of SiO_2 will enable fiber fabrication by spinning processes; adding ZrO_2 will lead to a finer microstructure of the ceramic, whereas small Cr_2O_3 additions improve the temperature resistance of the fibers. Eutectic amorphous zirconia/alumina (ZA), zirconia/alumina/titania (ZAT), and zirconia/alumina/silica (ZAS) fibers are in fact currently being developed and produced by melt extraction with a view to fabricating aluminum alloy matrix composites.

Table 1.3. Melting points and use temperatures of inorganic fibers (after ref.[3])

Fiber type	Melting point (°C)	Maximum use temperature (°C)	
		Oxidizing atmosphere	Non-oxidizing atmosphere
B	1200	560	1200
SiO_2	1660	1060	1060
Al_2O_3-SiO_2-B_2O_3	1740	1427	1427
Al_2O_3-SiO_2	1760	1300	1300
Al_2O_3	2040	1540	1600
ZrO_2	2650	1650	1650
SiC	2690	1800	1800

One of the most widespread casting methods used for the fabrication of such a composite is the squeeze casting process[4]. During squeeze-casting, the compatibility of reinforcing materials and matrix alloys is of primary importance and is needed to generate a strong enough interface to allow load transfer from the matrix to the reinforcements without failure. There is therefore a demand for methods to evaluate factors such as wettability and reactivity between the melt and the fiber. Sessile drop experiments can be used to determine the relative interfacial energies for a liquid aluminum drop on the ceramic solid surface, and measurement of the contact angle of the drop as a function of time, temperature, atmosphere etc., shows the influence of process parameters on wetting.

However, the wettabilities of ceramic materials with liquid aluminum alloys are generally poor (contact angles significantly higher than 90° (non-wetting) even well above the matrix melting temperature). For such systems, application of pressure alone is not sufficient to overcome poor wettability, and a large number of attempts have been made at designing solutions to enhance the wetting of the ceramic phase by the metal phase. These can be classified in three broad categories: reinforcement pretreatment, alloying modifications of the matrix, modification of the reinforcement[5].

The objective of this work was to study the wetting behavior of ZA, ZAT, and ZAS ceramic materials with various aluminum alloys and to design the optimum experimental parameters for potential composite fabrication. The following Chapter reviews the background science and literature of fiber reinforced metal matrix composites including their fabrication and engineering properties, and a concise view on the principle of fiber reinforcement. Then, theoretical mechanisms of wetting are introduced and the influence of several parameters on the ceramic/metal system behavior is discussed. Finally, a literature survey related to ZA, ZAT, and ZAS ceramic fabrication and intrinsic properties is presented.

Based on the literature review, a number of objectives were chosen (Chapter 3). The results of this research are divided in two main sections; the first part is related to the ceramic substrates, while the second one deals with the wetting behavior of several metal/ceramic systems (Chapter 5).

Chapter 2:
LITERATURE REVIEW

2.1 FIBER REINFORCED METAL MATRIX COMPOSITES

Metal matrix composites have potential as structural materials at high temperatures. Fiber reinforcement of Al and Mg alloys is expected to improve their stiffness and strength enough to replace classic engineering alloys in dynamic structural applications, thereby reducing weight, inertia and vibration. Prototype automotive parts such as connecting rods or diesel pistons have been manufactured from Al-alloys reinforced with various types of fibers[6,7]. In the case of the diesel piston for example, the local composite reinforcement of the ring groove exhibits wear resistance and dimensional stability comparable with the Ni-Resist alloy inserts used currently, and has the added benefits of easier production, lower weight and improved thermal conductivity.

Metal matrix composites have a series of requirements which are similar to those of conventional alloys currently used in dynamic engineering structures. They include the combination of the following properties:

1. high strength;
2. high modulus;
3. high toughness and impact properties;
4. low sensitivity to changes in temperature or thermal shock;

5. high electrical and thermal conductivity;
6. excellent reproducibility of properties.

Fiber reinforced composites contain reinforcements having lengths greater than their cross-sectional dimensions. Such a composite is considered to be a discontinuous fiber or short fiber composite if its properties vary with fiber length[8]. On the other hand, a composite is considered to be continuous fiber reinforced when it contains fibers that are comparable in length to the overall dimensions of the composite part.

A classification of fiber composite microstructure in terms of geometry can be considered. The main classes can be identified as long-parallel fiber, short-parallel fiber, long-random fiber and short-random fiber, as well as combinations of these[9] . The fiber diameter is also significant, mainly because of its influence on certain properties. The main categories of composite microstructure geometries are shown in Fig.2.1.

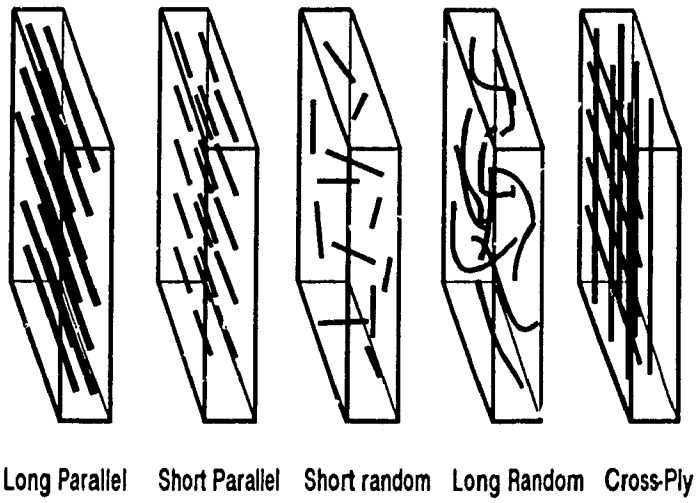

Figure 2.1. Classification of fiber composite microstructure geometries.

2.1.1 Unidirectional Reinforcements: a Simple Example of the Rule of Mixture

The fiber arrangement in the matrix has a great influence on the final properties of the composite. The most spectacular properties are obtained in the fiber direction of a long parallel fiber reinforced composite. A simple expression can be used to relate composite strength to constituent properties[10]:

$$\sigma^*_c = \sigma_f \cdot V_f + \sigma_m \cdot V_m \qquad (2.1)$$

where σ_c^* is the ultimate strength of the composite expressed as a stress based on the original area, σ_f is the average stress on all the fibers, and σ_m is the average stress on the matrix at failure. V_f and V_m are the volume fractions of fibers and matrix. If there is no porosity or third phase, $V_m + V_f = 1$. This equation or "rule of mixture" is only a simplified analysis of stress distribution in an unidirectional composite loaded parallel to the fiber direction. However, in the same way, it is possible to get the same kind of equation for the Poisson ratio, ν, for example:

$$\nu_c = \nu_f \cdot V_f + \nu_m \cdot V_m \qquad (2.2)$$

As well as for the Young's modulus E, which can be described by:

$$E_c = E_f \cdot V_f + E_m \cdot V_m \qquad (2.3)$$

Equations (2.1), (2.2), and (2.3) do not describe the case of a low fiber volume fraction, where the matrix is predominating in the composite. In this case, the fibers are dispersed and do not act as a reinforcement. When fracture occurs, Fig.2.2 shows that the curve σ_c vs V_f cuts the Y-axis (at $V_f=0$) for a stress equal to σ_m. The rule of mixture describes the composite behavior as driven by the fibers, but the fiber failure strain is significantly lower than that of the matrix. Therefore, σ_m is

not the matrix failure strain σ_{mf}, but the one which corresponds to the fibers failure strain. For lower fiber volume fractions, the stress vs strain curve for the composite is given by: $\sigma_{cf} = \sigma_{mf}.V_m$. Therefore, the fibers act as a reinforcement when the volume fraction V_f is greater than a critical fiber volume fraction V_{fmin}.

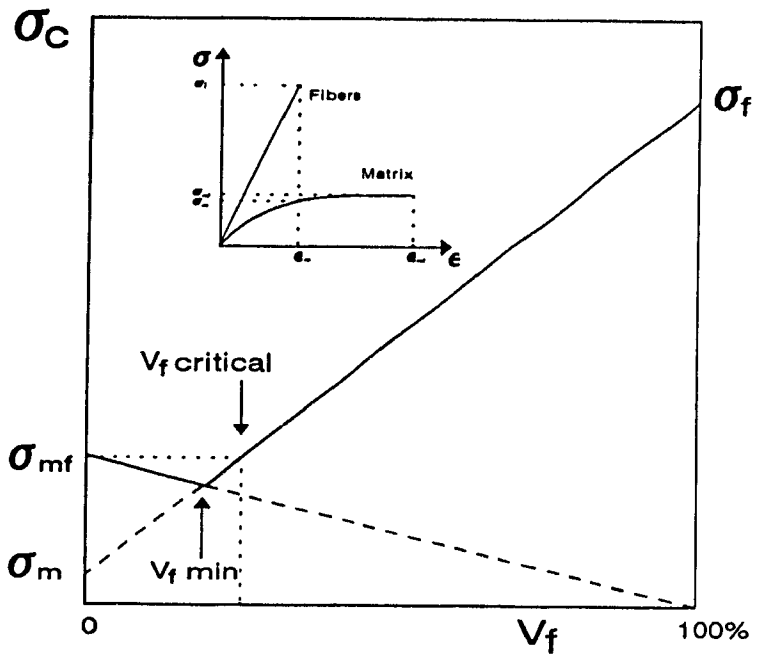

Figure 2.2. Rule of mixture for a continuous fiber composite.

2.1.2 Load Transfer and Ductile Matrix Composite Failure

When a composite containing uniaxially aligned fibers is stressed in a direction parallel to the fibers, the axial displacement in the fiber and matrix are different because of the difference in elastic moduli. The difference between the axial displacement of the fiber and the matrix leads to shear strains produced in the matrix on all planes parallel to the axis of fibers. This shear strain is the mechanism by which the tensile loads supported by fiber and matrix are distributed between the two components. For this concept, it is assumed that each fiber is embedded in a

continuous matrix with an excellent fiber/matrix bonding.

The stress is applied to the fiber by shear stresses at the interface:

$$\frac{dP}{dz} = 2\pi r_0 \tau_{rz(r=r_0)} \tag{2.4}$$

where P is the tensile load on the fiber of radius r_0 and τ_{rz}, evaluated at the surface of the fiber, is a function of r and z (Fig.2.3). P is $\sigma_{zz}\pi r_o^2$ for a thin fiber[11].

The load builds up linearly from the ends with a constant shear stress. In the case of discontinuous fiber composites, a minimum critical reinforcement length can be defined at which stresses can be built up high enough to break the fibers:

$$l_c = \frac{r_0 \sigma}{\tau} \tag{2.5}$$

The length $l_c/2$ is defined as the transfer length. The value of l_c depends on τ. For a plastic matrix, τ is constant. If the interface fails, τ is equal to the frictional force per unit area produced by the fiber pull-out. For a work-hardening matrix, the value of τ depends upon the plastic strain in the matrix.

In the case of a ductile matrix, such as aluminum or magnesium, when the fiber length $l<l_c$, failure of the composite must occur by plastic flow of the matrix. When the fiber length $l>l_c$, failure occurs when the fibers fail.

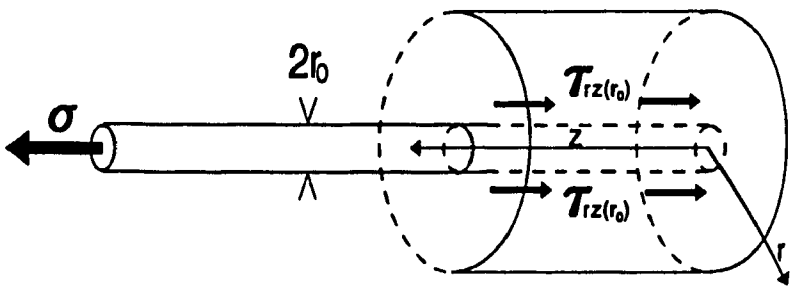

Figure 2.3. Force acting on a reinforcing fiber.

The strength of the composite is thus directly related to the strength of the fibers and the quality of the interface. When fibers fracture, the strength is decreased by the load-carrying ability of the broken fiber, at the location of the filament break[12].

The stress concentration effect around broken fiber ends can also lower the effective strength of the composite. One of the important assets of composite materials is that a crack propagating normal to the applied tensile load can be stopped at the fiber-matrix interface; the maximum stress induced at the crack tip in the matrix is approximately equal to the ultimate strength of the matrix, which is low compared to the fiber-breaking stresses. This crack blunting phenomenon is described in Fig.2.4.

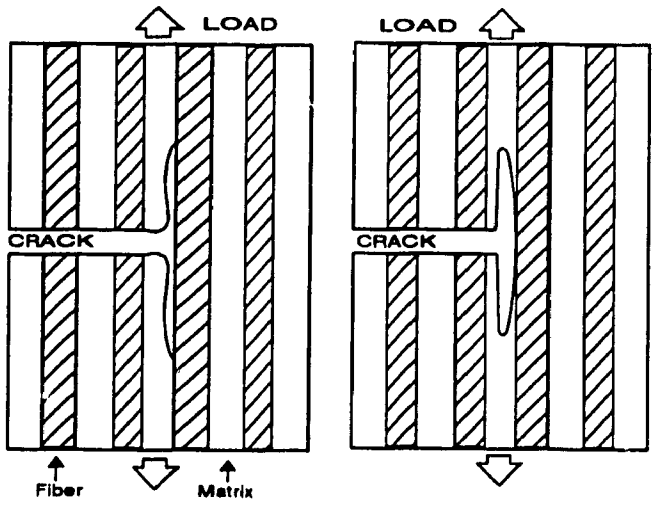

Figure 2.4. Crack blunting: (a) interfacial splitting; (b) matrix shear deformation and splitting

However, local stress concentrations due to the crack tip are significant; the broken fiber ends exert shear stresses on the matrix as they contract, which are supported by the neighbor fibers, since they cannot be sustained by the ductile matrix itself. These local additional tensile forces can lead to unstable crack growth[1].

The stress state of the composite is eventually modified by the shock wave generated by fiber fracture. The dynamic fracture energy is absorbed by a soft aluminum matrix for example. However, the energy release has not been treated quantitatively in the literature with respect to its effect on the strength of the composite.

Fig. 2.5 summarizes the failure modes of unidirectional composite subjected to longitudinal tensile load[13]. In a continuous fiber reinforced composite, the fiber provides all of the load-carrying characteristics of the composite, the most important of which are strength and stiffness. Because of the presence of multiple fibers, the composite is a very reliable material; the failure of even several fibers results in the redistribution of load onto other fibers as well as plastic deformation of the matrix rather than a dramatic failure of the part.

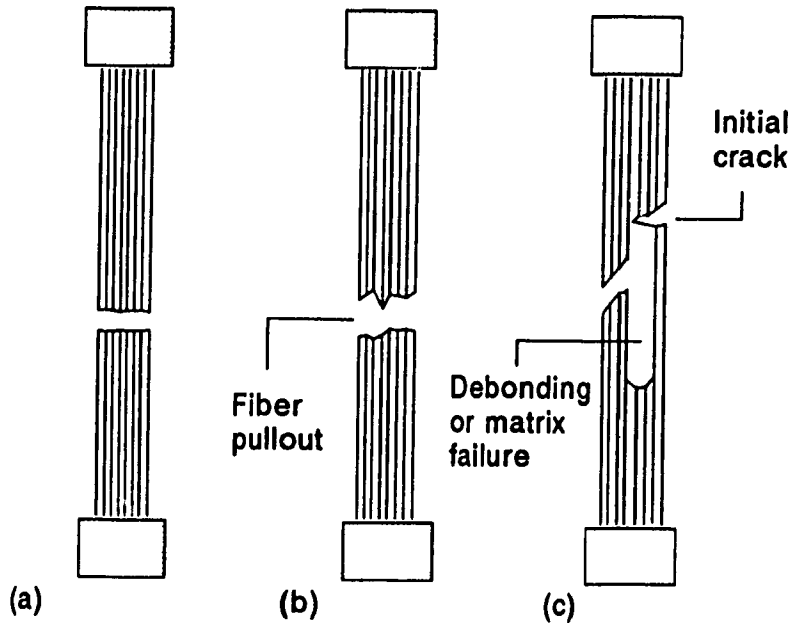

Figure 2.5. (a) brittle failure; (b) brittle failure with fiber pull-out; (c) brittle failure with debonding and/or matrix failure.

2.1.3 Fiber Production Methods

Fibers can be produced by several different techniques which to a large extent determine the form, microstructure and properties of the fiber. Certain inorganic fibers such as SiC fibers can be produced by first preparing a precursor fiber of a suitable polymer and then burning this under controlled conditions (pyrolysis). By this method the fibers are produced as many hundred parallel fibers with diameters around 10 μm in a continuous yarn[14].

Many other methods are used for ceramic fiber fabrication[3], including:

1. rod drawing, as practised in making wires;
2. passage through an orifice (melt spun fibers);
3. vapor deposition;
4. crystal growth from a melt solution or by the vapor-liquid-solid technique;
5. melt extraction.

Commercial Alumina and Alumina based Fibers: The metal oxide fibers produced in the largest volume are those composed of Al_2O_3 and SiO_2. One category of these fibers is known as Aluminosilicate fibers, which can be divided into those containing 45 to 60% of Al_2O_3, which can be melt spun, and those of higher Al_2O_3 content, which cannot be melt spun because of the high melting point and low viscosity of Al_2O_3.

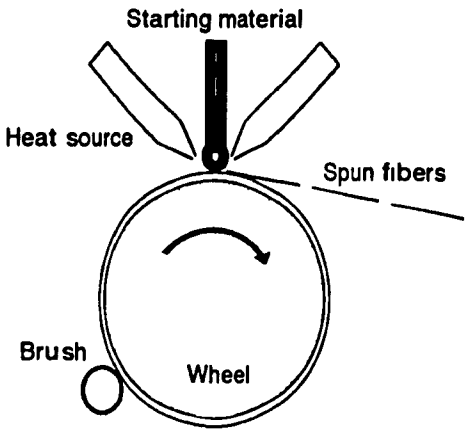

Figure 2.6. Schematic of melt spinning process.

The blowing process involves pouring the molten material into the path of a high velocity blast of air, which shreds the molten oxide into small droplets. The droplets elongate to a tear-drop shape and attenuate into a fiber[11]. During the spinning process, the molten material is fed

onto a vertically oriented, rapidly rotating disk from which fibers are thrown by centrifugal force. Fig.2.6 illustrates the melt spinning technique. Both the spun and blown processes produce a wide range of fiber diameters in the 1μm to 10μm range. Fiber lengths vary from 1cm to several centimeters.

A high Al_2O_3 content in the fibers is usually required for higher temperature resistance and higher modulus values, which makes them attractive for use in metal matrix composites. Table 2.1[15] shows that a SiO_2 containing fiber has greater tensile strength than a 99% pure Al_2O_3 fiber, but that the elastic modulus is lower. However, some additives such as ZrO_2 can improve the fiber properties but the high melting point and low viscosity of molten Al_2O_3 preclude processes such as

Table 2.1. Comparison of Al_2O_3/SiO_2 and Al_2O_3 fibers.

Characteristics	Fiber	
Composition (wt%)	Al_2O_3/15%SiO_2	> 99% Al_2O_3
Tensile Strength (MPa)	1590-2550	1550
Modulus (GPa)	200-248	379
Elongation (%)	0.8-1	0.4

melt spinning. *Du Pont de Nemours* have produced $Al_2O_3$80%-$ZrO_2$20% fibers which have about 50% greater tensile strength than conventional Al_2O_3 fibers, with a smaller grain size and which degrade less upon exposure to high temperatures.These fibers have been produced by the slurry process, as described in Fig.2.7[16]. The plasticized fiber is spun and then passed through a 300°C to 800°C oven to remove the polymer and calcine it. The fiber is then sintered at temperatures up to 1800°C.

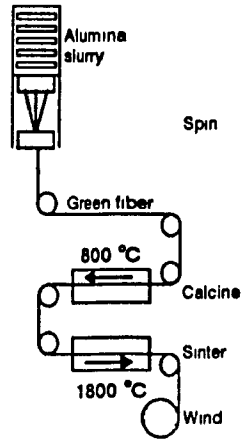

Fig. 2.7. Fiber FP process.

Outstanding physical and mechanical properties can be achieved with amorphous ceramic fibers, especially a very high tensile strength. The absence of shrinkage and porosity characterizes this category of fibers which show almost the same density as in the liquid state. Such fibers are mainly produced by sol-gel techniques[17,18]. However, rapid solidification methods provide an alternative and very attractive way for fabricating amorphous fibers.

Rapidly Solidified Fibers: Rapid solidification techniques were firstly applied to metallic glasses fabrication[19]. As reported by Rudkowski *et al.*[20], several methods exist for the fabrication of rapidly quenched fine metallic fibers. One is to cast the material into water, after shaping it down to the desired diameter; another approach is to use melt extraction from a pendant drop. Among the wide range of rapid solidification techniques, the melt extraction method is the most promising for amorphous ceramic fiber production.

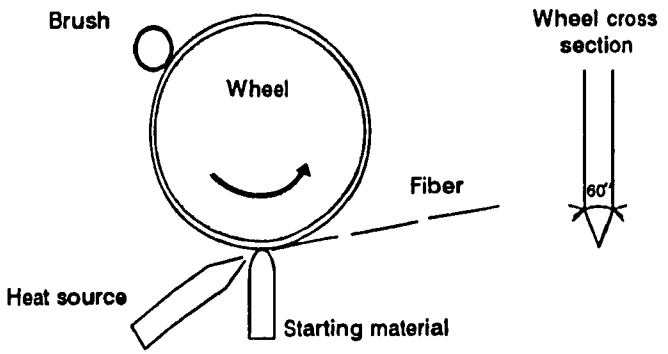

Figure 2.8. Schematic of the melt extraction process.

Figure 2.8 gives a schematic of a device used for manufacturing fibers in a continuous manner. The material to be fiberized is first made into the form of rod. The tip of the rod is melted and is brought into contact with a metal disk which rotates at high speed around its normal axis. During contact the molten material is solidified on the disk edge and extracted from the melt. Centrifugal force causes the material to be thrown away and quenched in air.

Fiber production depends on several processing parameters such as the wheel material (copper, brass, steel, molybdenum), the rotation speed and sharpness of the wheel, and obviously the characteristics of the material being processed.

However, this technique has some limitation; in fact high alumina content ceramic fibers are hard to process in this way because of their high melting point and low viscosity at high temperatures. Binary or ternary oxide ceramic compounds are therefore more likely considered for melt extraction fabrication.

2.1.4 Matrix

The purpose of the composite matrix is to bind the fibers together, to transfer load to and between the fibers, and to protect them from environmental effects and handling. the matrix generally determines the overall service temperature limitations of the composite, and also its environmental resistance.

The high toughness and impact properties of metal alloys are very important in composite materials, since the reinforcement is generally a linear elastic solid and does not have good impact properties by itself. Ductile metal matrices such as aluminum, magnesium, titanium or nickel-chromium alloys undergo energy absorbing plastic deformation under impact and therefore exhibit high toughness, which is very important in many dynamic structural applications[21]. The ductile matrix also permits the blunting of cracks and stress concentrations by plastic deformation and gives the material improved fracture toughness.

2.1.5 Composite

Composite Fabrication: Since composites are generally difficult to machine due to the presence of a ceramic phase, most methods are designed to be produced as net shape components. Several ways of fabrication exist for a metal matrix composite, which can be classified according to the form in which the matrix is introduced (solid, liquid or vapor)[22,23].

The choice of fabrication method depends on the combination of several factors, including:

- the nature of the composite system;
- the shape of the component to be manufactured;
- the field of production (mass production, high technology).

Solid-state diffusion bonding is a solid matrix processing technique which alternates layers of fibers and matrix foils. The assembly is uniaxially hot-pressed and the matrix penetrates between the fibers by solid state deformation.

Spraying or coating methods can be also considered. For example, the plasma spraying technique is carried out by spraying the matrix metals at temperatures above their melting point onto fibers. A thin film of matrix is formed which bonds to the fibers.

Powder metallurgy methods have been successfully employed in the fabrication of discontinuous fiber composites[24]. During this process, fine matrix alloy powder is mixed with reinforcing fibers. The blended mixture is then cold-compacted and sintered or hot-pressed.

Molten matrix methods consist of infiltrating fibers with the melt. The fibers are usually pre-arranged as a preform having the shape and fiber geometry required in the component. A very attractive technique among molten matrix methods for composite fabrication is squeeze-casting.

Squeeze-casting is a liquid-forging process where the liquid metal is solidified under high pressures several orders of magnitude greater than the melt pressure developed in conventional foundry practice. The mechanical properties of squeeze-cast products are controlled by the structure and the morphology derived during solidification. Fine equiaxed grain structure can be obtained as a result of undercooling below the equilibrium solidification temperature and a rapid rate of heat extraction[25]. In the case of the squeeze-infiltration process, composites are fabricated by applying pressure to a fully liquid charge on the surface of a fiber

preform located in a preheated die (Fig.2.9). The main benefit of this process, in addition to the advantages for a classic squeeze-cast product, is that high pressure permits a good infiltration of the fibrous preform by the melt and a very low level of porosity. Moreover the rapid cooling enables a better control of potential interfacial reactions between the fibers and the matrix.

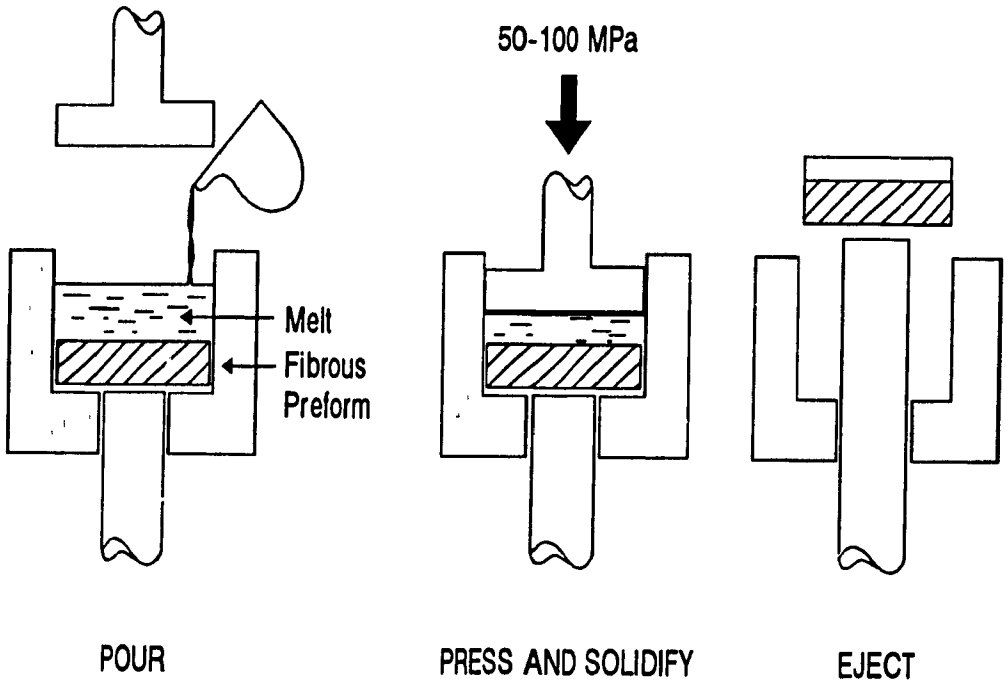

Figure 2.9. Squeeze-casting process for composite fabrication.

2.1.6 Fiber/Matrix Interactions

With metal matrix composites, the elevated temperature of fabrication can lead to chemical and mechanical compatibility problems.

Thermal-Mechanical Compatibility: A corresponding thermal-mechanical compatibility can be solved either by using a ductile matrix that deforms and takes up the differential strain necessary in thermal cycling or by selecting a matrix and

a reinforcement having nearly matching thermal-expansion coefficients. However, since the matrix is usually the more ductile material, it is preferred that the matrix have the higher coefficient of thermal expansion. The reinforcement, a brittle material, is therefore stressed in compression upon cooling.

Chemical Compatibility: Fiber/matrix combinations are seldom in an equilibrium state. Thus in most systems, fiber and matrix will tend to interact usually with detrimental effects on the composite properties. Some of the main interaction phenomena can be fiber dissolution in the matrix, chemical reaction between fiber and matrix or poisoning of fiber by matrix atoms. Several considerations are important with respect to chemical compatibility[24]: the free energy of reacting the two phases, the chemical potential and the surface energy. However, with low temperature metal matrix composites, the chemical-reaction problem can be avoided by keeping the fabrication temperature as low as possible.

2.2 WETTING

The behavior of the fibers with the matrix metal is of primary importance for any fabrication of a metal-matrix composite. The wetting properties of the fibers by the liquid metal can give very important information about potential interfacial reactions. The first requirement for the fabrication of metal-matrix composites, especially by processes involving liquid metals, is a certain degree of wetting of the fibers by the liquid metal which will permit a good bonding between the two phases and generate a strong enough interface to allow transfer and distribution of load from the matrix to the reinforcement without failure.

2.2.1 Theories of Wetting

The degree of wetting of a solid by a liquid in a solid-liquid-vapor system is characterized by the condition of thermodynamic equilibrium. The main thermodynamic relations of the wetting theory are the equations, first proposed by

Young[26] in 1804, for wetting angle θ and the work of adhesion W_a:

$$\gamma_{sv}=\gamma_{sl}+\gamma_{lv}\cos\theta \qquad (2.6)$$

$$W_a=\gamma_{lv}(1+\cos\theta) \qquad (2.7)$$

where γ_{sv}, γ_{sl}, γ_{lv} are the interfacial surface energies at the interfaces solid-gas, solid-liquid and liquid-gas. These equation were obtained theoretically by different methods such as the mechanical equilibrium of forces at the three-phase boundary[27]. The first exact treatment of the thermodynamics of a solid-liquid-vapor system is due to Gibbs[28] who derived Young's equation for the non gravitational case and outlined its derivation for a system in a gravitational field. Johnson[29] provided a more rigorous treatment of the thermodynamics of a solid-liquid-vapor system still assumed to be at chemical equilibrium, i.e. no mass transport across the interfaces.

However, in wetting studies at elevated temperatures, the phases of a solid-liquid-vapor system are not often at chemical equilibrium. Under chemical non-equilibrium, the effect of chemical reactions on the interfacial tensions must be considered and studies have been done[30,31] to correlate the wetting tendency with the free energy of interfacial reactions.

Wetting under Equilibrium Condition: In equilibrium systems, solid and liquid contacting phases are under conditions of thermodynamic equilibrium. The total differential free energy is given as a function of the chemical potential, the interfacial surface energy and the total free energy of each component in the system[32]. At thermodynamic equilibrium, dG=0, and the following equation can be written:

$$\gamma_{sl}dA_{sl}+\gamma_{sv}dA_{sv}+\gamma_{lv}dA_{lv}=0 \qquad (2.8)$$

where A_{sl}, A_{sv}, A_{lv} are respectively the solid-liquid, solid-vapor and liquid-vapor interfacial areas.

According to Aksay *et al.*[33], when liquid and solid phases are brought into contact, a solid-liquid interface forms if:

$$\delta G=\delta\int_{sl}\gamma_{sl}dA_{sl}+\delta\int_{sv}\gamma_{sv}dA_{sv}+\delta\int_{lv}\gamma_{lv}dA_{LV}<0 \qquad (2.9)$$

This free energy decrease results in a driving force for the deformation of the liquid drop. Therefore, for a given system, the free energy changes are only associated with changes in the interfacial areas. A process of adsorption can be observed and equation (2.6) can be applied. The equilibrium angle of contact in this case is accepted to be the wetting angle corresponding to the value determined by this equation.

Figure 2.10 shows the equilibrium of forces on the periphery of a sessile drop. For composite fabrication applications, a contact angle $\theta < 90°$ is sufficient to produce wetting[34]. Wetting is defined as a reduction of the total surface energy of the solid by the liquid ($\gamma_{sv} > \gamma_{sl}$); a condition of $\gamma_{sl} > \gamma_{sv}$ is defined as non wetting. The driving force for wetting can then be given by the difference ($\gamma_{sv} - \gamma_{sl}$).

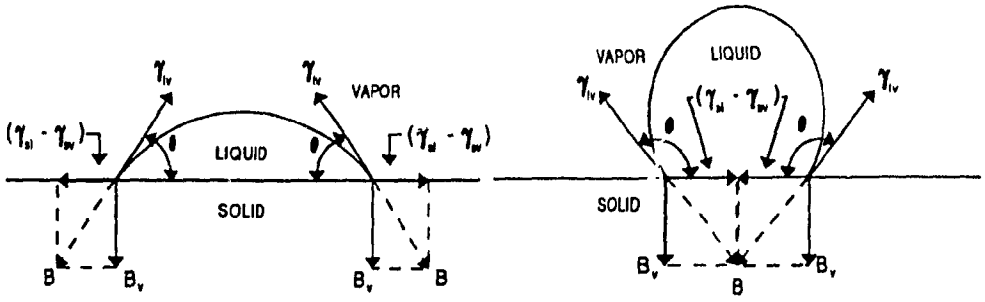

Figure 2.10. Drop configuration for wetting and non wetting conditions

Wetting under Non-Equilibrium Conditions: For non-equilibrium conditions, the system is usually considered to be in thermal and mechanical equilibrium but not in chemical equilibrium. The three phases of the system will react with each other through the interfaces to achieve a state of equilibrium. After the contact surface appears, the system tends to reach an equalization of the component chemical potentials in both liquid and solid phases, by diffusion or dissolution processes or any chemical transformation. For the reaction to proceed, mass transfers across the interfaces must result in a decrease of the free energy of the system. However, in the early contact, the initial decrease of free energy of the system is attributed to a decrease of the interfacial energy γ_{sl}, and the magnitude of the decrease in the interfacial free energy is equal to $(-\Delta G^{sl}/A_{sl})$[35].

According to Pask[36], the action of these processes can result in a decrease of the corresponding interfacial tension. In his work on metal-ceramic systems, Humenik *et al.*[32] interpreted wettability results on the basis of surface tension and free energy changes. Many works have been done on systems under non-equilibrium conditions, and an interfacial energy decrease on wetting solid metals by a liquid phase is often pointed out as a result of a chemical reaction and dissolution. Thus, Kingery[37] found that a metallic liquid will wet a solid metal if a strong chemical reaction takes place. Considering a liquid chemically adsorbed at a solid surface, the work of adhesion released during the adsorption reaction is equal to the energy of the system; in accordance with the Dupré equation[38]:

$$\gamma_{sl}=\gamma_{sv}+\gamma_{lv}-W_a \qquad (2.10)$$

Therefore, an increase of the work of adhesion W_a results in an interfacial energy γ_{sl} decrease.

Allay et *al.*[39] have considered a number of concrete cases of wettability accompanied by chemical interfacial reactions. For a system where the solid phase

is partially soluble in the liquid phase, there should be a minimum in the curve of interfacial energy vs. contact time, considering pure substances initially in contact (see Fig.2.11).

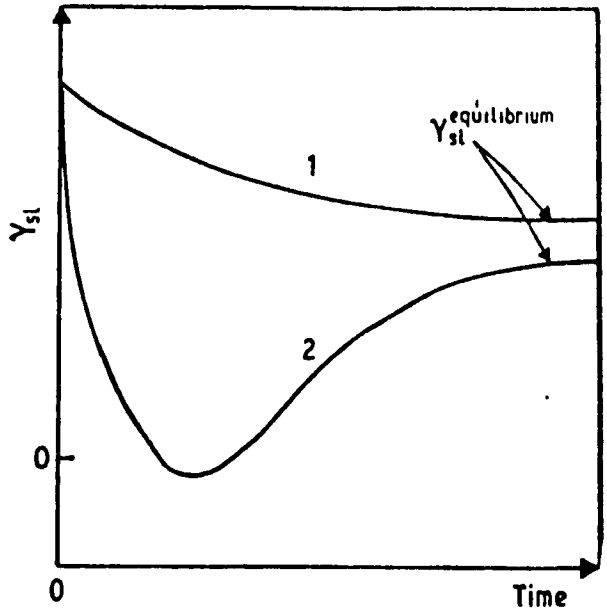

Figure 2.11. Variation of γ_{sl} with time: Curve 1, pure adsorption; curve 2, interfacial reaction.

In his work, Naidich[40] proposes that the dynamic variation of the interfacial tension is proportional to the difference of the component chemical potentials in the contacting phases. The work of adhesion between two phases can be presented as:

$$W_a = W_{a(equil)} + W_{a(non\text{-}equil)} \tag{2.11}$$

Interfacial surface energy is expressed as:

$$\gamma_{sl} = \gamma_s + \gamma_l - W_{a(equil)} - W_{a(non\text{-}equil)} = \gamma_{equil} - \Delta\gamma_{non\text{-}equil} \tag{2.12}$$

where $\Delta\gamma_{non\text{-}equil}$ is a function of the difference of component chemical potentials; $\Delta\gamma_{non\text{-}equil} = \phi(\mu_i^s - \mu_i^l)$. As the system approaches equilibrium, the difference of chemical potential decreases while the interfacial tension increases and stabilizes on reaching equilibrium.

2.2.2 Mechanism of Wetting

The mechanism of wetting is still not fully understood although several theories have been suggested. The main mechanisms which have been proposed for wetting of solids by liquid metals are electronic charge transfer, dissolution, adsorption and chemical reaction.

Electronic Interaction: It has been suggested that the interaction force between liquid metal phase and solid compound is determined by the electronic configuration of the two phases. Ramqvist *et al.*[41] showed that the wettability of transition carbides decreases when the ionicity of carbide bonds increases. The electrons in stable configuration have little affinity to interact with external electrons and consequently poor wetting occurs. The dependence of the wetting angle has been described[33] as a function of the valence electron concentration; good wetting for materials with high valence electron concentration might be due to the low stability of these compounds.However, active interfacial reactions may predominate in the wetting process and reaction products at the interfacial region may reduce the interacting force between the solid and the liquid metal[42].

Adsorption: When intimate intermolecular contact is achieved at the interface, the materials will adhere because of the surface forces acting between the atoms in the two phases. The most common forces are Van der Waals forces[43]. The process is described as a transition of some part of the substance toward the surface but not through the interface[29]. The adsorption is usually limited to the first few monolayers of the interface. The role of adsorption on the change of surface energies and chemical reaction can be considered as a secondary process for

wetting. However, adsorption may act as the primary wetting or spreading mechanism.

For the non-reactive, high vapor systems, adsorption of elements on the solid surface can induce good wetting. An adsorption-evaporation process may affect the wettability of ceramics with liquid aluminum alloys. However, Al or Mg vapor will react with oxygen and Al_2O_3 or MgO phase because of the strong affinity of these elements for oxygen. Therefore adsorption is not believed to be an active wetting mechanism for ceramic/aluminum alloy systems[32].

Interfacial Reactions: In general, whenever interfacial reactions occur, the wetting tendency and work of adhesion are increased. As mentioned in a previous section, the driving force for the reaction is a reduction of total free energy of the system. Since the interfacial reactions proceed as a function of time, they are strongly related to wetting kinetics. However, the excessive reactions can cause the degradation of the solid phase or the formation of unwanted phases at the interfacial region.

Chidambaram *et al.*[44] have presented a thermodynamic criterion that has been developed by treating wetting as a surface phenomenon. The free energy change for an interfacial reaction, ΔG_r, can be used to predict wetting tendencies. A simplistic approach to model the system using bulk thermodynamics considers that wetting is possible whenever the ΔG_r for the reaction at the interface is negative. A simple example can be taken when alumina is in contact with a liquid metal. The following reaction can occur at the interface:

$$Al_2O_3+3xM \rightleftharpoons 3M_xO+2Al \qquad (2.13)$$

The Gibbs free-energy change ΔG_r can be calculated as:

$$\Delta G_r = 3\Delta G^\circ_{M_XO} - \Delta G^\circ_{Al_2O_3} + RT.\ln\frac{a^2_{Al}}{a^{3x}_{M}} \qquad (2.14)$$

where a_{Al} and a_M are the activities of the aluminum and the metal, respectively. A negative ΔG_r implies a spontaneous reaction and wetting.

Many investigators[45,32,46] have suggested that interfacial reactions can make a solid-liquid system wettable; the decrease in surface energy is considered as the result or change in the energy per unit area due to reactions.

It is worth noting that if the reaction products form a coherent, stable and relatively thick layer at the solid-liquid interface, the liquid can be isolated from direct contact with the reacting solid[47]. The system has changed and the expression for W_a becomes:

$$W_a = \gamma_{lv}(1+\cos\theta) + \gamma_{ss} - A\Delta G_r \qquad (2.10)$$

where ΔG_r is the Gibbs energy for the reaction, γ_{SS} is the energy of the solid-reaction layer interface, as shown in Fig. 2.12, and A is a constant related to the number of moles of product formed for unit extension of the drop on the solid.

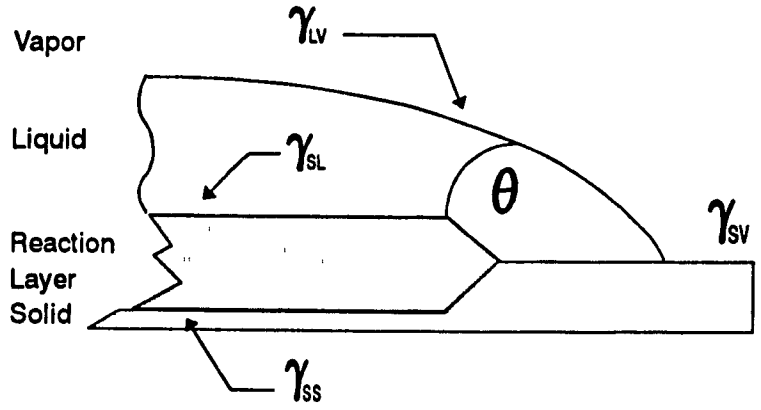

Figure 2.12. Schematic of solid wet by liquid with reaction

2.2.3 Wettability of Ionic Compounds: the Interface Liquid Metal-Oxide

Solid phases can be divided into a number of classes in accordance with their physico-chemical nature. One of these classes is the ionic compound, or predominantly ionic compounds, including mainly high-melting metal oxides and salts.

As a rule, the wettability of high-melting metal oxide by liquid metals is poor. However, observations of metal-oxide contact have shown that some metals, such as titanium, zirconium, tin or aluminum can wet the oxide surfaces[48,49,50]. Brace[51] and Bondi[52] tried to explain the wettability of oxides by some liquid metals by supposing that the liquid metal reduced the solid oxide surface layer to the metal which is wetted by the metal melt. On the basis of the works of Kingery *et al.*[53,54] and Armstrong[55], it can be stated that the wettability of an oxide by a metal and adhesion in such a system increases with growing affinity of the liquid phase for oxygen and that the formation of high charge metal ions, such as Sn^{2+} or Al^{3+} are favorable for metal-ceramic bonding. Generally, it is considered that the weaker the bonds between the metal and the oxygen in the oxide, the greater the chemical interaction and therefore the better the wetting of oxides by metals[29].

According to Weyl's model[56], the larger size and higher polarizability of the oxygen anions, as compared to other ions, cause a reconstruction of the oxide surface with displacement of the cations from the surface to the interior (Fig.2.13)

A double layer is created of which the extreme outer layer contains only anions. It is generally assumed that adhesion with oxides is essentially governed by the interactions of the metal atoms with the oxygen anions only, which can be written as follows:

$$M_2 + M_1O = M_2O + M_1 \qquad (2.16)$$

where M_1 and M_2 are respectively the metal of the solid oxide and the metal of the melt. The chemical contribution to the work of adhesion, W_a, increases with decreasing free energy due to the reaction: $\Delta G_{2,1} = \Delta G^0_2 - \Delta G^0_1$. However, the free energy change associated with the solution of Metal 1 in the melt must be taken into account.

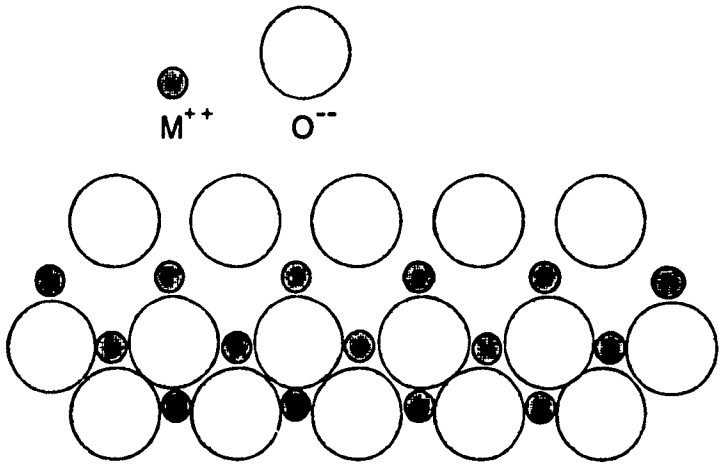

Figure 2.13. The Weyl model of the reconstruction of an ionic compound.

2.2.4 Wetting of Ceramic Phases by Molten Aluminum and Aluminum Alloys

The wettabilities of ceramic materials with liquid aluminum alloys are poor. They have wetting angles usually higher than 90° even above the matrix melting or casting temperatures. For such systems, the application of pressure, only, cannot overcome poor wettability due to the void formation in the small channels during solidification and debonding during service. Therefore, acceptable wettability is the most important parameter for successful casting of composites.

On the basis of Young's equation, the most direct method to achieve an improvement in the wetting of the reinforcement seems to be to raise γ_{sv}, to lower γ_{sl} and γ_{lv}[57,5]. Several factors can influence the wetting behavior of ceramic-liquid metal systems. Some of these factors are outlined in the following section.

Influence of Oxygen Partial Pressure: The wettability of ceramics by molten aluminum has been investigated by many authors in the temperature range 660 to 1350°C[36,58,59,60], mainly with Al_2O_3 materials. The results obtained show significant differences, especially at temperatures below 1000°C, which are probably due to differences in the experimental conditions (Fig.2.14). Brennan and Pask[53] suspected that the sudden decrease of the contact angle at a specific temperature is connected with the presence of an oxide layer on the metal surface. The influence of this layer has been studied by Coudurier *et al.*[61]. The work of adhesion W_a equals about 100 $mJ.m^{-2}$ at the melting point of aluminum; it increases drastically with temperature and reaches its "normal" value (≈1000 $mJ.m^{-2}$) only above 950°C, which is the threshold temperature for the break-up of the aluminum oxide barrier.

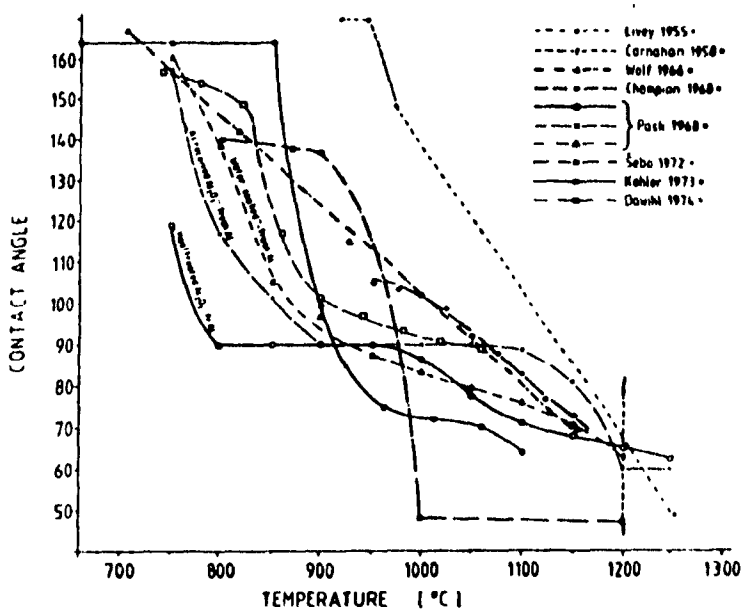

Figure 2.14. Contact angle in the system Al_2O_3/Al (experiments under vacuum).

Hausner *et al.*[62,63] investigated the influence of different oxygen partial pressures obtained with several oxygen getters on the wetting angle of a drop of aluminum on a Al_2O_3 substrate at 700°C. The results demonstrated that an oxygen partial pressure P_{O2} of 10^{-13} bars is the limit for the formation of a droplet by the liquid aluminum. Below 10^{-13} bars, the wetting angle seemed to be proportional to log P_{O2}.

Influence of Surface Roughness: Wetting can be profoundly influenced by the roughness and the texture of the solid surface. Rhee[64] illustrated the influence of the surface r ughness on the contact angle by using ceramic substrates as-hot-pressed (rough surface) and polished to a mirror finish (smooth surface). Based on the work of Dettre and Johnson[65], he reported that the contact angle decreased from non-wetting to wetting as the surface becomes smoother. However, Oliver *et al.*[66] stated that the influence of the surface roughness on wetting behavior is related to the type of roughness. Capillary channelling phenomena along grooves can be observed and are highly dependent on the orientation and texture of roughness.

Temperature Dependence of the Contact Angle: The wetting angles decrease with increasing temperature. This effect may be partly thermodynamic, due to changes in surface energies, and partly kinetic due to rapid desorption and diffusion phenomena. Zisman[67] found that the cosine of the contact angle increases linearly with decreasing surface energy of the liquid. The relation can be expressed by the equation:

$$\cos\theta = a - b\gamma_{lv} = 1 + b(\gamma_c - \gamma_{lv}) \qquad (2.17)$$

where γ_c is the value of γ_{lv} at which the contact angle θ approaches zero.

Based on Zisman's work, Rhee[68] suggested that γ_{lv} can be varied by changing the temperature of the system, and proposed a linear relation between cos θ and the temperature T:

$$\cos\theta = A + BT = 1 + B(T - T_c) \qquad (2.18)$$

where A is a constant, B the slope of the curve and T_c the temperature at which θ approaches zero. This relation is found to be a general rule applicable to many liquid metal/ceramic systems.

Influence of Additive Elements in the Metal: The most widely used technique to promote wettability is to add a wetting agent, usually in the form of an alloying element in the melt. Effective additions fall in two categories. The first are

additions which promote reactions at the solid-liquid interface, such as titanium, zirconium or silicon in aluminum[69,70]. Second, additions to aluminum that do not promote reactions with the solid phase, but modify the characteristics of the oxide layer on the metal surface and reduce the surface tension of the liquid. The most efficient alloying element reported to promote wettability is lithium[71,72]. The primary role of the lithium may be the weakening of the diffusion barrier created by the Al_2O_3 film covering liquid aluminum; lithium is a very strong oxide former and may tend to form spinel by reacting with the oxide layer, and thereby affect its characteristics. Apart from lithium, another addition which has often been reported is magnesium[73,74,75]. The role of magnesium may be justified in a similar way as the role of lithium. In all cases, the rule is to decrease the solid-liquid interfacial energy.

The surface free energy of mixtures of metals is related to the interaction of the components in the bulk and in the surface layer. The component with lower surface tension is enriched at the surface in accordance with the Gibbs adsorption isotherm[76]:

$$\Gamma_i = -\frac{1}{R.T} \cdot \frac{\partial \gamma}{\partial \ln C_i} \qquad (2.19)$$

where Γ_i is the surface excess of the component i which has lower surface tension, and C_i is its reactivity in the solution of surface tension. Therefore, adsorption of an alloying element having a lower γ_{lv} than the liquid matrix at the surface of the solid phase will cause a decrease in the solid-liquid interfacial energy.

Magnesium for example is known to wet Al_2O_3 or silica [77] because of its lower surface tension (559 mJm^{-2}) than pure aluminum (760 mJm^{-2}) at the usual melt temperature (993 K). On the other hand, alloy additions of magnesium decrease the surface tension of aluminum to 620 mN^{-1} for Al-Mg3% at 993 K[78] (see Fig.2.15). Silicon alloying will decrease the surface tension of pure aluminum in the same order of magnitude, either combined with magnesium or not[79].

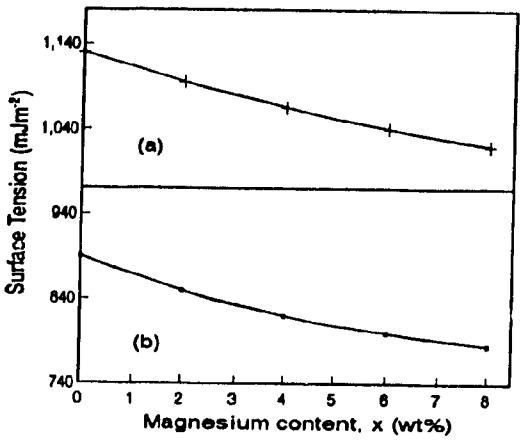

Figure 2.15. Surface tension of Al-Mg alloys as a function of the Mg content. Data for (a) unoxidized and (b) oxidized alloys (T=973 K).

Al/Al_2O_3 fiber-reinforced composites exhibited a concentration of magnesium (present as alloying element in aluminum) at the fiber matrix interface[80], analyzed as spinel $MgAl_2O_4$ on the fiber surface[81]. However, reaction between fiber and matrix is clearly undesirable. A more convenient technique based on the same method would be to modify the ceramic surface itself.

2.2.5 Wetting Angle Measurements

A number of techniques have been introduced to measure contact angles. The sessile drop method and the plate weight method are often used in wetting studies. Another method based on capillary pressure has been more recently reported by Cornie et al.[82].

Sessile Drop Method: The main characteristics of the contact capillary system (solid-liquid-gas) are the angle of contact of the solid wetted by the liquid and the surface tension of the liquid. As reported by Kingery[40], the contact angle can be calculated either by using relations developed by Bashforth and Adams[83], or several methods based on the same fundamental relationships[84,85].

The contact angle can also be calculated from the drop dimension (height h and diameter of wetting perimeter 2a) by the following relation[29] for spherical segment (valid for small drops):

$$\tan \theta = \frac{2ha}{a^2 - h^2} \tag{2.20}$$

Apart from these methods, the contact angle can be directly measured by drawing the tangent to the drop contour near the wetting perimeter.

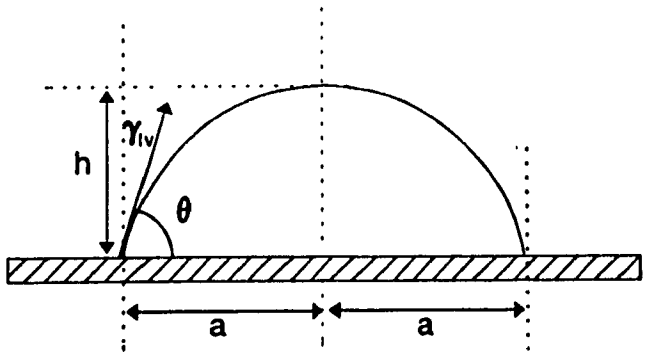

Figure 2.16. Sessile drop method for contact angle measurements.

Plate Weight Method: The plate, partially submerged in the liquid, is subject to a capillary force tangential to the plate surface and normal to the wetting perimeter[86]. The free energy of this system, expressed as a function of γ_{lv}, H, and x (see Fig.2.17), can be derived to lead to the expression of the capillary force projected in the x direction:

$$f_x = -2b\gamma_{lv}\cos\theta$$

where b is the width of the plate.

The contact angle being measured is determined by the expression:

$$\cos \theta = \frac{\Sigma\ \Delta l_i \cos\ \theta_i}{l} \tag{2.22}$$

where $l = \Sigma\ \Delta l_i$ is the wetting perimeter length and θ_i is the contact angle corresponding to the length l_i.

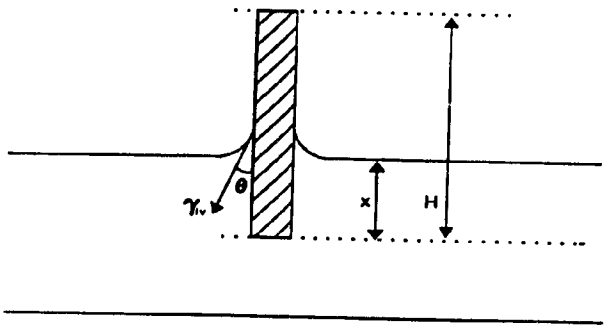

Figure 2.17. The derivation of the force equation for the plate immersed into a liquid.

Capillary Pressure Method: Capillary rise is related to surface energy balances and wetting phenomena. The height to which a liquid rises or is depressed depends on the capillarity diameter, and the wetting angle. Considering the equilibrium of the raised liquid, capillary pressure P_c is given by:

$$P_c = \frac{2\gamma_{lv}\cos\theta}{r} \qquad (2.23)$$

where r is the capillary radius (see Fig.2.18). When the liquid is forced through the capillary system by an applied pressure, a threshold pressure occurs before infiltration begins. This threshold can be related to equation (2.23) and therefore converted into contact angle θ.

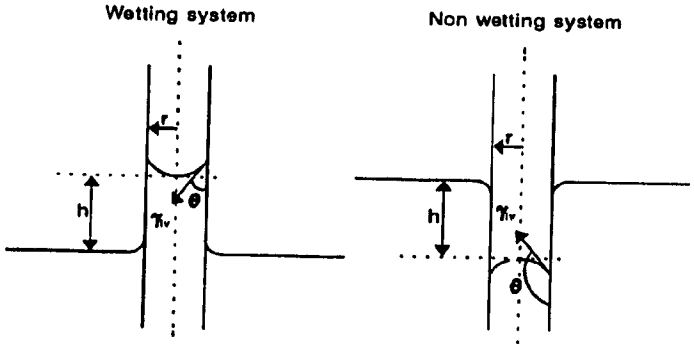

Figure 2.18. Schematic diagram of a liquid on a capillary surface.

2.3 ZIRCONIA/ALUMINA/TITANIA AND ZIRCONIA/ALUMINA/SILICA SYSTEMS

Ceramic materials are generally more stable than other materials at elevated temperatures and corrosive environments and present in addition good mechanical properties. Among ceramics, the oxides are perhaps the most common and abundant, because they are more easily fabricated and more stable in air than non-oxide ceramics such as nitrides, and carbides. Oxide ceramics can be classified according to their different representative crystal structure, depending on the configuration of the oxygen ions and the stoichiometry of the elements.

There are many combinations of single oxides which can lead to multicomponent or multiphase oxides. The multicomponent oxides refer to the oxides which contain more than one cation type in the structure. The additional cations allow a range of structural types to be synthesized, allowing the selective optimization of the material properties. In the same way, a multiphase oxide approach will be usually attempted to improve a particular set of properties[87]. Thus, in terms of fiber fabrication, eutectic combinations of oxide ceramics are very attractive for specific forming processes such as melt extraction techniques compared to single component oxides. Binary or ternary eutectic systems lead to lower melting temperatures and changes in the melt viscosities which can make the system viable for melt extraction.

2.3.1 An A_2O_3 Type Oxide

A_2O_3 type oxides with a corundum structure present usually excellent properties in hardness, corrosion resistance, high thermal conductivity and heat resistance. Alumina (Al_2O_3) is a representative oxide of this class. A number of transitional Al_2O_3 structures can form with increasing temperature, but all structures are transformed irreversibly to α-Al_2O_3 with a corundum structure of hexagonal system. This form is generally used for structural and electrical applications.

Because of a strong chemical bond strength between the Al and O ion, Al_2O_3 exhibits outstanding physical stability, such as a high melting point (2050°C), one of the highest hardness among oxides, and high mechanical strength (modulus of elasticity E = 300 to 390 GPa, tensile strength up to 450 MPa at 25°C[88]). Fracture toughness at room temperature ranges from 3.85 to 5.9 MPa$\sqrt{m}$[77] depending on the density. However, thermal shock resistance is poorer than ceramics such as Si_3N_4 or SiC because the coefficient of thermal expansion is large.

2.3.2 AO_2 Type Oxides

TiO_2: TiO_2 exists as three polymorphs; low-temperature stable anatase, brookite and high temperature stable rutile. The rutile structure easily forms non-stoichiometric oxides and shear structure oxides derived from the large number of oxygen vacancies. TiO_2 has a melting point of 1855°C; a modulus of elasticity E = 282 GPa and the modulus of rupture (MOR) ranges from 69 to 100 MPa[89].

SiO_2: This ceramic is a representative oxide which has distinctive engineering properties such as a low thermal expansion, a low thermal conductivity, and glass-forming ability derived from the covalent nature of the Si-O bond. The liquid which is formed when crystalline SiO_2 is melted has an unusually high viscosity. Therefore, the liquid has a strong tendency to form a glass, rather than crystallize upon cooling. Generally, the strengths of SiO_2 are not large, except for the single crystal. Depending on the structure, the MOR varies from 70 to 250 MPa with a modulus of elasticity around 75 GPa for bulk fused silica[90].

ZrO_2: Zirconia exhibits three polymorphs: the monoclinic, tetragonal and cubic phases. The monoclinic phase is stable up to about 1170°C where it transforms to the tetragonal phase. ZrO_2 transforms from tetragonal to cubic phase at 2370°C, which is stable until the melting point of 2680°C[91]. The tetragonal to monoclinic transformation upon cooling is associated with a large volume change (3 to 5%). This is sufficient to exceed the fracture strength of ZrO_2 and the strain can only be

accommodated by cracking. Additives such as calcia, magnesia or yttria can be used to stabilize or partially stabilize the material in either the tetragonal or cubic phase.

The addition of Y_2O_3 to ZrO_2 as well as stabilizing the tetragonal and cubic forms, lowers the temperature of the tetragonal to monoclinic transformation. Several groups have been working on the potential of zirconia for increasing both the strength and toughness of ceramics by utilizing the tetragonal to monoclinic transformation of metastable tetragonal particles induced by the presence of the stress field ahead of a crack[92-94].

2.3.3 Multiphase Oxides: Zirconia/Alumina

One of the more common systems under investigation has been the Al_2O_3/ZrO_2 ceramic, when pure zirconia or partially stabilized zirconia is added to Al_2O_3 powder, mixed and sintered or hot pressed. This two phase material results in a significant increase in strength and toughness.

In general, the equation for the rate of sintering can be written as a function of temperature, grain-size, and density[95]:

$$\frac{d\rho}{dt} = A.\frac{e^{-Q/RT}}{T}.\frac{f(\rho)}{d^n}$$

where

$$A = \frac{C\gamma V^{2/3}}{R} \qquad (2.25)$$

Here, $d\rho/dt$ is the rate of densification, d is the grain size, γ is the surface energy, V is the molar volume, $f(\rho)$ is a function only of density. R, T and Q have their usual meaning. C is a constant and A is a material parameter which is insensitive to d, T or ρ. The grain size power law, n, depends on whether the densification rate is controlled by lattice diffusion (n = 3) or by grain-boundary diffusion (n = 4).

Wang and Raj[96] performed sintering experiments at constant heating rates, and estimated the activation energy for sintering of alumina containing 5 vol% zirconia. Addition of zirconia required a higher temperature for sintering than nominally pure alumina. A very high activation energy for boundary diffusion was found in the alumina/zirconia system (730 ± 50 kJ/mol for alumina/zirconia, compared to alumina 480 ± 42 kJ/mol[84]). It can be attributed either to the enthalpy for defect formation or to the presence of a liquid phase at grain interfaces[97].

Ultrarapidly quenched Al_2O_3/ZrO_2 mixed powders were sintered by Pilate and Cambier[98]. The ultrarapidly quenched powder contained a metastable phase (γAl_2O_3), high temperature stable phase (tetragonal ZrO_2) and a high content of amorphous phase (30-50wt%). A 90/10wt% composition was sintered at 1600°C for one hour to achieve 96% of the theoretical density. Most of the zirconia particles were found to be intergranularly located.

More recently, Ando and Shiohara[99] melt-extracted hypoeutectic Al_2O_3-25wt% ZrO_2 and eutectic Al_2O_3-42 wt% ZrO_2 (see Fig.2.19) ceramics into rapidly solidified thin (20 to 150 μm) flakes. The main constituents in the melt-extracted microstructure of the eutectic ceramic were fine eutectic and amorphous structures.

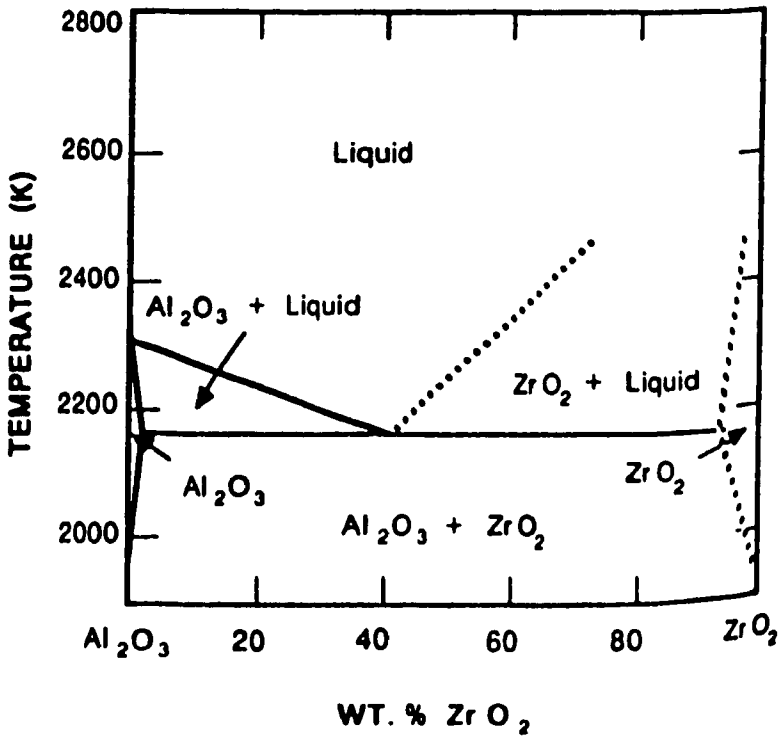

Figure 2.19. Al_2O_3/ZrO_2 phase diagram.

Properties of the Al_2O_3/ZrO_2 system are dependent upon a number of parameters, including the Al_2O_3:ZrO_2 ratio, the stabilizers in the zirconia, the grain

size and distribution of each phase, as well as the processing conditions. Commercially available grades of Al_2O_3/ZrO_2 show an extremely high flexural strength (2400 MPa at room temperature) and still relatively high elastic modulus (260 GPa)[100].

2.3.4 Zirconia/Alumina/Titania System

The ternary system $ZrO_2/Al_2O_3/TiO_2$, referred to as ZAT, shows some relatively deep eutectic regions. Three eutectic compounds can be found with a melting point ranging from 1580°C to 1610°C. According to the phase diagram (Fig.2.20), two binary compounds are present in the system: zirconium titanate ($ZrTiO_4$), and aluminum titanate (Al_2TiO_5).

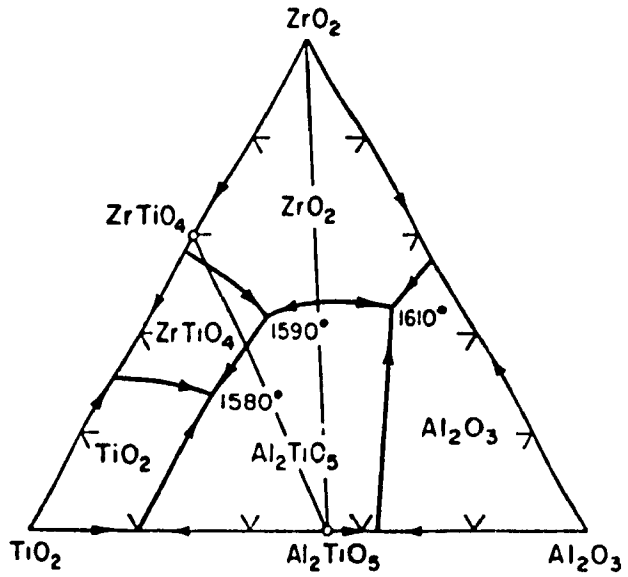

Figure 2.20. $ZrO_2/Al_2O_3/TiO_2$ phase diagram (wt%).

Because of a good thermal shock resistance and a low thermal conductivity, aluminum titanate is a very attractive material for thermal insulation or refractory applications. However, thermal expansion microcracking causes a very low mechanical strength and the compound tends to decompose to alumina and titania between 750°C and 1300°C[101].

ZAT system has been reported as a new family of low thermal expansion ceramics[102]. Thomas *et al.*[103] examined the effect of adding zirconia, stabilized with 3 mol% yttria, on the properties of aluminum titanate. The ceramic, sintered at 1500°C, reached 94% of the theoretical density and was found to contain aluminum titanate and zirconia as

a mixture of the tetragonal and monoclinic phases. The result of the incorporation of zirconia was a development of an inhomogeneous microstructure of elongated Al_2TiO_5 grains of various sizes and the zirconia appeared to be distributed along grain boundaries. The sintered density was improved and the mechanical strength of the sintered product was increased over that of Al_2TiO_5. The reliability of the fracture strength increased with zirconia addition as well.

Zirconia is believed to refine the grain structure of aluminum titanate[104]. However, according to Shindo *et al.*[105] zirconia is an effective grain refining agent for alumina matrix in alumina-zirconia ceramics, but has less effect on titania-containing ceramics. Osendi *et al.*[106] studied the influence of TiO_2 on the mechanical properties at high temperature of a zirconia-toughened alumina. Titania was shown to be a very efficient sintering aid for alumina/zirconia ceramics, and average densities of 4.1 (96% to 98% of D_{th}) were achieved after firing at 1570°C for 1 hour[107]; the material exhibited elastic moduli up to 340 GPa at room temperature. On the other hand, formation of glassy pockets located at triple points, and Ti segregation on alumina grain boundaries was observed. The Ti seemed to act in this case as a barrier for ZrO_2 grain growth, but also had significant adverse effects on high-temperature mechanical properties.

2.3.5 Zirconia/Alumina/Silica System

The ternary system $ZrO_2/Al_2O_3/SiO_2$, referred as ZAS, shows one eutectic (ZrO_2 = 31wt%, Al_2O_3 = 53wt%, SiO_2 = 16wt%) with a melting point around 1780°C. In accordance with the phase diagram (see Fig.2.22), the ZAS system presents two binary compounds; mullite and zircon ($ZrSiO_4$).

Mullite is the only chemically stable intermediate phase at atmospheric pressure in the SiO_2-Al_2O_3 system. The chemical composition of mullite is usually denoted as $3Al_2O_3.2SiO_2$ (60 mol% Al_2O_3)[108]. Due to the important physical and chemical properties of mullite such as low thermal expansion, and very high chemical stability[109], improvement of the mechanical performance of mullite-based materials appears very attractive. It is known that the addition of a dispersed

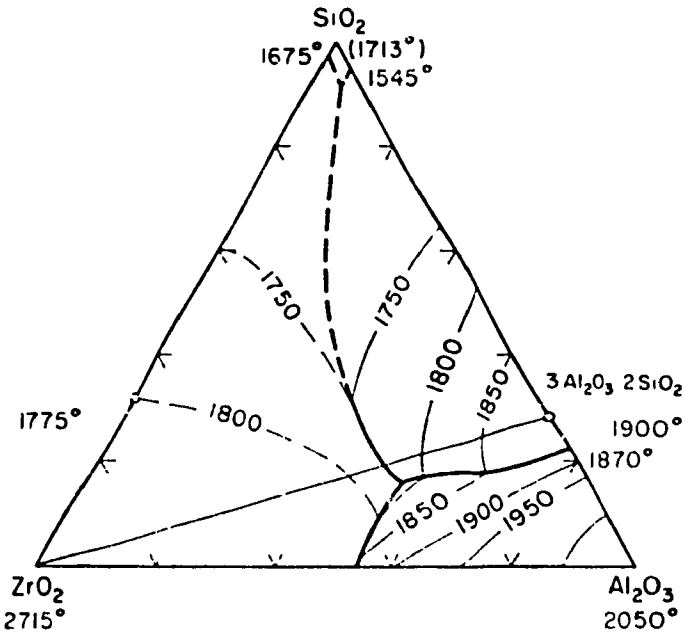

Figure 2.22. The ZrO_2/Al2O3/SiO2 phase diagram.

tetragonal phase of ZrO_2 in a ceramic matrix enhances its resistance to crack propagation[110,111]112. Moya and Osendi[112] studied the sintering, microstructure and toughness of mullite/ZrO_2 ceramics with increasing amounts of ZrO_2 (up to 20%). Samples were sintered at 1575°C to achieve 99% of the theoretical density, with ZrO_2 grains mainly located at the Al_2O_3 grain boundaries. Grain boundary strengthening has been proposed as the main toughening mechanism of the ZrO_2/mullite system[42], produced by a metastable solid solution between mullite and ZrO_2 grains. Moreover, the ZrO_2 addition was found to promote densification and retard grain growth of the mullite phase in the mullite-ZrO_2 ceramic system[113].

Zircon ($ZrSiO_4$) can be used as a raw material for ZAS ceramic preparation. The reaction sintering or hot-pressing will therefore follow the reaction[114]:

$$2ZrSiO_4 + 3Al_2O_3 \rightarrow 3Al_2O_3.2SiO_2 + 2ZrO_2 \qquad (2.26)$$

Reaction sintering in the $ZrO_2.SiO_2/Al_2O_3$ system proceeds by atomic solution, diffusion, reprecipitation both in pressureless sintering and hot-pressing[115]. During pressureless sintering, the boundary phase is the non-crystalline mullite phase formed by sudsolidus reactions. Claussen and Jahn[116] fabricated fully-dense zirconia-mullite ceramics (d= 3.76) by sintering an alumina-zircon mixture to high density (1450°C) and then reacting in situ (1600°C). During the reaction sintering of such a system, Di Rupo and Anseau[117] observed the occurrence of a transitional non-crystalline mullite phase at 1400°C and 1425°C located at the boundary between

$ZrO_2.SiO_2$ and Al_2O_3 grains.

Rapid quenching of melts in the ZAS system has been studied by Yoshimura *et al.*[118] who produced amorphous flakes of various composition using an arc-furnace and twin-roll process. In the ZAS system, amorphous materials tended to form in the highest Al_2O_3 compositions.

Recently, Nogami *et al.*[119] prepared toughened glass ceramics in the ZAS system by the sol-gel process, with a composition range 0-30mol%Al_2O_3, 30-60mol% ZrO_2, 40-70mol% SiO_2. The fracture toughness was found to be dependent on both Al_2O_3 and ZrO_2 content; the highest value achieved was 9 MPa$\sqrt{m}$. Previously, Low and McPherson[120] had studied the crystallization behavior of a gel-derived ZAS system.

Chapter 3:
OBJECTIVES

The conventional experimental approach to wettability consists of measuring the contact angle of a drop of the liquid metal resting on a flat substrate of the ceramic reinforcement material.

This work will be aimed at fulfilling the following objectives:

1. To define and apply the optimum processing parameters to the fabrication of binary and ternary oxide ceramic substrates (ZA, ZAT, ZAS).

2. To characterize the ceramic microstructure and properties.

3. To study the effect of the following parameters on the wetting behavior of the ceramic substrates by liquid aluminum alloys:

   a- Temperature

   b- The nature of the ceramic

   c- Alloying elements (Si and Mg) in the aluminum

4. To determine the best metal-ceramic system with a view to fabricating melt extracted fiber reinforced composites.

Chapter 4: EXPERIMENTAL PROCEDURES

4.1 CERAMIC SUBSTRATES

4.1.1 Starting Material

Material Specification: Alumina (Al_2O_3), partially stabilized zirconia (ZrO_2), silica (SiO_2) and titania (TiO_2) powders were used to prepare Zirconia/Alumina/Titania (ZAT), Zirconia/Alumina/Silica (ZAS) and Zirconia/Alumina (ZA) ceramic substrates. In addition, alumina was used directly as a substrate. The specifications of the four oxide ceramic powders and the sintered Al_2O_3 substrate are shown in Table 4.1 and Table 4.2 respectively.

Table 4.1. Oxide ceramic powder specifications.

Oxide	Purity (%)*	Particle size (μm)	Supplier
Al_2O_3-A16SG	99.85	0.35	Alcoa (USA)
ZrO_2-TZ-3Y	94.7 (5.2 Y_2O_3)	0.2	TOSOH corporation, Tokyo (Japan)
SiO_2	99.5	0.88	Johnson Matthey (USA)
TiO_2-T-315	99.6	0.45	Fisher Scientific (USA)

(*) Supplier's data

Table 4.2. Specification of Al_2O_3 substrate[a]

Density (g/cm^3)	3.8
Purity (%)	99.5
Grain size (μm)	17
Open porosity (%)	0-4
Elastic modulus (GPa)	372

Powder Particle Size Analysis: The particle size of the starting powders was measured by using the dynamic laser light scattering NICOMP 370[b]. This instrument is suitable for measuring particle diameter in the nanometer range.

A small amount of powder (~1g) was dispersed in 50 ml of distilled water and the agglomerates were broken down with an ultrasonic probe; four drops of sodium polymethacrylate[c] were added as a dispersant. About 5 ml of liquid suspension was injected into the instrument.

Each particle is illuminated by the incident beam of a laser focused on the glass tube containing the dilute dispersion. By measuring the intensity of the scattered light, the mean spherical diameter of each particle can be calculated and displayed. The mean diameter of each raw powder is reported in table 4.3.

Starting Material: X-ray diffraction analyses performed on zirconia, alumina, titania, and silica powders show the initial form and composition of each starting material. Powder identification was carried out with an X-ray diffractometer[d] using filtered CuKα radiation. The accelerating voltage was 40 kV (± 0.1%) and the

---

[a]Coors Porcelain Co.

[b]Pacific Scientific Instrument Division.

[c]Darvan C, R.T. Vanderbilt Company.

[d]Philips X-ray diffractometer APD1700

beam current was 20 mA (± 0.1%), with a scan speed of 0.01 deg.sec^{-1}. A 20° to 80° range was selected for the angle 2θ. Zirconia powder (Fig.4.1a) was a mixture of the monoclinic form (stable up to 1170°C) referred as baddeleyite and the tetragonal form of ZrO_2 (stable from 1170°C to 2370°C). As shown on Fig.4.1b, alumina powder was used in the form of α-Al_2O_3 with a corundum structure of a hexagonal system. Starting TiO_2 powder was the high-temperature stable rutile form. Neither anatase nor brookite polymorphic structures, which transform irreversibly to rutile at temperature from 400°C to 1000°C, were detected (Fig.4.1c). Finally, Fig.4.1d indicates that SiO_2 powder was used in the low quartz form (trigonal crystal system), stable up to 575°C, which is the most common crystalline form of silica.

4.1.2 Powder Processing

Ceramic Composition: Eutectic or peritectic compositions were selected for the ceramic substrate fabrication because of their relatively low melting point. The compositions of the three eutectic compounds are reported in Table 4.3.

Table 4.3. Composition and melting point of ZAT, ZAS and ZA eutectics.

System	Zirconia wt% (mol%)	Alumina wt% (mol%)	Titania wt% (mol%)	Silica wt% (mol%)
ZAT	44 (37.8)	42 (43.6)	14 (18.6)	--
ZAS	31 (24.4)	53 (50)	--	16 (25.6)
ZA	42.6 (38)	54.7 (62)	--	--

1610	1780	1890	Melting point (°C)
ZAT	ZAS	ZA	

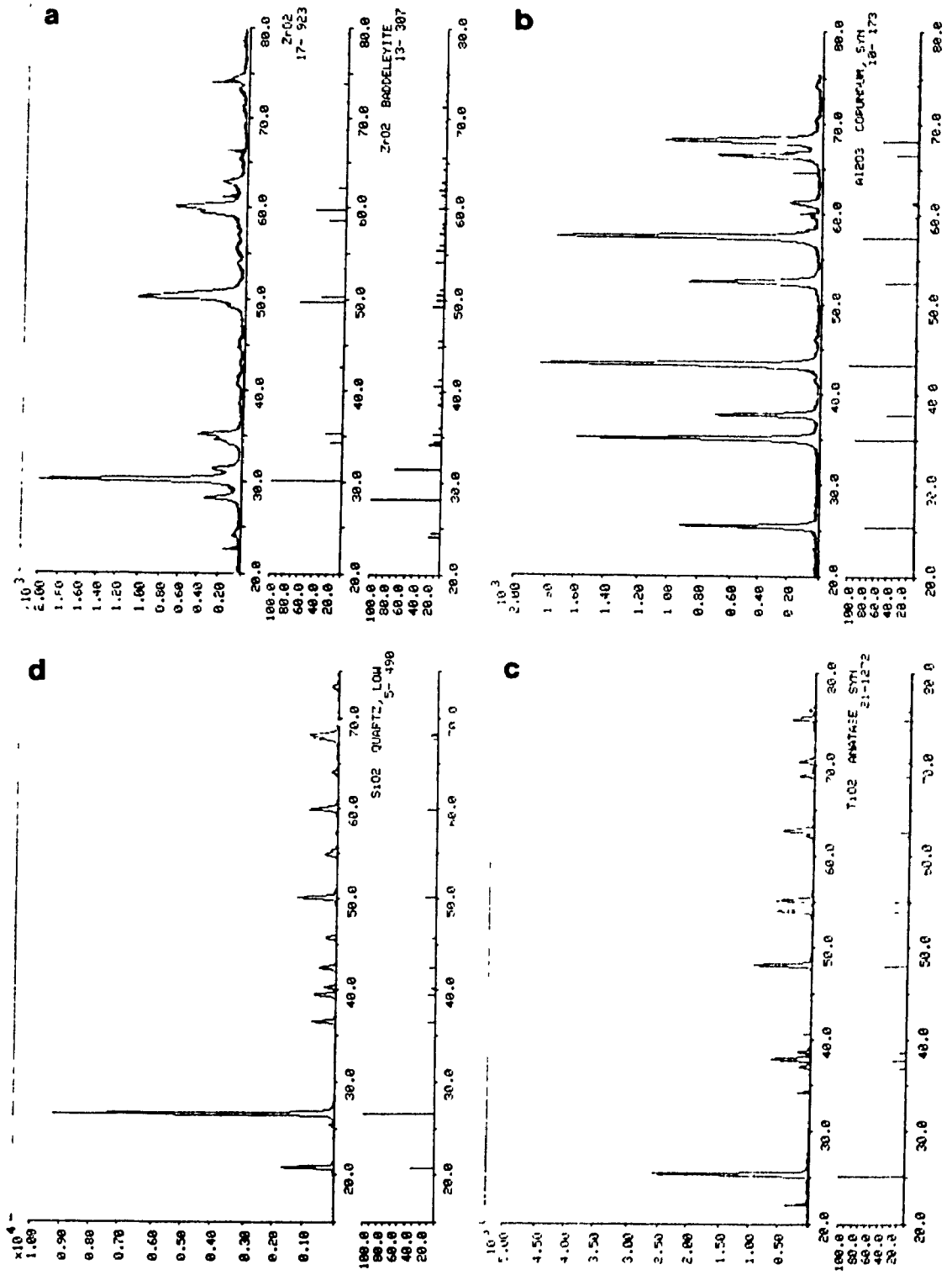

Figure 4.1. XRD patterns of: (a) ZrO_2, (b) Al_2O_3, (c) TiO_2, (d) SiO_2.

Green Compact Fabrication: Each powder combination was mixed in the wet state using isopropyl alcohol. The mixtures of ZAT, ZAS and ZA were attrition milled at a speed of 150 rpm for 45 minutes in a 4L Teflon container. The ratio of solid to liquid was 1 to 5 by weight. Al_2O_3 (99.7% pure) milling media[a], having a diameter of 3.7 mm, was used in the proportion of 2.5 times the weight of powder used. After attrition milling, the slip was separated from the media by passing it through a 212 μm sieve. It was then dried in a microwave oven, and stored in a dryer at 150°C for 24 hours to remove any trace of isopropyl alcohol. The resulting large aggregates of dry powder were granulated through a 125 μm sieve to form a free flowing powder.

Green compacts were formed by uniaxially pressing the powder as a pellet (ϕ= 2.5 cm, h= 2.5 mm) using a die press at a pressure of ~ 35 MPa. The uniaxial compaction was performed in two steps in order to avoid a gradient of pressure in the pellet. Fig.4.2 shows the processing route for green compact fabrication.

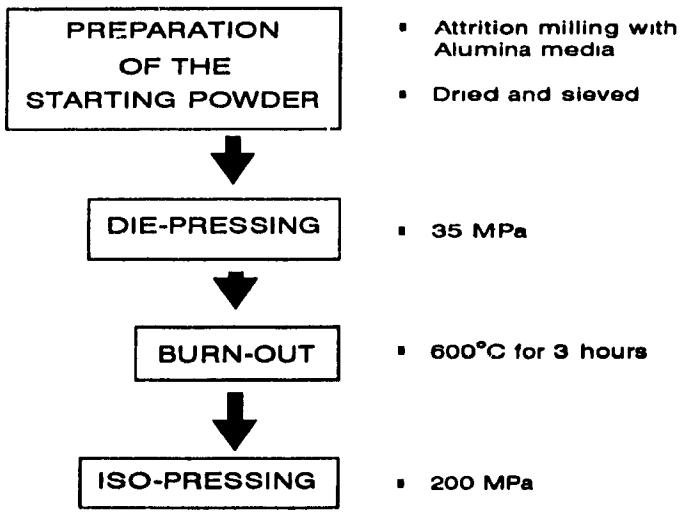

Figure 4.2. Processing route for green compact fabrication.

[a]Union Process

4.1.3 Sintering

The green compacts were prefired in air at 600°C for 3 hours in order to burn out any impurity present in the bulk pellet or organic contaminants which might have been introduced during sieving or die pressing. They were then isostatically pressed at 200 MPa just before sintering. The densities of the green samples were calculated by dry weight and dimension.

The green samples were densified by sintering in a water cooled graphite element furnace, shown schematically in Fig.4.3. All experiments were carried out under vacuum (~40 Pa). The samples were placed in a BN crucible, embedded in a loose BN/Al_2O_3 powder mixture. The sintering temperature ranged from 1400°C to 1790°C depending on the nature of the processed ceramic, and was maintained for 2.5 hours. The heating cycle was controlled using an Omega CN-2010 controller[a] and was programmed to heat at a rate of 60°C/min (Fig.4.4). The temperature was measured with a C-type (W-5%Re/W-26%Re) thermocouple[b]. The furnace was calibrated by determing the temperature at which pure metals (Cu, Ni, Fe, Cr) melted. The controller temperature was then compared to the actual melting temperatures of each metal, to establish the off-set temperature at ±10°C.

4.1.4 Ceramic Characterization

Density Measurements: The extent of densification of ZAT, ZAS, and ZA ceramics after sintering was measured by calculating the density of the samples using Archimedes' principle as laid out in ASTM C373-88. The open porosity was measured by calculating the surface water absorption as described in the above procedure.

---

[a]Omega Engineering Inc.

[b]Omega Engineering Inc.

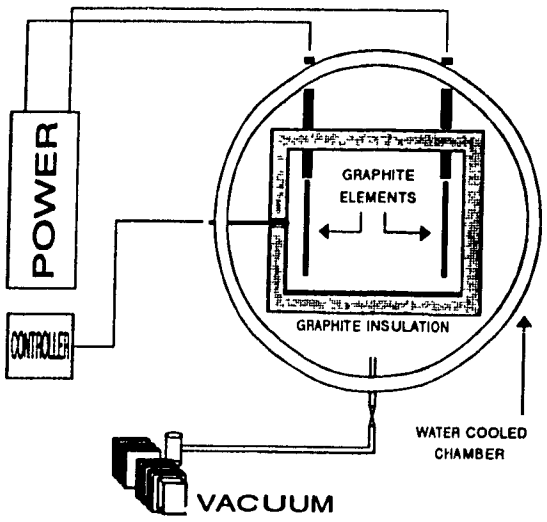

Figure 4.3. Graphiteelement furnace for sintering experiments.

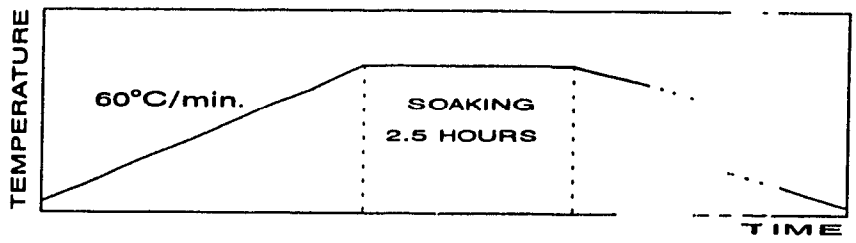

Figure 4.4. Sintering temperature time-schedule.

In order to estimate the remaining closed porosity of each material, the sample bulk densities were compared to the theoretical densities of the sintered and ground powder, measured by using a null-pycnometer[a]. The sintered sample is ground into a fine powder and inserted in the sample cell. The density measurement is based on the difference of pressure encountered between filling the empty cell and the loaded sample cell with a same quantity of inert gas. The calculation is derived from the first law of thermodynamics.

---

[a]Quantachrome Corporation

X-ray Diffraction Analysis: Phase identification was carried out by X-ray powder diffraction. The fired samples were ground into powder and were analyzed with an X-ray diffractometer using filtered CuKα radiation. The experimental parameters are given in section 4.1.2. A 20° to 80° range was selected for the angle 2θ. The different phases were determined, according to the phase diagrams, by matching the resulting diffraction patterns with reference patterns[a].

4.2 WETTING

The sessile drop method was designed to measure the contact angle between the different ceramic substrates and aluminum alloys. An outline of the method has been previously given in section 2.2.5. Details of the experimental procedure are developed in the following sections.

4.2.1 Furnace Equipment

The experimental apparatus used to measure the contact angle by the sessile drop method is described in Fig.4.5. It consists essentially of a closed end quartz tube heated externally by a resistance furnace. A temperature controller Omega CN9000 A, with a type K thermocouple and accuracy of ± 5°C was used to control the temperature in the furnace. A quartz window was fitted at one end of the tube in order to take pictures of sessile drops at the experimental temperatures.

The chamber was connected to a vacuum device consisting of a rotary vacuum pump and an oil diffusion pump which was capable of achieving a vacuum of $\sim 10^{-6}$ Torr. In addition, the presence of titanium sponges placed in the tube permitted very low oxygen partial pressures around the sessile drop. In order to prevent oxygen contamination, a gas line under vacuum was used to back-fill the furnace with ultra high purity argon. The drop and the substrate were supported by an alumina D-shape.

---

[a]Powder Diffraction File, JCPDS International Center for Diffraction Data.

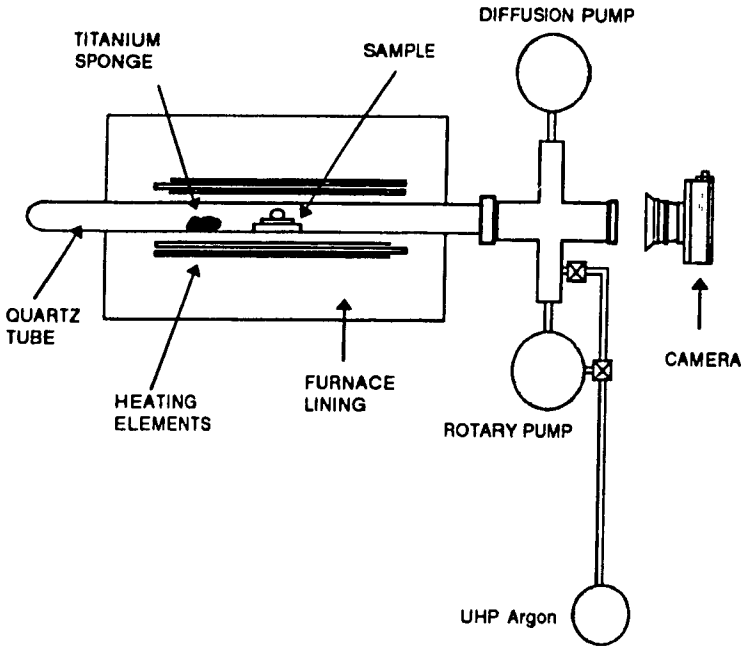

Figure 4.5. High vacuum tube furnace for wetting experiments.

4.2.2 Substrate Preparation

Surface Preparation: After sintering, the substrates were mounted with epoxy on a steel plate, then were ground and levelled off using an automatic surface grinder. The epoxy was then burnt out and each substrate was polished separately with 15 μm, 6 μm, and then 1μm diamond paste, finishing with a 0.03 μm alumina suspension. After polishing, the average height and width of surface asperities of the platelets was estimated to 0.05 μm.

Heat Treatment: Before the experiments, the substrates were ultrasound cleaned in acetone and then annealed under vacuum at 1000°C for 1 hour, using the furnace described in the previous section, in order to eliminate any hydroxyl groups or organics that might have been adsorbed on the surface, and to prevent the substrate surface from undergoing any structural change which might have occurred during the experiments.

4.2.3 Alloy Preparation

Fabrication: In addition to pure aluminum, four different alloys were used. Chemical analysis and compositions of the starting materials are reported in Tables 4.4 and 4.5, respectively.

Table 4.4. Chemical analysis of the starting materials.

Main impurities	Si (wt%)	Mg (wt%)	Zn (wt%)	Fe (wt%)	Ti (wt%)	Ca (wt%)
Al	0.005	-	-	0.003	-	-
Mg	-	-	-	0.05	0.03	0.01
Si	-	0.6	0.03	-	0.01	-

Table 4.5. Composition of the experimental aluminum alloys.

	Al[a] (wt%)	Si[b] (wt%)	Mg[c] (wt%)
Al-Si10	90	10	-
Al-Si5	95	5	-
Al-Mg2.4	97.6	-	2.4
Al-Mg1.1	98.8	-	1.2
Al-Mg-Si[d]	92.2	7	0.8

[a] Aluminum (99.98% pure) from ALCOA.

[b] Silicon (99.3% pure) from SKW.

[c] Magnesium (99.5% pure) from TIMMINCO METALS.

[d] Alloy (A357 series) provided by BELMONT METALS.

Aluminum-magnesium alloys were prepared in fire-clay crucible using a copper coil induction furnace[a]. Aluminum wrapped Mg pieces were introduced into molten aluminum and maintained below the melt with a graphite rod until complete melting and dissolution of the magnesium. After homogenization, the alloy was cast into a 50g ingot.

Aluminum-silicon alloys were prepared by arc-melting under argon gas. Aluminum chips mixed with silicon pieces were melted on a cold copper anode. The alloy was melted several times to insure a good homogeneity, and solidified into 20g bar shaped ingots.

Characterization: The alloying element content in the raw aluminum alloys was analyzed by emission spectrometry using a Baird-Atomic spectrometer[b]. The G06H4 and G25H1 standards were used to calibrate the emission curves for Mg and Si elements. The average contents of the alloying elements were taken after five burns.

In addition, atomic absorption spectrometry[c] was performed on Al-Mg alloys after heating up to experimental temperatures. The alloy drops (~1g) were dissolved in 20ml of concentrated hydrofluoric acid at 50°C. The Mg content in the solution was then determined by flame atomization, using air-acetylene gas and a Ne type hollow cathode as the light source.

Surface Preparation: The surface roughness has a significant influence on oxidation of aluminum and aluminum alloys, and polished aluminum surfaces gain much less weight than unpolished ones[121]. The alloy piece was therefore polished with 1000 grit metallographic paper both for removing the oxide layer and

---

[a]Tocco Process Equipment, 10 KHz.

[b]BAIRD-ATOMIC, Spectrovac 1000 DV-2.

[c]Instrumentation Laboratory Inc. aa/ae Spectrophotometer 357.

preventing it from a further surface oxidation. It was then ultrasound cleaned in isopropyl alcohol for 10 minutes prior to experimentation.

4.2.4 Wetting Experiments

After sample preparation (see previous sections), the alloy piece (~1g) was placed on the substrate and the assembly was slid into the furnace tube. The chamber was evacuated for 40 minutes, after several back-fillings with inert gas, to reach a vacuum of 10^{-6} torr. The sample was then heated at a rate of 110°C/min up to the required experimental temperature. After 45 minutes, the sessile drop was furnace cooled.

Furnace Atmosphere: Experiments involving pure aluminum and aluminum-silicon alloys were conducted under vacuum. In the case of aluminum-magnesium and aluminum-magnesium-silicon alloys, experiments were performed under an ultra high purity argon[a](99.999% pure) atmosphere. The furnace was first evacuated to 10^{-6} torr. At 600°C, inert gas was introduced in the tube up to atmospheric pressure, through a gas line previously purged and evacuated to 10 millitorrs.

Data Collecting: Photographs of the sessile drop were taken during the experiments using a NIKON F401 mounted with a 110mm lens. Both heating and soaking periods were observed. No external light source was required for temperatures above 700°C. The contact angle was calculated by the tangent method (see section 2.2.5). The measurement of the contact angle was made to ±1°, the reproducibility generally being within ±5°.

---

[a]Matheson Gas Products.
The sum of N_2, O_2, CO, CO_2 and H_2O are < 10 ppm.

4.2.5 Microscopy and Microstructural Analysis

Microscopy: Observations of interfaces and microstructures were carried out using different techniques including reflected optical microscopy[a] and scanning electron microscopy[b]. Polished samples were prepared by mounting in epoxy resin and sectioning with a diamond cut off wheel, followed by conventional grinding and diamond polishing. The samples were Au-Pd sputter coated prior to SEM examination. A 10 kV acceleration voltage was used to minimize charging of the sample and edge effects.

Energy Dispersive Spectroscopy and X-Ray Mapping: Qualitative interface analyses were carried out by electron dispersive spectroscopy (EDS) using acceleration voltages in the 10 to 15 kV range. The detector was able to operate with either a Be window (7.5 μm thick) or an ultra-thin Al window (0.1 μm). The Be window was used to detect elements with a large range of atomic numbers (Al, Si, Zr, Ti) and was connected to a Tracor Northern[c] analysis system.

Because of the size of the different phases in the microstructure, no quantitative EDS or microprobe analyses could be carried out on the ceramic specimens. Therefore, qualitative phase analysis was performed by x-ray mapping[d] using the detector described previously. X-ray images, set-up by a Tracor Northern TN 8500 system, were obtained with an exposure of 4000 counts/cm^2 under an acceleration voltage of 15 kV.

---

[a]Neophot, LECO.

[b]JEOL 840 A

[c]Tracor Northern TN-96-606E3/513.

[d]Tracor Northern TN-96-60E3/513.

Microprobe Analysis: In addition, quantitative interface analyses were performed on polished and carbon coated samples by electron probe spectroscopy[a] using a high purity germanium detector[b]. Standards for calibration were SiO_2, Al_2O_3, MgO, and pure Zr for the detection of Si, Al, Mg, and Zr, respectively. Analyses were conducted using an acceleration voltage of 15 kV, with a spot size of 2 μm and a counting rate of 25 counts/sec.

---

[a]CAMEBAX

[b]EXPLORER, NORAN Instruments.

Chapter 5:
RESULTS & DISCUSSION

PART 1: CERAMIC SUBSTRATES

The aim of this part of the thesis was the fabrication of ceramic substrates for further wetting experiments. Therefore, no complete characterization was performed on the ceramic materials, but only microstructural studies necessary for a good understanding of the ceramic/liquid metal wetting behavior.

5.1.1 SINTERING TEMPERATURE

5.1.1.1 Effect of Sintering Temperature on Bulk Density and Open Porosity

Conventional procedures were used to fabricate the green pellets; the processing parameters were therefore not investigated.

A study of the influence of the sintering temperature on the bulk density and the apparent porosity was carried out for Zirconia/Alumina, Zirconia/Alumina/Titania, and Zirconia/Alumina/Silica ceramic substrates. Both the bulk density and the open porosity were measured by the Archimedes' principle.

Zirconia/Alumina (ZA): The melting point of the ZA eutectic is 1890°C. Therefore, densification experiments were performed at temperatures ranging from 1500°C to 1790°C, for an holding time of 2.5 hours.

Fig.5.1 shows the evolution of the bulk density with the sintering temperature. The average density value of five fired samples is plotted every 50 °C. The curve shows that the density increases from 3.2 to 4.6 $g.cm^{-3}$ when the temperature increases from 1500°C to 1790°C; the densification process occurs mainly between 1550°C and 1790°C since the green pellets before firing present a density d_g= 3.1 $g.cm^{-3}$. The theoretical density, also reported on the Figure, was measured from the powder of a fully densified sample.

In addition, the open porosity versus the sintering temperature is plotted on Fig.5.2. The open porosity plays an important role in the wetting behavior; too much

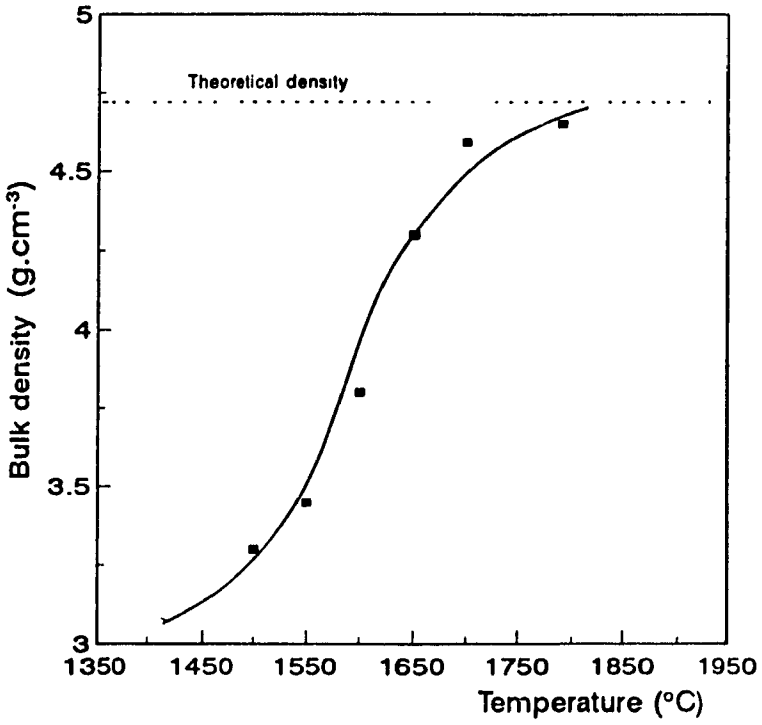

Figure 5.1. ZA: evolution of bulk density with temperature

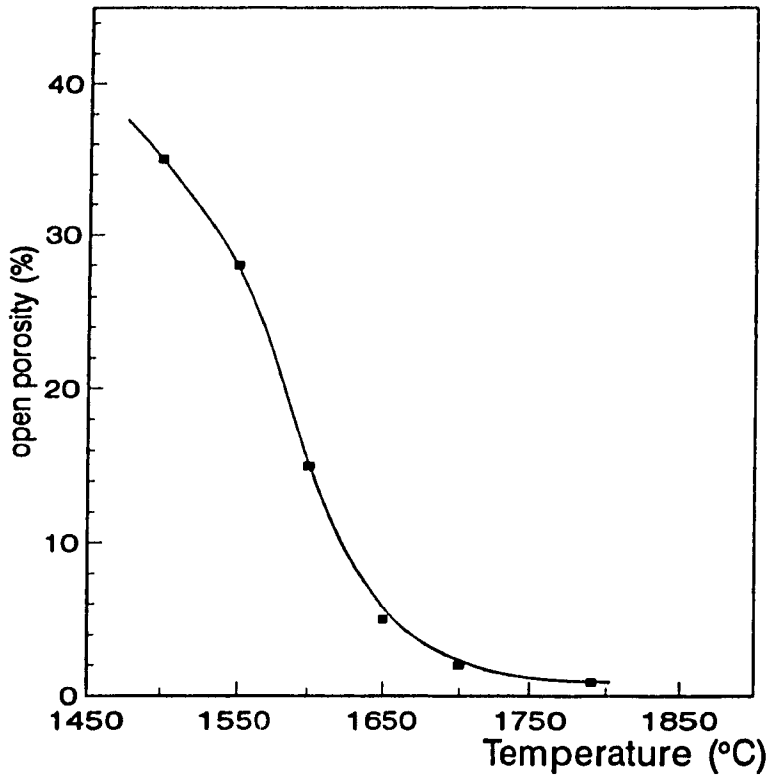

Figure 5.2. ZA: evolution of open porosity with temperature

open porosity can affect the contact angle of the liquid metal on the ceramic substrate. The curve shows, in this case, a final open porosity less than 0.9% for a sintering temperature of 1790°C.

Zirconia/Alumina/Titania (ZAT) and Zirconia/Alumina/Silica (ZAS): Fig.5.3 and 5.4 demonstrate the effect of firing temperature on the bulk density for the eutectics of ZAT and ZAS respectively. The average bulk densities are plotted every 50°C from 1300°C to 1500°C for ZAT and from 1400°C to 1680°C for ZAS; the soaking time for each temperature was 2.5 hours.

No significant changes in the bulk density of ZAT pellets were observed below 1400°C. Samples achieved a density of 4.5 $g.cm^{-3}$ after sintering at 1500°C for 2.30 hours. The remaining open porosity was 1.1% as seen in Fig.5.5.

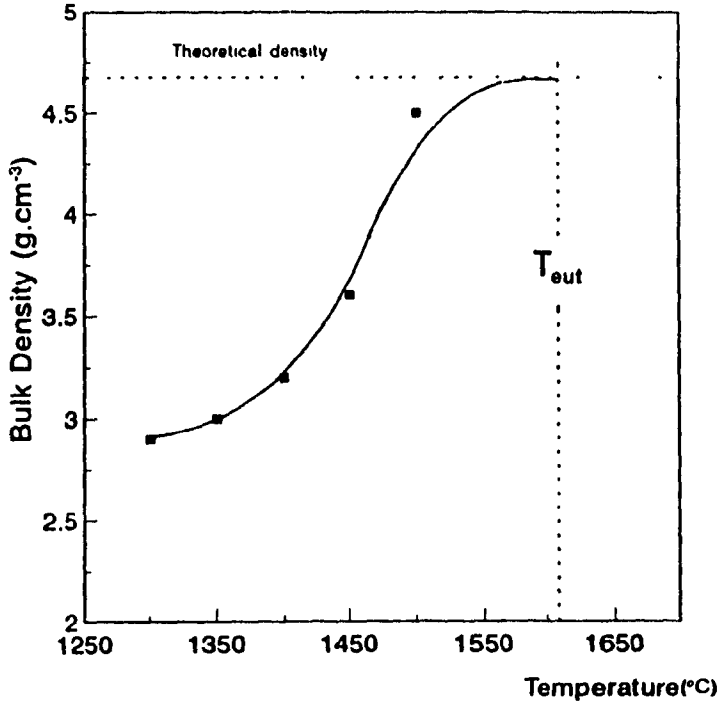

Figure 5.3. ZAT: effect of firing temperature on bulk density

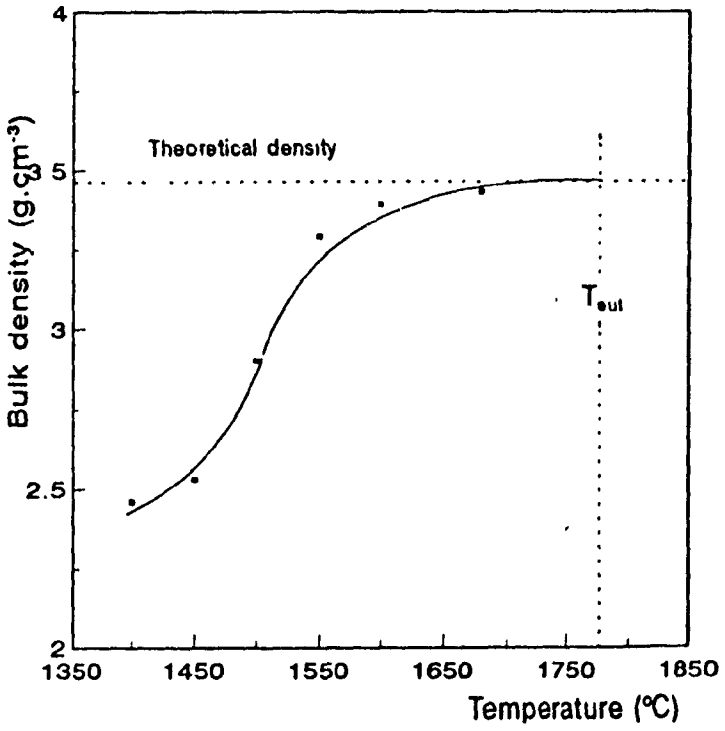

Figure 5.4. ZAS: effect of firing temperature on bulk density

The bulk density of ZAS samples increases from 2.45 to 3.45 $g.cm^{-3}$ when the sintering temperature increases from 1400°C to 1680°C. However, the densification process begins probably below 1400°C since the green density is 2.2 $g.cm^{-3}$. Fig.5.6 shows that the open porosity is still 5% even at high temperature (1600°). Nevertheless, the remainder of the open porosity is reduced to 1.2% after 2.30 hours at 1680°C.

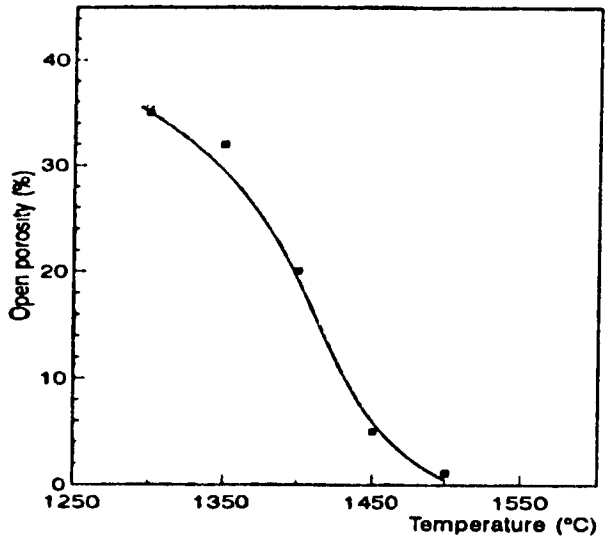

Figure 5.5. ZAT: evolution of open porosity with sintering temperature

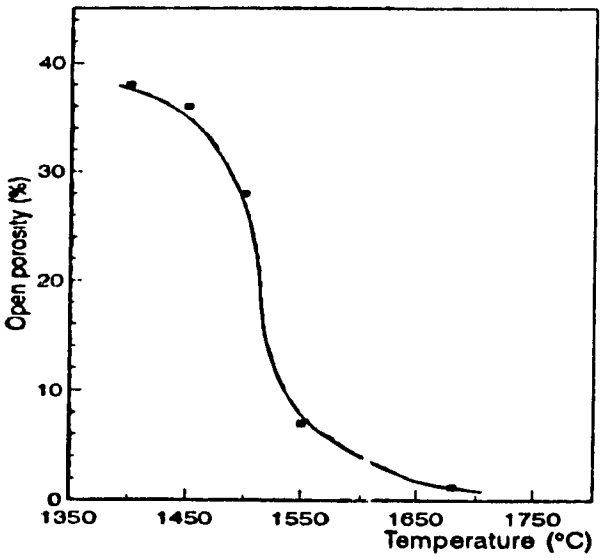

Figure 5.6. ZAS: evolution of open porosity with sintering temperature

5.1.1.2 Evolution of the Relative Density with Sintering Temperature

Fig.5.7 shows a comparison of the effect of firing temperature on the relative density of each ceramic system studied. All the materials achieved a relative density over 97% with an open porosity less than 1.2% (Table 5.1). From this figure it can be inferred that both TiO_2 or SiO_2 additions accelerate the initial densification rate of Zirconia/Alumina powder.

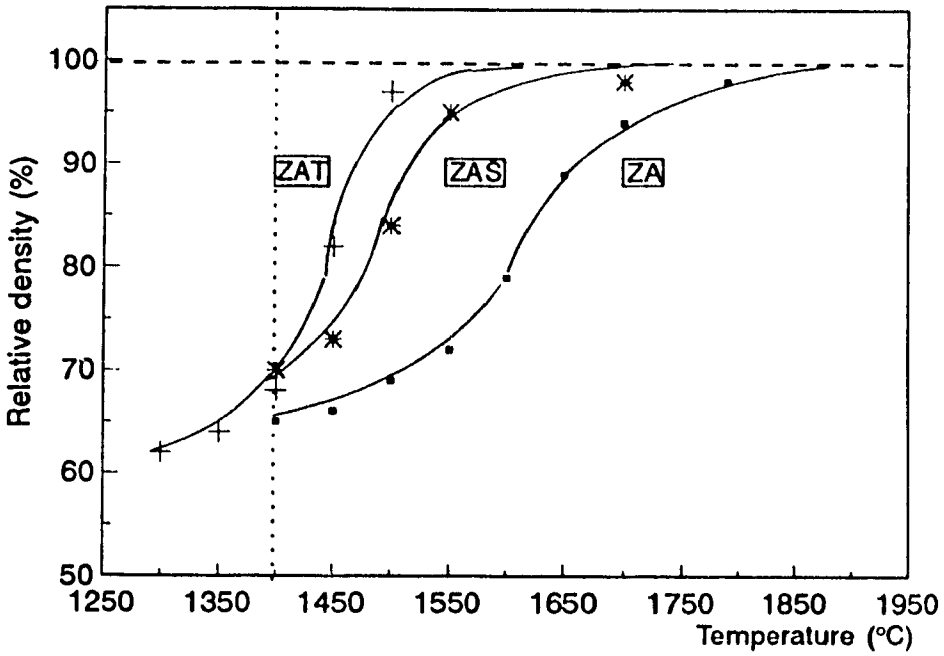

Figure 5.7. ZA, ZAT, and ZAS: evolution of relative density with sintering temperature

Table 5.1. Densities and open porosity for ZA, ZAT, and ZAS

	Green density	Bulk density after sintering (at T°C)	Theoretical density	Apparent porosity (%)
ZA	3.1	4.6 (1790°C)	4.71	0.9
ZAT	2.8	4.5 (1500°C)	4.65	1.1
ZAS	2.2	3.4 (1680°C)	3.48	1.2

Osendi and Moya[107] suggested that TiO_2 acts in the same way as it does on sintering of Al_2O_3; that is a substitution of Al^{3+} by Ti^{4+} generating aluminum vacancies which promote more rapid diffusion rates. However, because of the high amount of TiO_2 added to ZA (18.6 mol%), the change in the densification behavior with temperature is more probably due to the occurrence of a new phase in the system.

In the same way, the addition of SiO_2 to ZA (24.4 mol% ZrO_2 + 50 mol% Al_2O_3 + 25.6 mol% SiO_2) obviously results in the formation of mullite at the eutectic sintering temperature of 1780°C, and therefore modifies the densification rate. The formation of new phases in both ZAT and ZAS systems is discussed later.

5.1.2 BULK CHARACTERIZATION OF THE SINTERED CERAMICS

5.1.2.1 Sintered Zirconia/Alumina/Titania

Fig.5.8 shows the X-ray diffraction pattern of a fully sintered ZAT sample (1500°C for 2.5 hours). The main diffraction peaks of a new phase, $ZrTiO_4$, were detected for angles corresponding to 24.3°, 30.5°, 49.5°, and 60.6°. Most of these peaks, however, were overlapping with those belonging to ZrO_2, which existed as a mixture of the monoclinic and tetragonal phase (as observed for the starting material). Finally, Al_2O_3 had not reacted with the other constituents and was still in the initial corundum form.

5.1.2.2 Sintered Zirconia/Alumina/Silica

Fig.5.9 presents the X-ray diffraction pattern of a fully sintered ZAS sample (1680°C for 2.5 hours). The main difference between the raw material and the sintered one was the occurrence of the mullite phase ($3Al_2O_3.2SiO_2$). The amount of Al_2O_3 had therefore likely decreased during sintering. In addition, the presence of cristobalite was detected in the specimen, although most of the peaks

corresponded to the mullite phase; the cristobalite results from the conversion of the quartz during firing. Finally, ZrO_2 had not reacted with the other constituents, however only the tetragonal form could be detected.

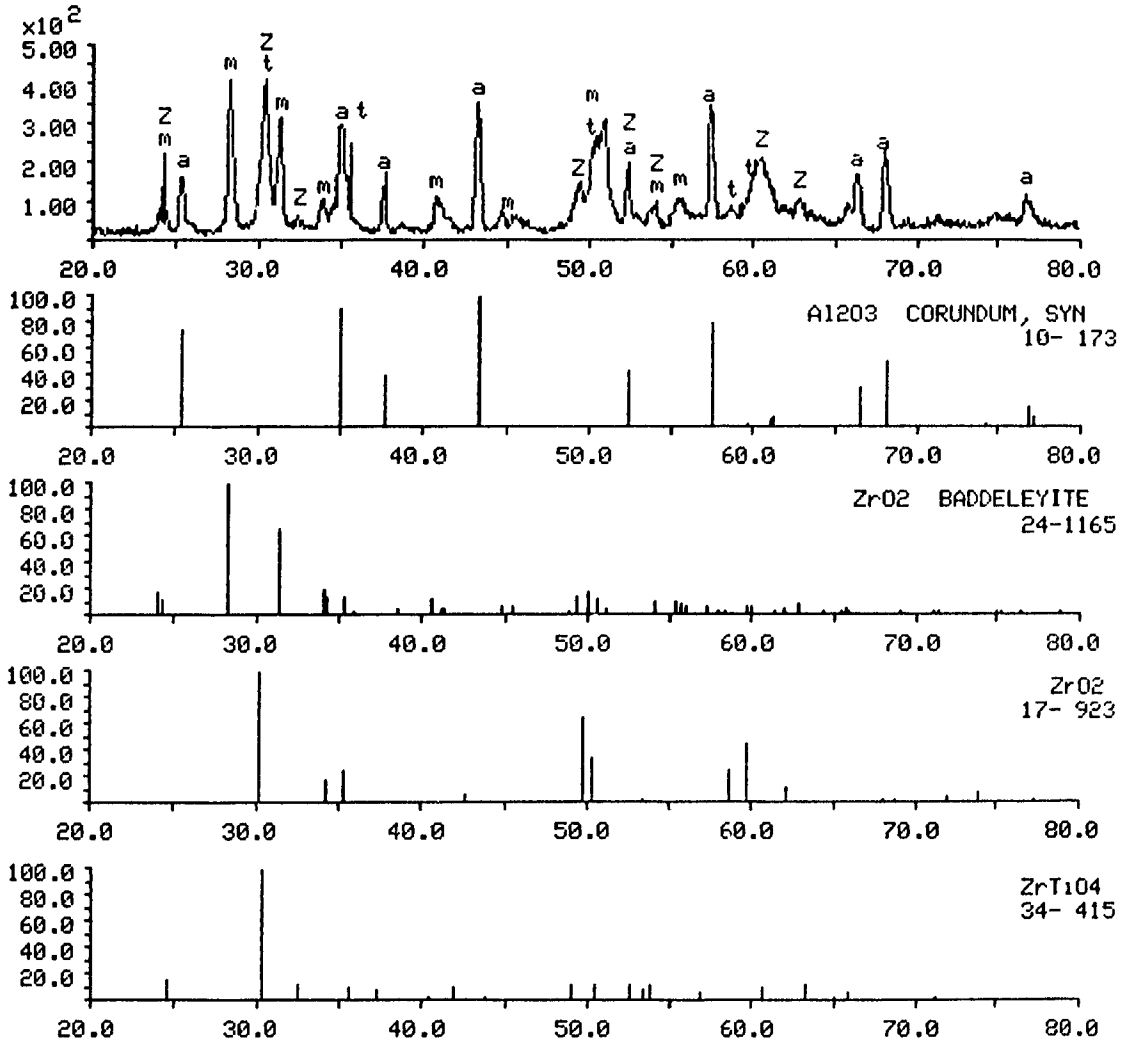

Figure 5.8. X-ray diffraction pattern of sintered ZAT (2.5 hours, 1500°C). a=Al_2O_3; t=tetragonal ZrO_2; m=monoclinic ZrO_2; Z=$ZrTiO_4$; no TiO_2 was detected.

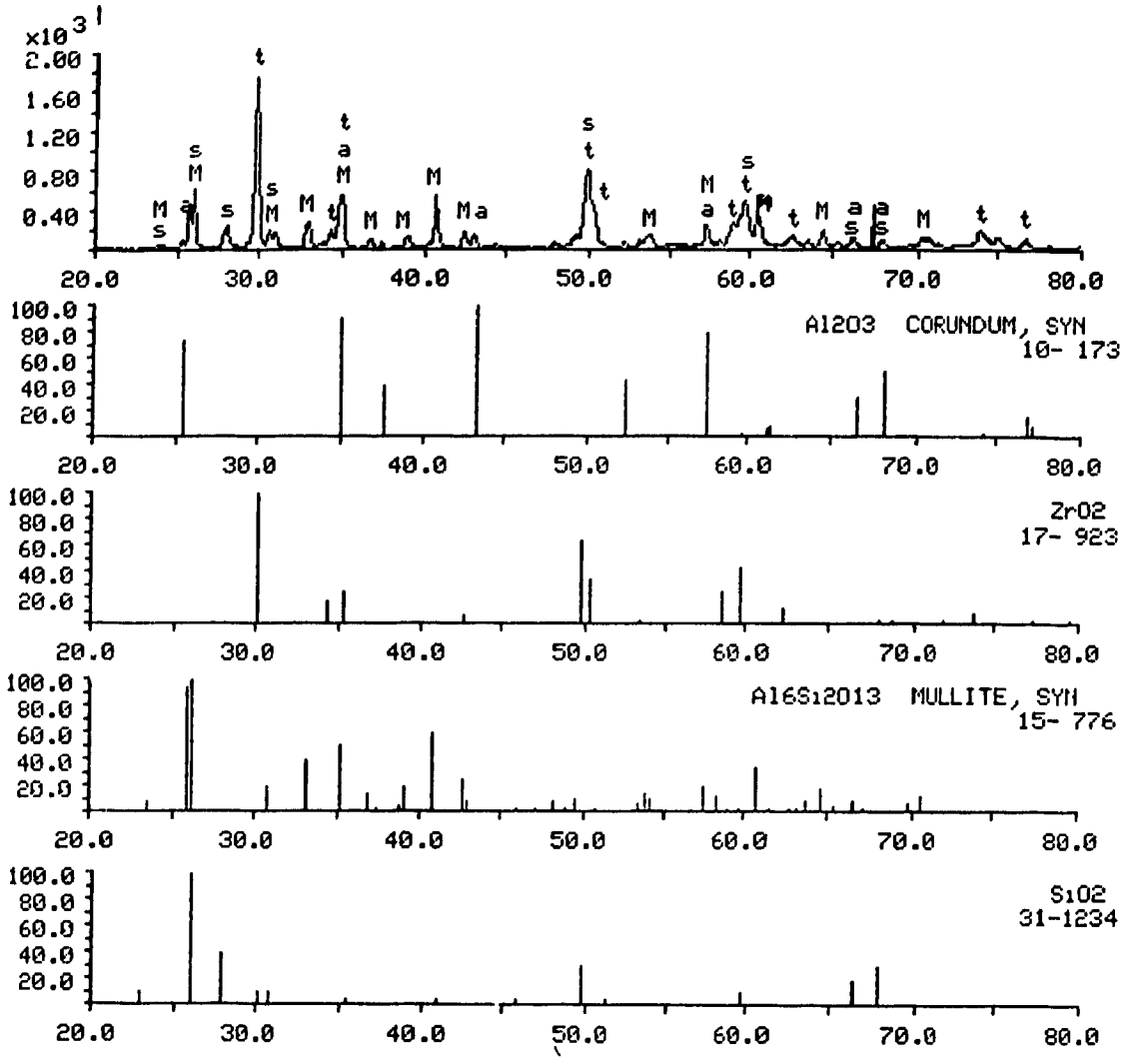

Figure 5.9. X-Ray diffraction pattern of sintered ZAS (2.5 hours, 1680°C). a=Al_2O_3; t=tetragonal ZrO_2; c=cristobalite; M=mullite; s=SiO_2.

X-ray diffraction analyses produced a very good approach for determining the different phases present in both ZAT and ZAS specimens. However, no quantitative or semi-quantitative analyses could be performed on the diffraction patterns because of major peak overlapping. Any attempts to resolve the peaks ended in failure. Calculations based on equations related to the reaction sintering

mechanisms are therefore the best method for estimating the expected relative amounts of each phase present in the ceramic.

Table 5.2 summarizes the phases encountered in fully sintered ZA, ZAT and ZAS ceramics.

Table 5.2. Phases present in ZA, ZAT, and ZAS fully sintered samples

	PHASE			
ZA	Al_2O_3 (corundum)	ZrO_2	--	--
ZAT	Al_2O_3 (corundum)	ZrO_2*	$ZrTiO_4$	--
ZAS	Al_2O_3 (corundum)	ZrO_2	SiO_2 (cristobalite)	$3Al_2O_3.2SiO_2$ (mullite)

(*) Monoclinic and tetragonal

5.1.2.3 Zirconia/Alumina Ceramics

According to the zirconia/alumina phase diagram (Fig.2.19), ZA ceramics present a binary structure; ZrO_2 and Al_2O_3 occur as a duplex phase structure below 1900°C for the eutectic composition (42.6 wt% ZrO_2 + 54.7 wt% Al_2O_3) with very little mutual solid solubility. This simple structure morphology, reported in the literature[122,106,98,99] has been confirmed by X-ray and microstructural analyses, as described in the following sections.

5.1.3 MICROSTRUCTURAL CHARACTERIZATION OF ZA, ZAT, AND ZAS SPECIMENS

SEM observations and X-ray mapping were performed on ZA, ZAT, and ZAS polished sections to complete the results obtained from the bulk characterization.

5.1.3.1 Zirconia/Alumina

An analysis of the microstructure of a polished section of ZA shows a relatively homogeneous mixture of zirconia and alumina (Fig.5.10a). From this picture, it can be seen that materials consist of a dispersion of alumina particles in a zirconia matrix. Most of the alumina particles are intergranulary located but some appear embedded in the zirconia phase.

Most of the zirconia and alumina grains are of the same size and are in the range of 1 to 4 μm. However, some coarser zirconia grains (up to 8μm) can be observed, and are the result of abnormal grain growth during sintering due to agglomeration of ZrO_2 particles during processing; a few small pores can be detected at the ZrO_2/Al_2O_3 grain boundary regions.

The phase observation is confirmed by X-ray mapping. Fig.5.10b shows the X-ray map of the polished section of ZA, as presented in Fig.10a. Both alumina and zirconia are therefore clearly defined.

Figure 5.10a. SEM micrograph of ZA (BE image)

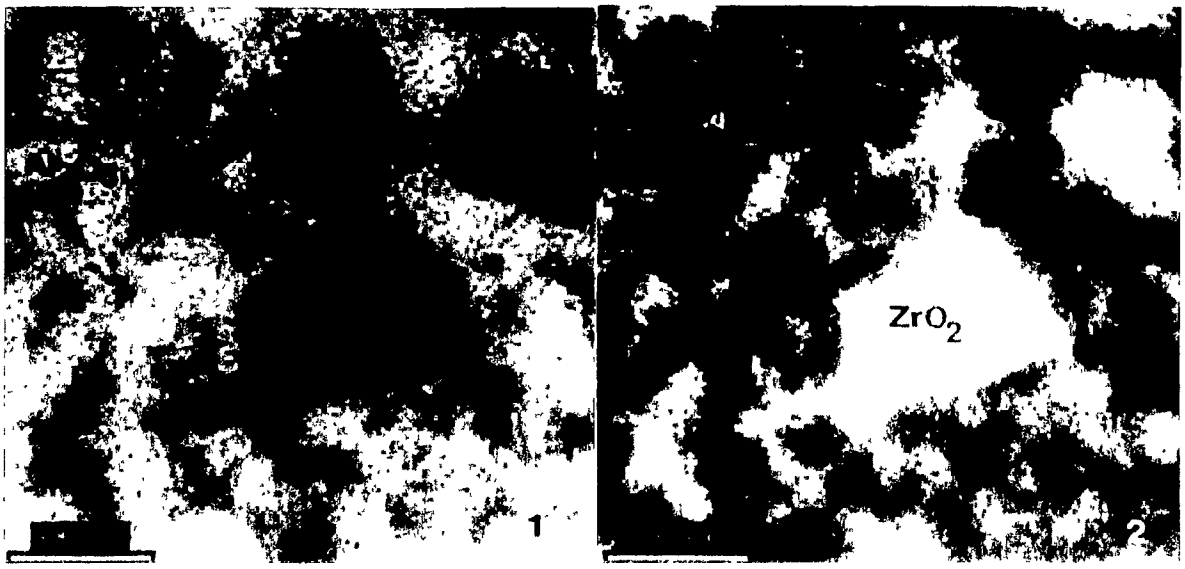

Figure 5.10b. X-ray map of ZA: (1) Al map (2) Zr map

5.1.3.2 Zirconia/Alumina/Titania

Fig.5.11a shows a polished SEM microstructure obtained for ZAT indicating a fine grain size. The resulting microstructure is fine with grains in the 1 to 5 μm range. Three different phases can be distinguished; alumina particles surrounded by a ZrO_2 matrix with a new phase being detected within the ZrO_2 phase and between the alumina grains. These phases can be identified on the X-ray map of the same sample taken at higher magnification (Fig.5.11b), and the combination of the Zr map and the Ti map confirms the presence of the $ZrTiO_4$ as detected previously by X-ray diffraction analysis.

5.1.3.3 Zirconia/Alumina/Silica

SEM micrographs of a typical ZAS sample are shown in Fig 5.12a. At least three phases are evident with a wide grain size distribution (1 to 10μm), the mullite matrix surrounds a dispersion of Al_2O_3 and ZrO_2 grains. From the micrograph, it is possible to distinguish two kinds of zirconia particles. Intragranular ones are enclosed in mullite grains and have a spheroidal morphology.

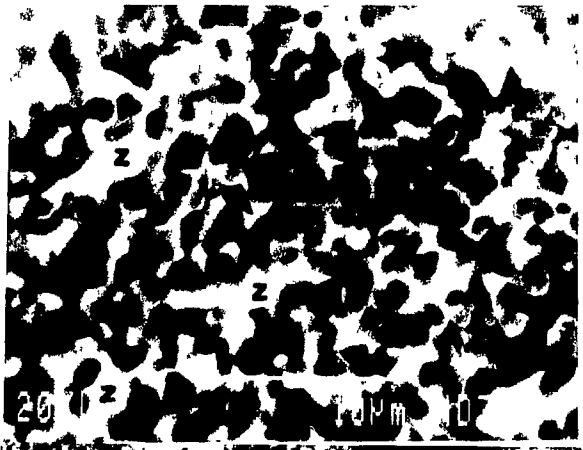

Figure 5.11a. SEM micrograph of ZAT section; z=ZrO_2; a=Al_2O_3; Z=$ZrTiO_4$.

Figure 5.11b. X-ray map of ZAT; (1) SEI; (2) Al map; (3) Zr map; (4) Ti map.

Figure 5.12a. SEM micrograph of ZAS section; a=Al_2O_3; z=ZrO_2; m=mullite.

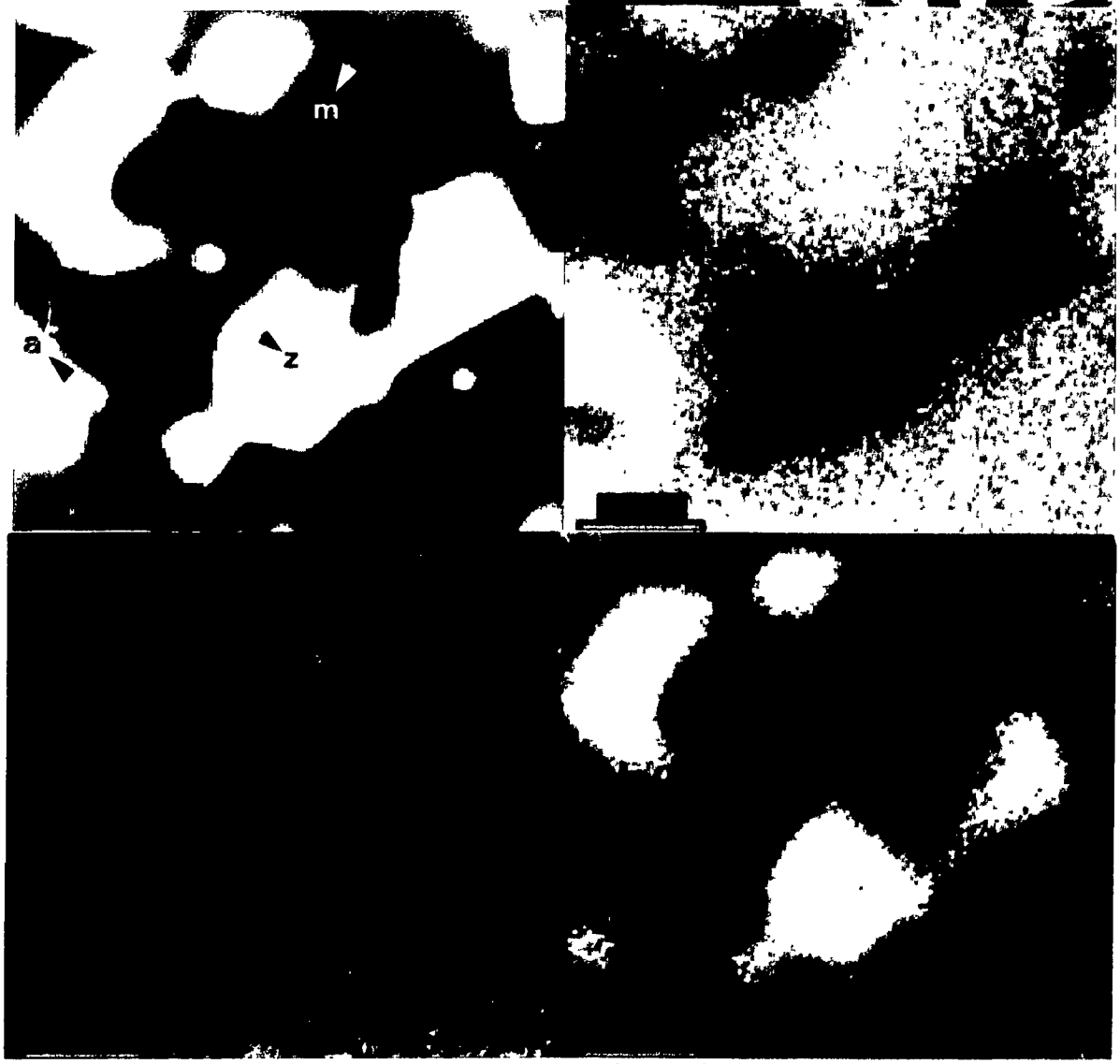

Figure 5.12b. X-ray map of ZAS; (1) SEI; (2) Al; (3) Zr; (4) Si. LM=lower Al_2O_3 content mullite.

The intergranular ones have a coarser faceted grain structure and are located between the mullite grain boundaries.

Fig.5.12b presents X-ray maps of the same sample, shown at higher magnification. In this Figure, ZrO_2, pure Al_2O_3, and a matrix of fine mullite crystallites can be detected. A zone corresponding to a lower alumina mullite ($3Al_2O_3.2SiO_2$) content is observed between ZrO_2 particles. It is suggested this zone could either result from the presence of a variation in the mullite composition in the range of $3Al_2O_3.2SiO_2$ to $2Al_2O_3.3SiO_2$, as reported by Di Rupo and Anseau[117], or from the occurrence of a SiO_2 phase which may be amorphous.

5.1.4 PHASE TRANSFORMATIONS DURING SINTERING

5.1.4.1 Phase Transformation in ZAT System

Based on the phase diagram (Fig.2.20), Al_2TiO_5, Al_2O_3, and ZrO_2 are the three phases coexisting in the eutectic system (A) (44wt% ZrO_2 + 42wt% Al_2O_3 + 14wt% TiO_2). The phase transformation should occur in the system during sintering by the following theoretical reaction:

$$44ZrO_2+42Al_2O_3+14TiO_2 \rightarrow 32Al_2TiO_5+24Al_2O_3+44ZrO_2 \qquad (5.1)$$

where the coefficients are given in wt%.

However, in no case was the Al_2TiO_5 phase detected either by X-ray diffraction analysis or by x-ray mapping, and the only additional phase which was observed is the compound $ZrTiO_4$. According to the ZAT equilibrium phase diagram[123], the occurrence of $ZrTiO_4$ is thermodynamically impossible when considering the eutectic composition (A) located in the compatibility triangle [ZrO_2-Al_2TiO_5-Al_2O_3].

Several assumptions can therefore been made regarding the phase transformation in ZAT system. During sintering, the system is actually not in equilibrium; phase changes, which occur 100°C below the eutectic melting point

(sintering temperature is 1500°C), are not exactly defined by the phase diagram representing the liquidus plane of the ternary system. The presence of the three phases $ZrTiO_4$, Al_2O_3, and ZrO_2 after sintering could be explained by sub-solidus phase relationships between ZrO_2 and TiO_2. Noguchi and Mizuno[124] have actually extensively investigated the system and a large region of solid solution between ZrO_2 and $ZrTiO_4$ has been observed below 1600°C (Fig.5.13).

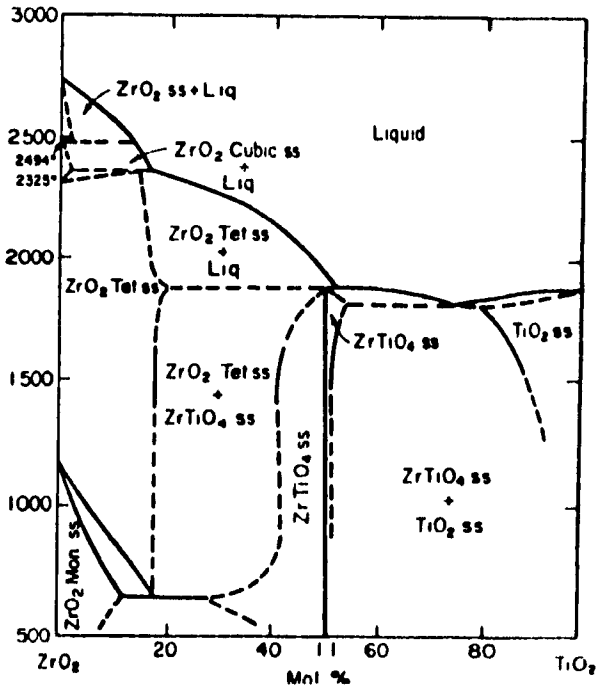

Figure 5.13. TiO_2-ZrO_2 phase diagram: solid-solution boundaries between ZrO_2 and $ZrTiO_4$.

The integrity of the ZAT phase diagram may be suspected; more especially the location or the existence of the eutectic (A) and the compatibility triangle [ZrO_2-Al_2TiO_5-Al_2O_3]. In Fig.5.14, an attempt is made to propose a new compatibility triangle defined by a [$ZrTiO_4$-Al_2O_3] Alkemade line.

Based on the X-ray and microstructural analyses, an experimental reaction, which is in agreement with Fig.5.14, can therefore be suggested:

$$44ZrO_2+42Al_2O_3+14TiO_2 \rightarrow 35.7ZrTiO_4+44Al_2O_3+22.3ZrO_2 \qquad (5.2)$$

where the amounts are given in wt%.

Finally, a calculation of the ZAT theoretical density based on equation (5.2) leads to 4.75 $g.cm^{-3}$; reaction (5.2) would therefore make sense since the measured theoretical density was previously estimated as 4.65 $g.cm^{-3}$ based on pycnometry.

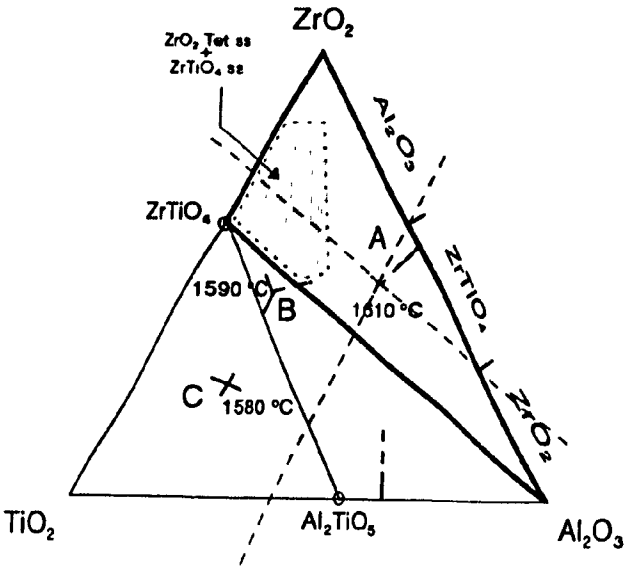

Figure 5.14. Schematic of ZAT phase diagram: proposition for a [ZrO_2-$ZrTiO_4$-Al_2O_3] compatibility triangle.

5.1.4.2 Phase Transformation in ZAS System

According to the phase diagram (Fig.5.15), mullite is the only new phase which should form in the ZAS system at the sintering temperature (1680°C). Indeed, Al_2O_3 and ZrO_2 phases do not react, as seen in section 5.3, and formation of zircon from ZrO_2 and SiO_2 is thermodynamically improbable[125]. Mullite forms according to the reaction:

$$3Al_2O_3+2SiO_2 \rightarrow 3Al_2O_3.2SiO_2 \qquad (5.3)$$

Considering the initial composition of ZAS (31wt% ZrO_2 + 53wt% Al_2O_3 + 16wt% SiO_2), equation (5.3) becomes:

$$31ZrO_2+53Al_2O_3+16SiO_2 \rightarrow 56.8(3Al_2O_3.2SiO_2)+12.2Al_2O_3 \qquad (5.4)$$

In this theoretical chemical reaction taking place during sintering, Al_2O_3 is in excess for 3:2 mullite formation. This equation does not accurately reflect the results obtained from bulk and microstructural analyses. The calculation of the

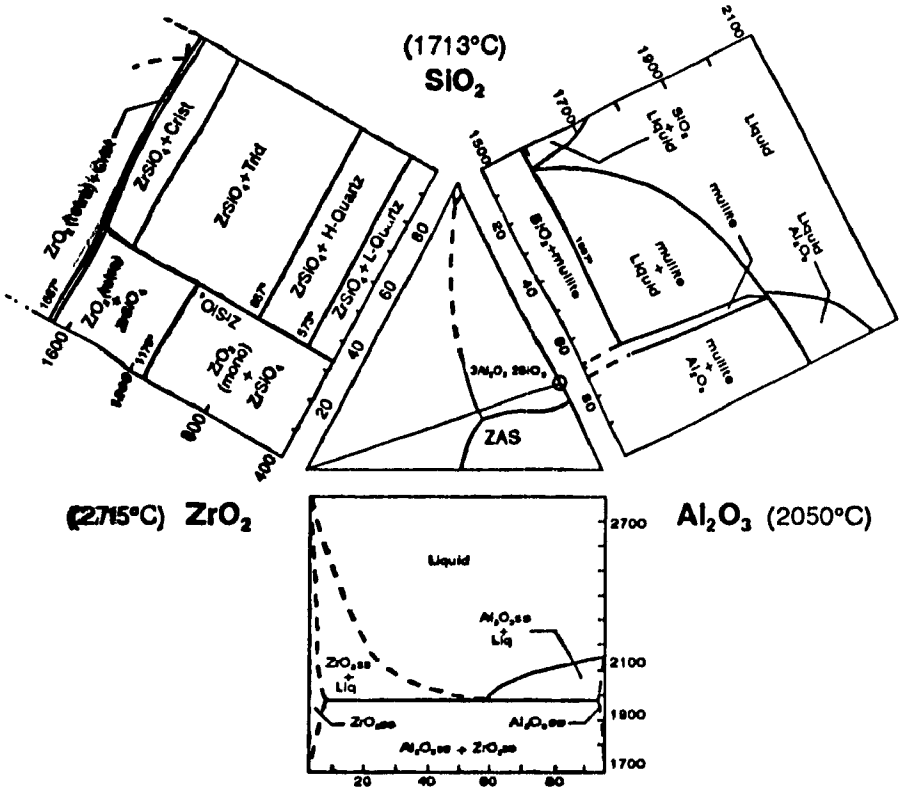

Figure 5.5. ZAS phase diagram and correponding binary diagrams.

theoretical density, based on equation (5.4), gives D_{th}= 4.09 g.cm^{-3}, whereas the theoretical density measured on sintered ZAS in the powder form is D_{th}= 3.5 g.cm^{-3}. It can therefore be assumed that Al_2O_3 and SiO_2 do not react completely, to form the 3:2 mullite, but react only partially, to produce a non-stoichiometric mullite and free SiO_2. The fact that the system has reached thermodynamic equilibrium conditions during sintering is the more likely explanation for this observation.

5.1.5 SUMMARY

Each ceramic material was densified by solid state sintering to achieve relative final densities over 96% of the theoretical density; open porosities were below 1.2%.

ZA materials presented a duplex ZrO_2/Al_2O_3 phase structure. ZrO_2, Al_2O_3, and $ZrTiO_4$ were found in ZAT materials by X-ray diffraction analyses and X-ray mapping; the phase distribution however was not in accordance with the phase diagram proposed in the literature. Finally, mullite formed in the ZAS system during firing; the final microstructure was also composed of un-reacted ZrO_2, Al_2O_3, and presumably amorphous SiO_2.

No quantitative or semi-quantitative analyses could be performed on the X-ray diffraction patterns because the major peaks of each phase were overlapping. Nevertheless, the expected relative amount of each phase in the ceramics can be estimated based on the chemical reactions taking place during sintering.

Densities and microstructural data on each material are reported in Table 5.3.

Table 5.3a. ZA: densities, porosity, and phases.

theoretical density	relative density* (%)		open porosity (%)	phases	relative amount† (wt%)
	green	final			
4.71	66	96	0.9	ZrO_2 Al_2O_3	42.6 54.7

SINTERED AT 1790°C FOR 2.5 HOURS

(*) calculated from the measured theoretical density
(†) expected

Table 5.3b. ZAT: densities, porosity, and phases.

theoretical density		relative density* (%)		open porosity (%)	phases (in wt%†)
calculated	measured	green	final		
4.7	4.65	60	96	1.1	ZrO_2** (44) $ZrTiO_4$ (35.7) Al_2O_3 (44)
SINTERED AT 1500°C FOR 2.5 HOURS					

(*) calculated from the measured theoretical density
(**) monoclinic and tetragonal
(†) expected

Table 5.3c. ZAS: densities, porosity, and phases.

theoretical density		relative density* (%)		open porosity (%)	phases (wt%†)
calculated	measured	green	final		
4.04	3.5	63	97	1.2	ZrO_2 (31) mullite (56.8) (SiO_2) Al_2O_3 (12.2)
SINTERED AT 1680°C FOR 2.5 HOURS					

(*) calculated from the measured theoretical density
(†) expected

Chapter 5:
RESULTS & DISCUSSION

PART 2: WETTING

This part of the thesis deals with the wetting behavior of the three ceramic materials with aluminum and aluminum alloys. Contact angles between the ceramic substrates and the alloys drops were measured *in-situ* using the sessile drop method as described in section 2.2.5 (Fig.5.16).

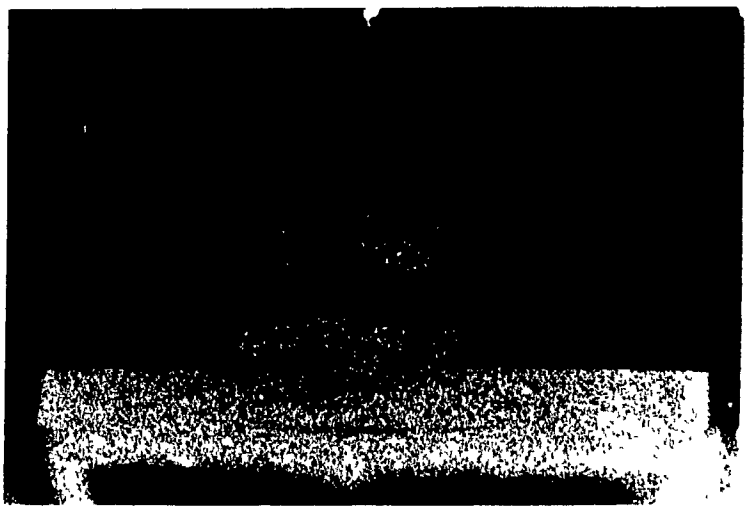

Figure 5.16. Typical *in-situ* picture of a sessile drop (ZAS/Al, 850°C)

5.2.1 ALUMINA/ALUMINUM SYSTEM

The alumina/aluminum system has been investigated many times in the temperature range 700°C to 1300°C[51-54]. However, the system appears to be very sensitive to changes in experimental parameters. Therefore, wetting experiments were performed to obtain reference contact angles between alumina and aluminum.

Experiments were conducted under vacuum (10^{-6} torr). Fig.5.17 shows the evolution of the contact angle with time at 900°C and 1000°C. After 20 minutes, the contact angle achieved 92° at 1000°C while staying very high at 900°C (~120°). This major difference in final contact angle is directly related to the presence of an oxide layer on the aluminum surface. At 1000°C , the system is above the critical temperature (950°C) for the penetration of liquid aluminum through the oxide layer which prevents any direct contact between the liquid phase and the substrate; a higher work of adhesion and a lower liquid metal surface energy lead, therefore, to a better wetting than at lower temperature. This behavior has been observed by many authors[52-55] who reported drops of the contact angle up to 70° after 1000°C, depending on the experimental conditions.

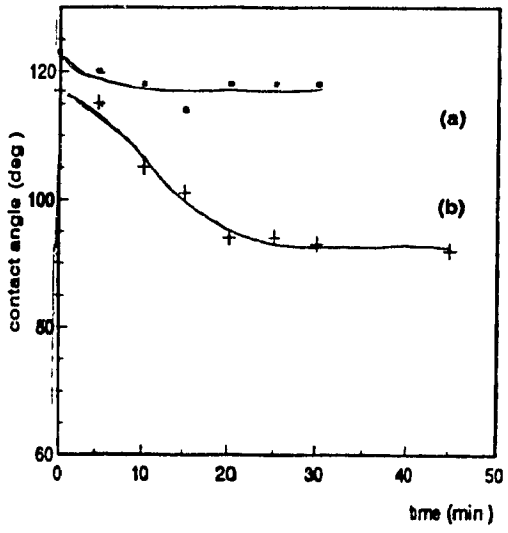

Time dependence of the contact angle.
Figure 5.17. Al_2O_3/Al:(a) 900°C, (b) 1000°C

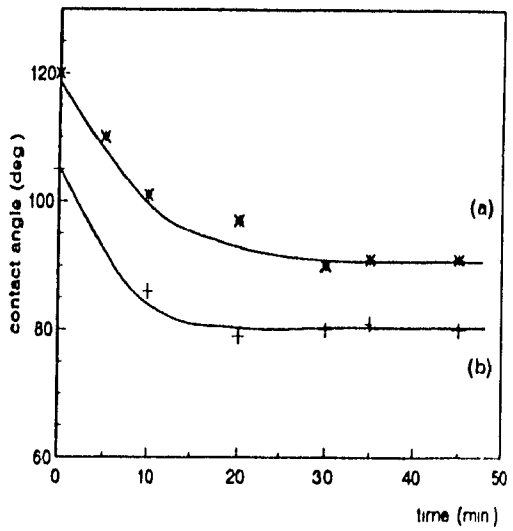

Figure 5.18 ZA/Al: (a) 900°C, (b) 1000°C

5.2.2 ZIRCONIA/ALUMINA CERAMIC

5.2.2.1 Evolution of ZA/Aluminum Contact Angle with Time

Fig.5.18 shows a typical isothermal variation of contact angle with time. Wettability data were obtained under vacuum at 900°C and 1000°C. In both cases, the system indicated a decrease of contact angle with time which reached an equilibrium value after 25-30 minutes. A wetting contact angle of 80° was achieved at 1000°C whereas only a slight wetting tendency was observed at 900°C. Here again, the higher value of θ at 900°C is likely due to the presence of an Al_2O_3 film around the drop.

5.2.2.2 Behavior of ZA/Aluminum-Silicon Alloy Systems

The effect of silicon alloying on the wetting behavior is illustrated in Fig.5.19, which shows the variation of contact angle with time at 900°C for Al-Si alloys. Experiments, conducted under vacuum for Al-5wt%Si (Al-5Si) and Al-10wt%Si (Al-10Si), demonstrate the significant influence of the silicon on the equilibrium contact angle. In fact, after 20 minutes at 900°C, ZA/Al-10Si presented a wetting contact angle of 83° which is comparable to that observed for pure Al at 1000°C. It can be noted that the variation of Si content in the aluminum did not have a great influence on the wetting behavior.

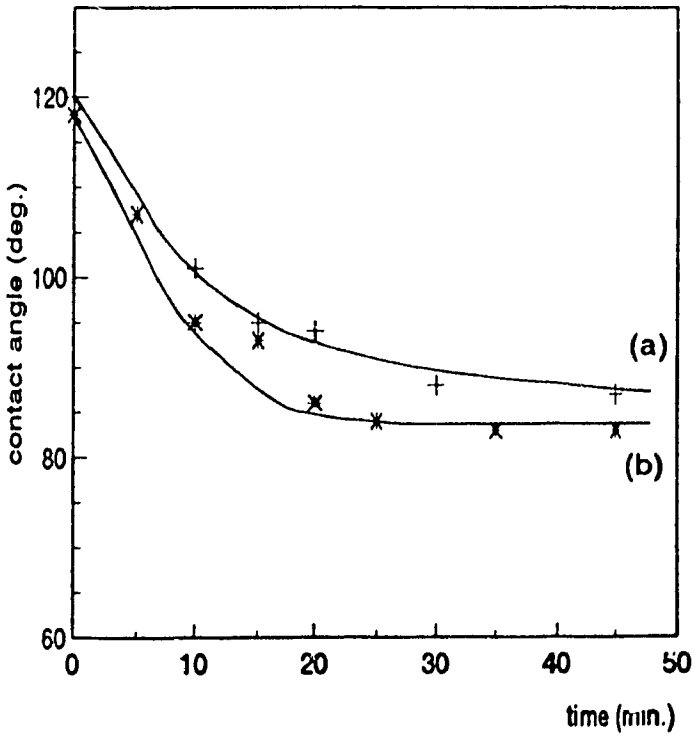

Figure 5.19. ZA/Al-Si systems (900°C):(a) Al-5Si, (b) Al-10Si.

5.2.2.3 Effect of Oxygen Partial Pressure on Contact Angle

In Fig.5.20 the dependence of the wetting angle on the oxygen partial pressure is shown for a temperature of 1000°C. Experiments were conducted under ultra high purity argon at atmospheric pressure, the furnace being previously evacuated to 10^{-3} or 10^{-6} torr. Contact angles of 84° and 105° were observed after 40 minutes for oxygen partial pressures corresponding to an initial vacuum of 10^{-6} and 10^{-3} torr, respectively. The huge difference in the final contact angles confirms that the oxide layer prevents the formation of the equilibrium shape of the aluminum droplet; the solubility of oxygen in aluminum is extremely low[126] and high oxygen pressures influence primarily the oxide layer thickness on the metal surface and therefore the wetting behavior.

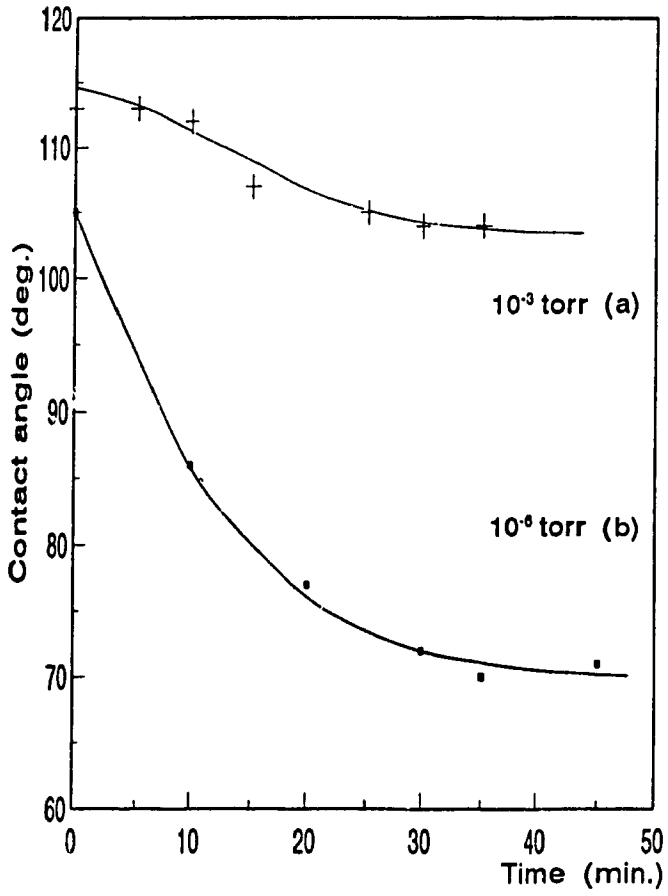

Figure 5.20. ZA/Aluminum.

Influence of the oxygen partial pressure on the contact angle (1000°C under ultra high purity argon):
(a) and (b) for O_2 partial pressures corresponding to an initial vacuum of 10^{-3} and 10^{-6} torr, respectively.

5.2.2.4 Interface Examination

The SEM micrograph presented in Fig.5.21 shows the cross section of the ZA/Al sessile drop cooled after holding at 1000°C for 45 minutes. The system had a very clean interface and no discernable voids could be observed between the two phases. The ZA phase did not present any change in the microstructure and no reaction was detected at the interface. Therefore, primary adsorption and mass transfer phenomena are most probably the driving force for wetting. Similar observations were made at the interface of a ZA/Al-10Si sessile drop obtained after 45 minutes at 900°C. The wetting improvement observed with Si additions in the aluminum could be then likely related to physical phenomena such as a decrease in the surface tension[73] or a reduction in the metal viscosity.

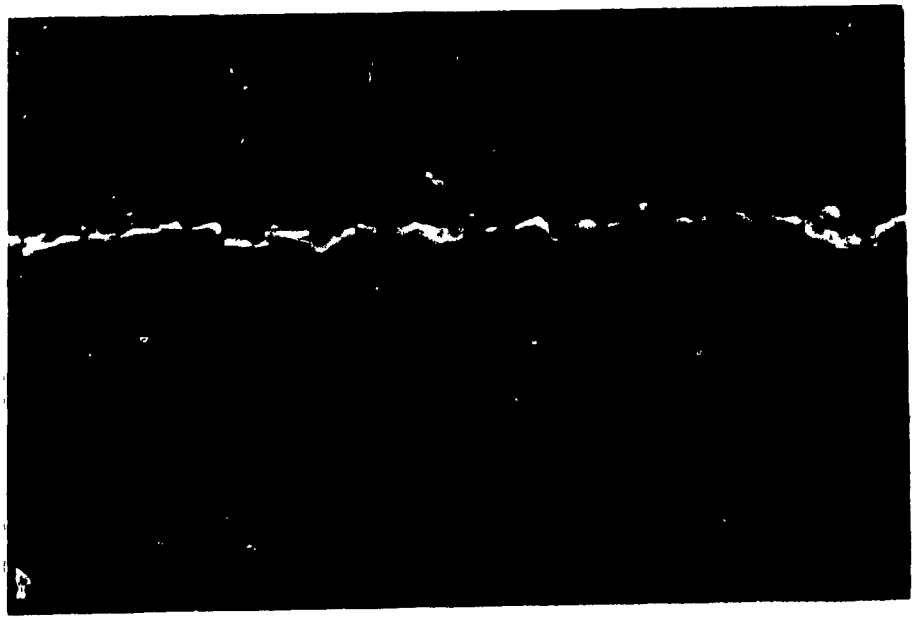

Figure 5.21. SEM micrograph of ZA/Al interface (1000°C, 45 min.)

5.2.3 ZIRCONIA/ALUMINA/TITANIA CERAMIC

5.2.3.1 ZAT/Aluminum System

The time dependence of the contact angles is illustrated by the curves for pure Al on ZAT at 900°C and 1000°C in Fig.5.22. In each case, the contact angle decreased during the first part of the experiment and tended to reach an equilibrium about 25 minutes after the holding temperature was attained. Similar to the ZA/Al system, the ZAT/Al system exhibited a wetting contact angle (θ= 79°) while incomplete wetting occurred at 900°C.

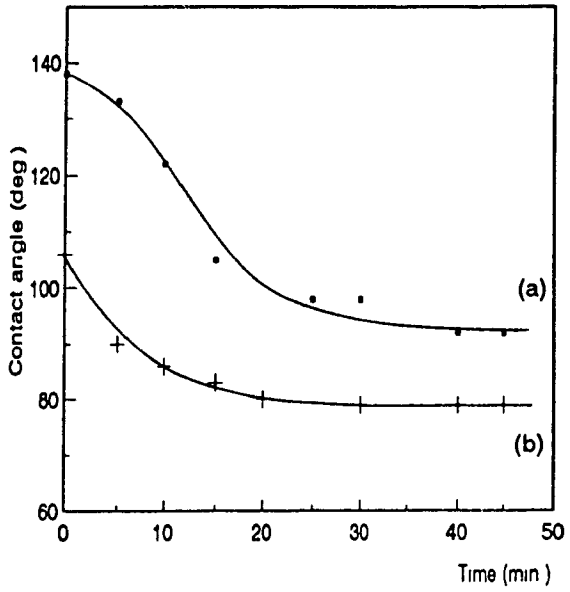

Figure 5.22. Evolution of the contact angle with time. ZAT/Al: (a) 900°C, (b) 1000°C.

5.2.3.2 ZAT/Aluminum-Silicon Alloy Systems

Effect of Si Content on Wetting Angle: Fig.5.23 shows the evolution with time of the contact angle at 900°C for Al-Si alloys. Again, in most cases the contact angle reached its equilibrium value after 25-30 minutes. The curves plotted for pure Al, Al-5Si, and Al-10Si demonstrate a significant influence of the presence of Si on the equilibrium contact angle. At 900°C, the contact angle for Al-5Si alloy is almost the same as that for pure aluminum against ZAT at 1000°C (θ= 86°). However, no notable increase in the wetting angle is apparent for contents higher than 5% Si (θ= 83° for Al-10Si alloy).

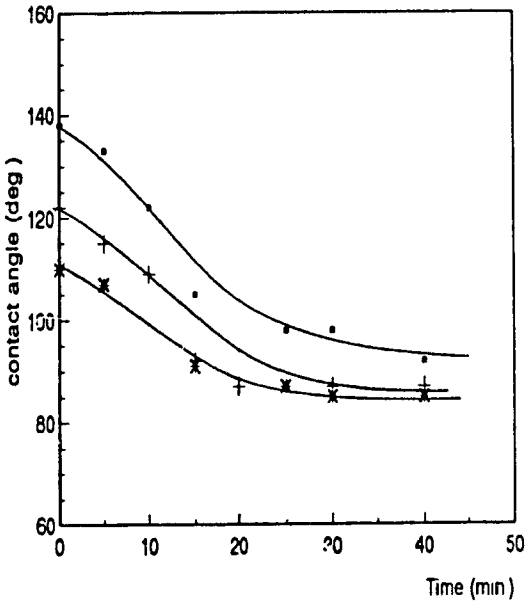

Figure 5.23. ZAT/Al-Si systems (900°C): (▪) pure Al, (+) Al-5Si, (*) Al-10Si

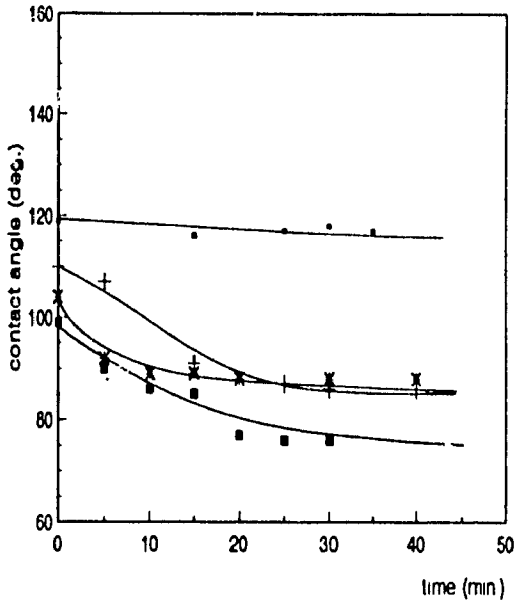

Figure 5.24. ZAT/Al-10Si: (▫) 800°C, (*) 900°C, (+) 950°C, (■) 1000°C

Effect of Temperature on Wetting Behavior: Fig.5.24 shows the time dependence of the contact angle for ZAT/Al-10Si system at different temperatures. Experiments were conducted under vacuum for temperatures ranging from 800°C to 1000°C. At 800°C, no decrease of the contact angle with time was noticed and the system exhibited a non wetting contact angle (θ= 120°) even after 40 minutes. The temperature dependence becomes significant above 900°C; after 15 minutes the system reached its equilibrium contact angles of 79° and 75° for 950°C and 1000°C, respectively.

A cross-over observed between the curves corresponding to 900°C and 950°C indicates either a slight variation in the experimental environment or a change in the t=0 time, leading to a curve shifting. However, this error does not affect the value of the equilibrium contact angle.

5.2.3.3 ZAT/Aluminum-Magnesium Alloy Systems

Wettability data for the Al-Mg alloys were obtained under high purity argon at atmospheric pressure since the high vapor pressure of Mg gave rise to rapid volatilization of the alloying element under vacuum. Experiments were performed at 850°C with Al-1.1wt%Mg (Al-1.1Mg) and Al-2.4wt%Mg (Al-2.4Mg) alloys. As shown in Fig.5.25, an abrupt decrease of the contact angle was observed for both alloys within the first 12 minutes at 850°C. Equilibrium wetting angles of 76° and 73° were achieved for Al-1.1Mg and Al-2.4Mg alloys, respectively.

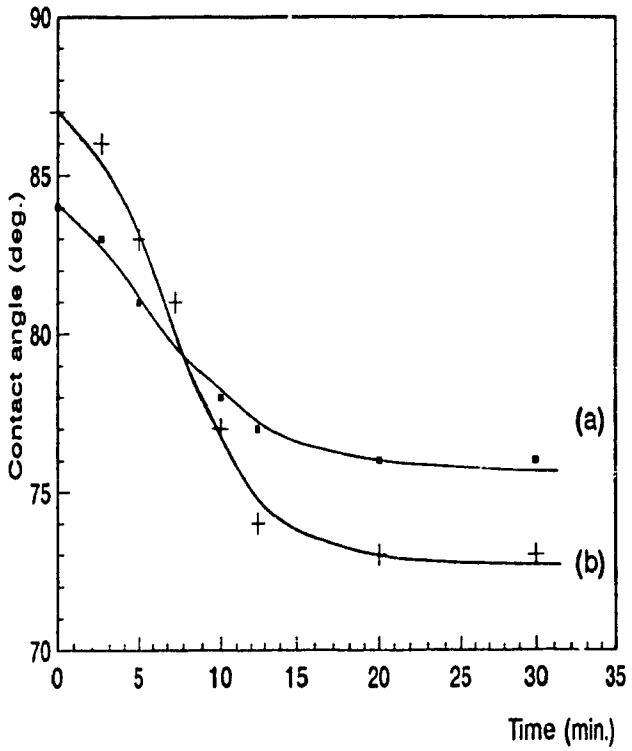

Figure 5.25. Time dependence curve for ZAT/Al-Mg systems (850°C): (a) 1.1Mg, (b) 2.4Mg.

This large drop of the contact angle, which is of the same order as that for ZAT/Al-10Si at 1000°C, might be explained by either physical phenomena such as changes in surface energies, or chemical phenomena; i.e. the formation of Mg based spinel could take place at the metal/ceramic interface[75], thereby promoting wetting.

5.2.3.4 ZAT/Aluminum-Magnesium-Silicon Alloy System

The time dependence curve obtained at 950°C for the Al-7Si-0.8Mg alloy (A357 series commercial alloy) can be seen in Fig.5.26; the curves corresponding to the Al-10Si and Al-1.1Mg (850°C) alloys are reported as a reference. The experiment was carried out under high purity argon at atmospheric pressure for the same

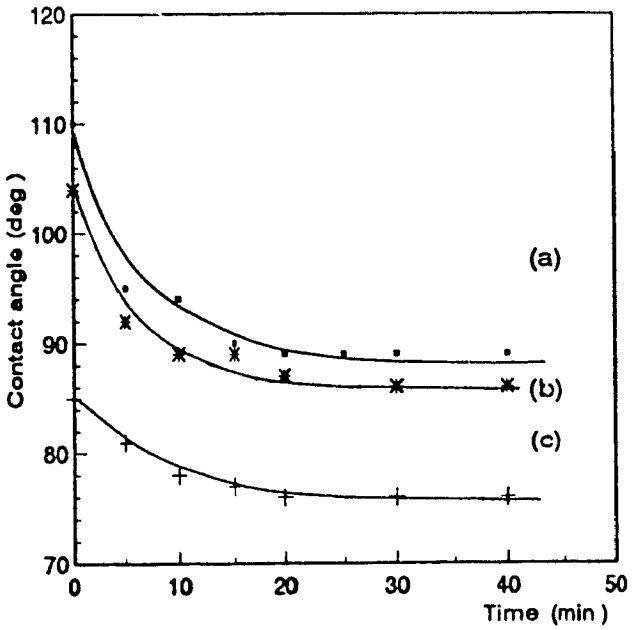

Figure 5.26. Time dependence of ZAT/Al-0.8Mg-7Si system at 950°C (a). (references Al-10Si (b), Al-1.1Mg (c)).

reasons mentioned previously. As expected, the rate of wetting was relatively fast and the system reached an equilibrium wetting angle of 87° after 15 minutes at 950°C. However, no significant difference in wetting behavior was observed compared to the Al-10Si alloy, and the equilibrium contact angle was not as low as expected. Consequently, two explanations might be suggested; the magnesium content was too low to induce any interfacial reaction or any modification of the alloy surface energies. On the other hand, a high evaporation rate could cause the disappearance of Mg from the alloy. The Mg evaporation rate actually depends on its diffusion rate in the alloy[127] and values increase exponentially with temperature.

5.2.3.5 Interface Examination and Discussion

An SEM cross sectional micrograph of the ZAT/Al sessile drop cooled after holding at 1000°C for 40 minutes is presented in Fig.5.27. This system exhibited a very clean, voidless interface and no interfacial reaction could be observed even at high magnification. The same observations were made for ZAT/Al-10Si; neither the ZAT substrates nor the alloy showed any change in microstructure.

Figure 5.27. SEM micrograph of ZAT/Al (1000°C for 40 minutes).

The difference in wetting behavior between ZAT/Al and ZAT/Al-Si alloys can therefore be attributed to physical phenomena. The surface tension of the metal phase affects considerably the contact angle of the non-reactive system. Addition of silicon to aluminum modifies the characteristics of the surface oxide layer and reduces the surface tension of the liquid, thereby influencing the wetting angle.

Time dependence of the wetting angle is often attributed to chemical reaction at the metal/substrate interface[38,50]. However, for systems such as ZAT/Al or ZAT/Al-Si, this phenomenon is only related to the necessity for the metal to break through the oxide layer to achieve intimate contact with the substrate.

The same observation can be made with ZAT/Al-Mg and ZAT/Al-Mg-Si systems. No reaction could be observed at the metal/ceramic interface and no spinel formation could be detected, even at high magnification on the SEM. The wetting enhancement observed as compared to the ZAT/Al system would therefore be

related to the aforementioned modification of the oxide layer and reduction of surface tension. Magnesium has a lower surface tension than aluminum at usual melting temperatures, and is actually known to weaken the diffusion barrier created by the Al_2O_3 film covering the aluminum[72].

5.2.4 ZIRCONIA/ALUMINA/SILICA CERAMIC

5.2.4.1 ZAS/Aluminum System

The wettability of ZAS/Al system was investigated under vacuum (10^{-6} torr). The evolution of the contact angle with time at 900°C and 1000°C is reported in Fig.5.28. As observed with previous systems, ZAS/Al presented only a slight wetting trend at 900°C and achieved an equilibrium contact angle of 90° after 30 minutes. At 1000°C, however, the system indicated a drastic decrease of the contact angle with time which reached its equilibrium value (θ= 74°) after 15 minutes.

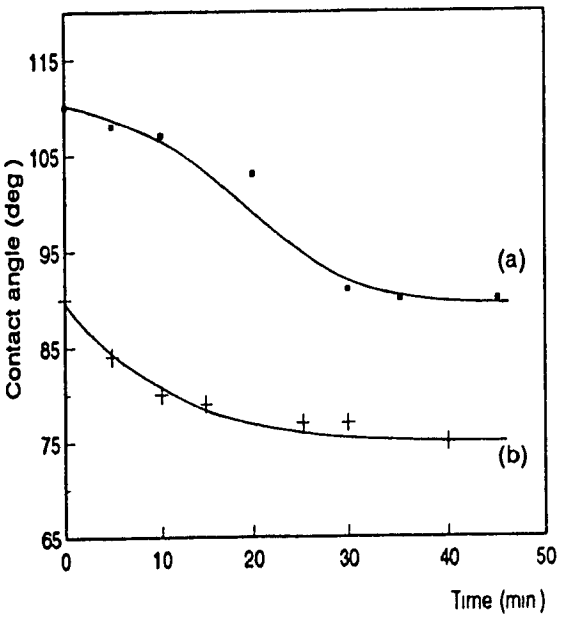

Evolution of the contact angle with time.
Figure 5.28. ZAS/Al system: (a) 900°C, (b) 1000°C.

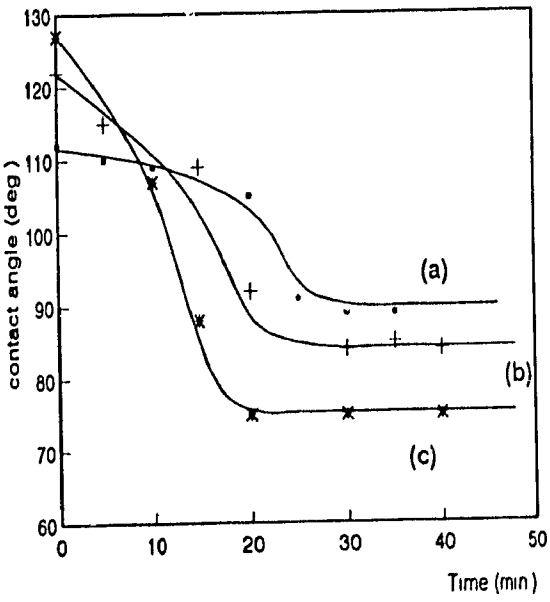

Figure 5.29. ZAS/Al-Si systems(900°C): (a) pure Al, (b) 5% Si, (c) 10% Si.

While both ZA/Al and ZAT/Al systems have shown a similar contact angle at 1000°C (θ~80°), the ZAS/Al system exhibited a much lower value for the same temperature; in addition to surface energy changes, chemical reactions at the metal/ceramic interface might therefore be part of the driving force for wetting.

5.2.4.2 ZAS/Aluminum-Silicon Alloy Systems

Effect of Si Content on Wetting Angle: Fig.5.29 shows the evolution of the contact angle with time at 900°C for Al-Si alloys. The curves reported on the graph for Al and Al-5Si indicate a decrease of the contact angle during the first 25 minutes of the holding temperature and form a plateau corresponding to θ= 90° and θ= 85°, respectively; a contact angle of 76° is achieved after 20 minutes for the Al-10Si. Here again, the presence of Si in the aluminum improves wetting as compared to pure Al. Moreover, unlike ZA/Al-Si and ZAT/Al-Si systems, ZAS/Al-Si systems demonstrate a significant composition (Si content) dependence of the contact angle and also probably rate of wetting, since a lower equilibrium angle is reached in a shorter time for a higher Si content.

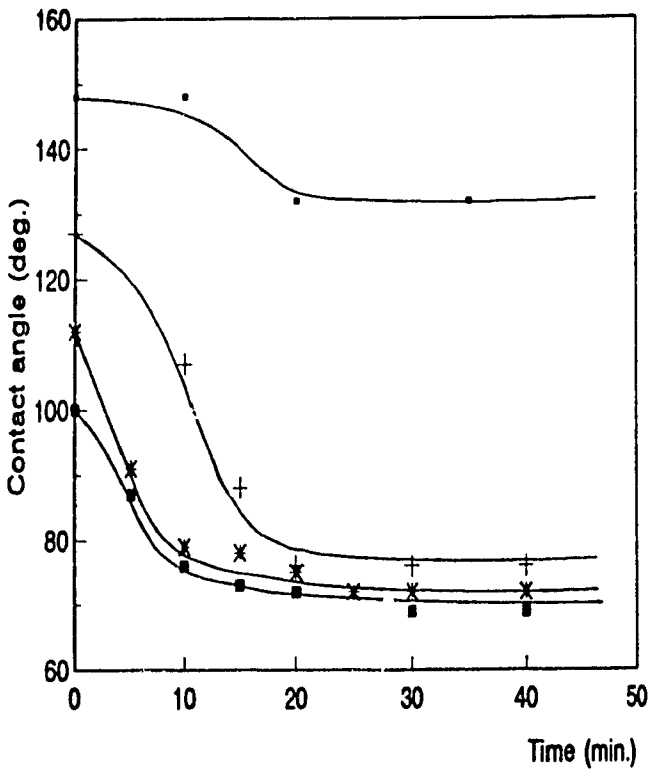

Figure 5.30. Effect of temperature on ZAS/Al-Si10 wetting behavior: (▫) 800°C, (+) 900°C, (*) 950°C, (■) 1000°C.

Effect of Temperature on Wetting Behavior: Fig.5.30 shows the evolution of the contact angle with time for Al-10Si at 800°C, 900°C, 950°C, and 1000°C. Although the system exhibited a

gradual decrease in the contact angle at 800°C, the change in the angle with time becomes significant with increasing temperature; an abrupt decrease of the contact angle can be observed above 900°C and the equilibrium value $\theta = 70°$ is reached after 15 minutes at 1000°C.

The ZAS/Al-Si system exhibits clearly lower contact angles than the ZAT/Al-Si at temperatures above 800°C and for the same Si contents. As mentioned previously, the occurrence of an interfacial reaction would likely explain the differences in wetting behavior between both systems.

5.2.4.3 ZAS/Aluminum-Magnesium Alloy Systems

Wetting data were collected for Al-1.1Mg and Al-2.4Mg at 850°C, under high purity argon at atmospheric pressure. As seen in Fig.5.31, both curves illustrate a sharp decrease of the contact angle which is reached after 15 minutes. The equilibrium values were 74° and 72° for 1.1wt% and 2.4wt% Mg contents, respectively. Moreover, the system exhibited wetting contact angles ($\theta = 86$-$87°$) even for the zero time at 850°C. This behavior (sharp drop of the contact angle and wetting observed after 15 minutes) is similar to that observed for ZAT against Al-Mg alloys under the same experimental conditions. Therefore, the wetting mechanism for ZAS/Al-Mg should be comparable to that of the ZAT-Al-Mg and ZAT/Al Mg-Si systems.

5.2.4.4 ZAS/Aluminum-Magnesium-Silicon Alloy System

An A357 commercial alloy (Al-Si7-Mg0.8) was used to investigate the influence of the combination of Mg and Si alloying elements on ZAS wetting behavior. Time dependence data, collected at 950°C under controlled atmosphere (high purity argon), are presented in Fig.5.32. The system reached an equilibrium contact angle of 79° after 20 minutes which is higher than expected, and especially higher than that reported for the Al-10Si alloy. The wetting behavior would therefore be more likely influenced by the presence of Si in the aluminum alloy than that of Mg.

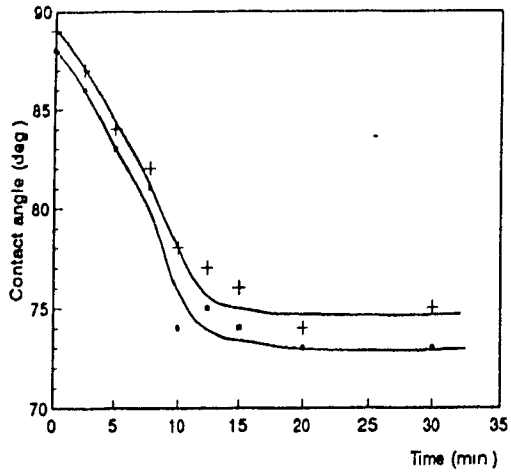

Time dependence of the contact angle.
Figure 5.31. ZAS/Al-Mg systems (850°C): (+) 1.1wt% Mg, (▪) 2.4wt% Mg.

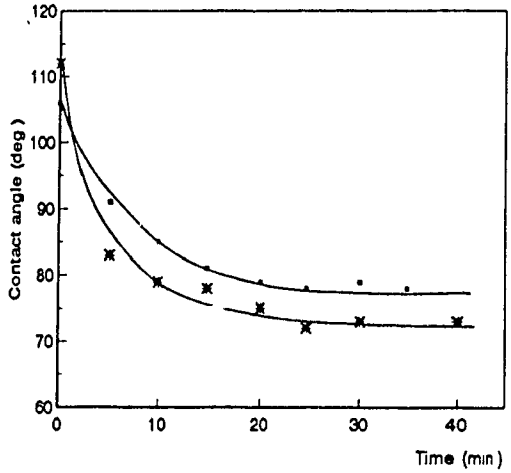

Figure 5.32. ZAS/Al-Mg0.8-Si7 (950°C) (reference: ZAS/Al-Si10).

5.2.4.5 Interface Examination

Prominent interfacial reactions were detected for both the ZAS/Al and the ZAS/Al-Si systems. In each case, a product consisting of discrete needle-like particles usually extending perpendicularly from the ceramic substrate appeared above 900°C and was evident by visual inspection of the specimens, as seen on Fig.5.33. Observations were performed on sessile drops cooled after 40 minutes at the holding temperature. However, selected drops quenched in air in the early stages of the experiment (within the first 10 minutes) exhibited the same kind of interfacial reactions.

Fig.5.33(a) shows the cross section of a ZAS/Al interface obtained at 1000°C. The needle-like particles were about 10 μm in thickness and the length ranged from 100 to 400 μm. Although a few of these particles were surrounded by metal only, most of them were attached to the ceramic phase in the polishing plane. Observation of segments of clean interface showed no discernible voids between the two phases. Significant modification occurred in the ceramic microstructure and a 60 μm thick reaction layer could be discerned in the interface region. Moreover, a crack induced by a metal/ceramic coefficient of thermal expansion mismatch was observed in the bulk ceramic in a zone corresponding to a drop perimeter and indicates good metal/ceramic bonding (Fig.5.33(c)).

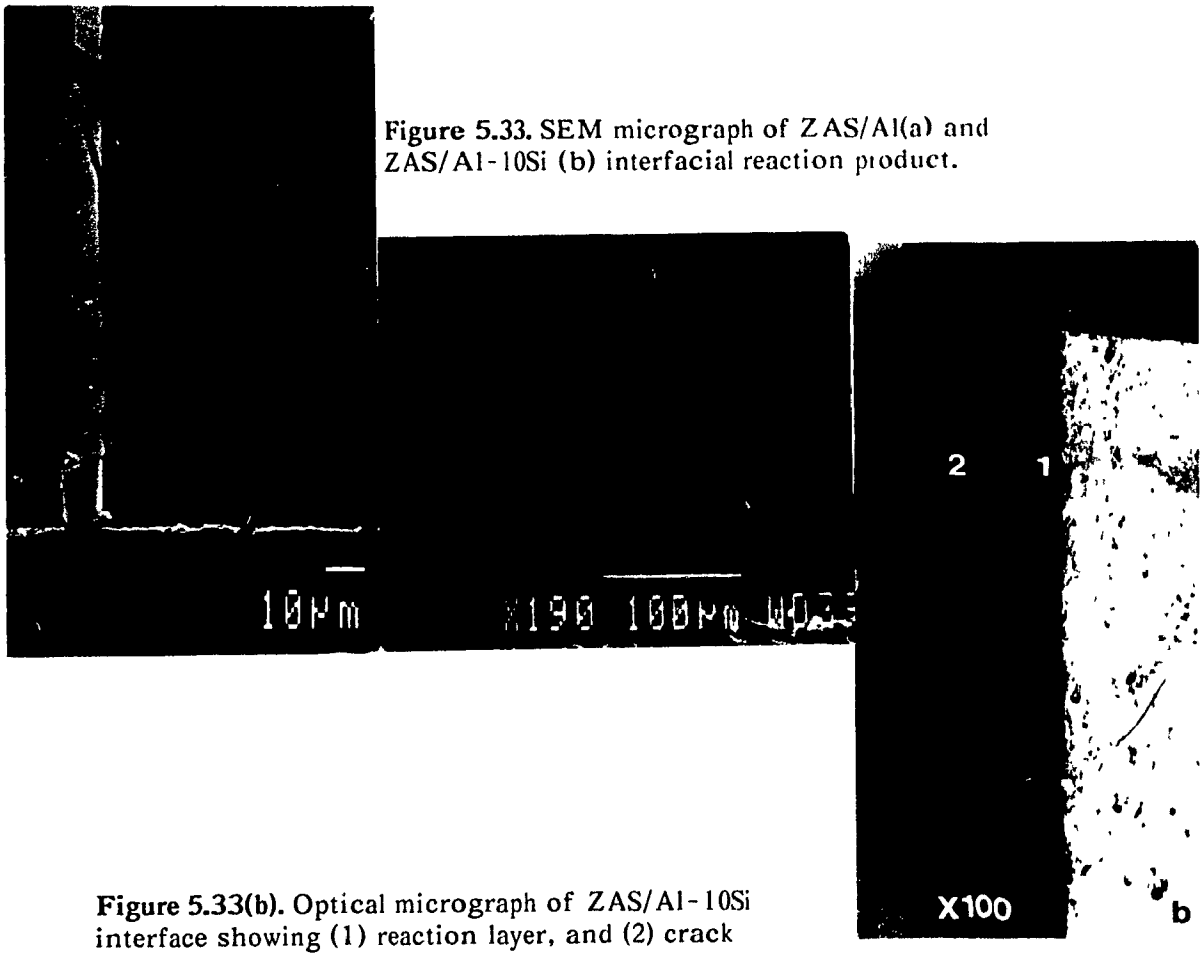

Figure 5.33. SEM micrograph of ZAS/Al(a) and ZAS/Al-10Si (b) interfacial reaction product.

Figure 5.33(b). Optical micrograph of ZAS/Al-10Si interface showing (1) reaction layer, and (2) crack in the ceramic.

Fig.5.33(b) presents the cross section of a ZAS/Al-10Si interface obtained at 1000°C. The extent of reaction in this specimen was greater than for pure Al. The average width of the plate-like faceted particles was 25 µm and the length ranged from 50 to 200 µm. In most of the cases, particles remained attached to the ceramic phase.

In addition, for Al, a 70 µm thick reaction layer was noticed at the metal/ceramic interface, and the same cracking phenomenon was observed in the bulk ceramic. No obvious modification of the eutectic phase was detected in the alloy.

In all cases, an interfacial reaction was observed between the metal and the ceramic in ZAS/Al and ZAS/Al-Si systems, which exhibited higher rates of wetting and lower equilibrium contact angles as compared to the corresponding ZAT systems under the same experimental conditions. The decrease of the contact angle with time and the improvement in wetting can therefore be related to a modification of the oxide surface layer and the surface tension of the alloy, as well as to interfacial reactions which lead to a decrease in the liquid/solid interfacial energy. In addition, since the reactions proceed as a function of time, they strongly influence the wetting kinetics.

No reaction product and especially no spinel could be detected at the ZAS/Al-Mg interface, even at high magnification. The wetting behavior was similar to that observed for ZAT/Al-Mg; the high degree of wetting and low equilibrium contact angle in this system is therefore also due to a decrease in surface energy induced by Mg additions to the Al, as discussed previously for ZAT/Al-Mg system. However, the presence of interfacial submicron size reaction product, hardly detectable by SEM, is not excluded.

Pronounced interfacial reactions were observed for the ZAS/Al-Mg-Si system. The product consisted of 15 μm wide, 50 μm long plate-like faceted particles; most of them were fragmented in their length. The interfacial compounds appeared similar to those encountered in ZAS/Al-Si system; moreover, no trace of spinel or Mg induced reaction could be detected. The similarity of these interfaces can therefore be related to the comparable wetting behavior of the two systems.

5.2.4.6 Interfacial Compound Characterization

Qualitative Characterization: Both the interfacial reaction products in ZAS/Al and ZAS/Al-Si systems were determined by qualitative EDS (Fig.5.34) to be intermetallic compounds composed of aluminum, zirconium, and silicon. However, the intermetallic product in ZAS/Al sample seemed to contain lower amounts of Si. No other elements were detected in these reaction products.

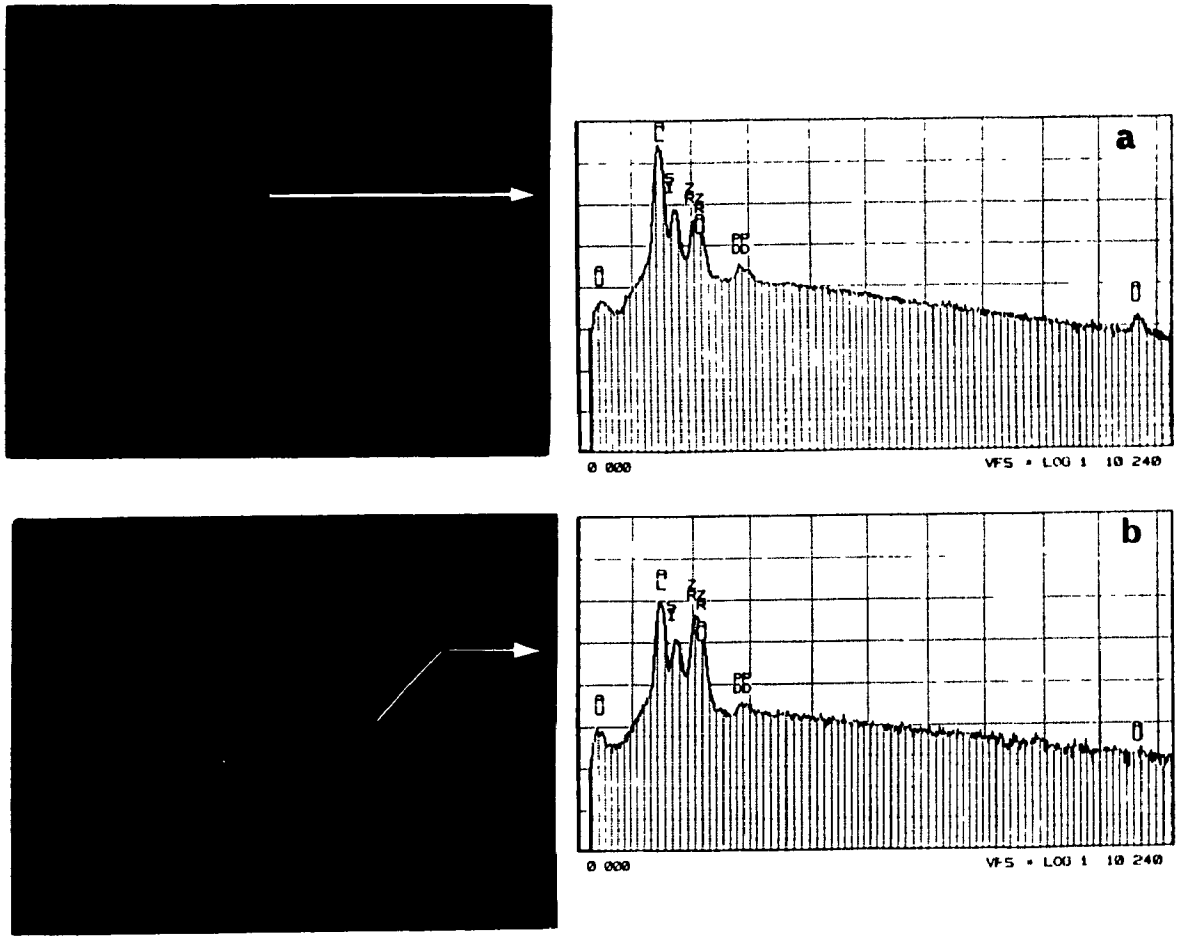

Figure 5.34. EDS analyses of the interfacial reactions: (a) ZAS/Al (1000°C), (b) ZAS/Al-10wt%Si (1000°C)

X-ray mapping, also used to generate atomic distribution maps of ZAS/Al and ZAS/Al-Si samples confirmed the EDS results (Fig.5.35). In both cases, a homogenous concentration of Zr and Al was found across the intermetallic particles. X-ray maps produced for Si showed a uniform distribution of the elements in ZAS/Al-Si intermetallic particle, whereas only traces could be detected in the ZAS/Al interfacial reaction product.

Figure 5.35. X ray map of ZAS/Al (a), and ZAS/Al 10Si interfacial compounds (b).

Quantitative Characterization: Quantitative electron probe microanalysis (EPMA) indicated that, in the case of ZAS/Al, the intermetallic compound contained 1 atom of zirconium per 3 atoms of Al, consistent with the stoichiometric compound of $ZrAl_3$; traces of Si (~1.5 at%) were also found in the compound. The metal phase consisted of pure aluminum in regions near and far from the reaction zone.

A high Si content (ranging from 14 to 16 at%) was analyzed in the intermetallic compound produced at the ZAS/Al-Si interface. Based on the determinations of Al and Zr, the closest fitting compositions for the reaction product were: $(ZrSi)Al_3$, $(Zr_2Si)Al_4$, or $(Zr_2Si)Al_3$; the Al:Zr ratio then ranges from 1.5 to 3. The Al-Si alloy did not present any change in composition in regions far from the interfacial reactions. However, Si depletion could be detected close to the intermetallic particles.

The interfacial reaction products of ZAS/Al-Si-Mg sample were found to be the same type of intermetallic compounds as analyzed in the previous system. The Mg content was below the limit of detection of the EPMA (<0.3%).

5.2.4.7 Formation of the Intermetallic Compounds

Energy dispersive spectroscopy, X-ray mapping, and electron probe microanalyses identify the interfacial reaction product in the ZAS/Al and ZAS/Al-Si systems as a $ZrAl_3$ based intermetallic compounds. The only noticeable difference between these two systems is the Si content of the particles.

$ZrAl_3$ occurs as a b.c. tetragonal structure (a=4.103 Å and c=17.320 Å)[128] and, according to the phase diagram (see Fig.5.36), is the first intermetallic compound to form in equilibrium with aluminum. When the Zr:Al ratio decreases, the next compounds to form are $ZrAl_2$ and Zr_2Al_3. The phase diagram also predicts equilibrium of both liquid and solid aluminum with $ZrAl_3$. Therefore formation and growth might occur in the solid state upon cooling of the sessile drop. One of the most likely mechanism for $ZrAl_3$ formation is by the reaction reported by Isaacs *et al*[129]:

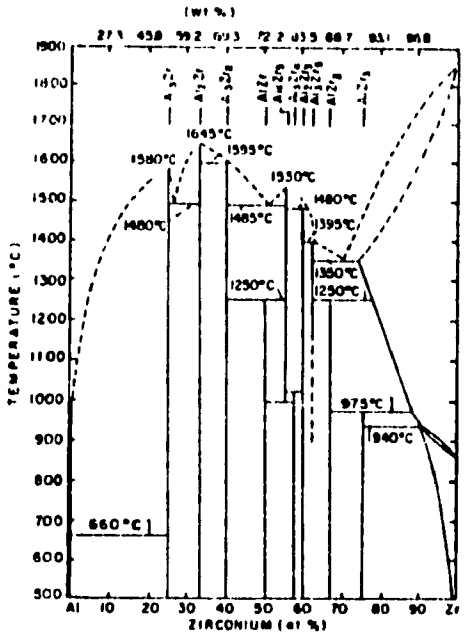

Figure 5.36. Zr/Al phase diagram.

$$\frac{13}{3}Al_{(l)}+ZrO_{2(s)} \rightarrow \frac{2}{3}Al_2O_{3(s)}+ZrAl_{3(s)} \qquad (5.5)$$

The Gibbs free energy for this reaction is given by:

$$\Delta G = -271.85+(0.329T)+(1.31.10^{-6}T^2) +(7.54.10^3/T)-(0.0308.T.\ln(T)) \qquad (5.6)$$

A ΔG of -145kJ/mol was calculated within the experimental temperature range (900-1000°C) and indicates that the formation of $ZrAl_3$ would be expected on a thermodynamic basis.

Based on equation (5.6), the formation of $ZrAl_3$ base intermetallic compounds appears to be strongly related to the presence of ZrO_2 in the ceramic substrate; Si and Zr would diffuse from the substrate to the Al alloy, and at a later stage, through the aluminum alloy to the growing intermetallic particles. This is confirmed by the observation of a Zr and Si depleted zone and a high Al content zone in the ceramic interfacial region, illustrated by the X-ray maps shown on Fig.5.37 of a reacted ZAS/Al-Si interface. The enhanced Si content found in the reaction product at the ZAS/Al-Si or ZAS/Al-Mg-Si interfaces is most likely derived from the diffusion of Si from the alloy to the intermetallic particles.

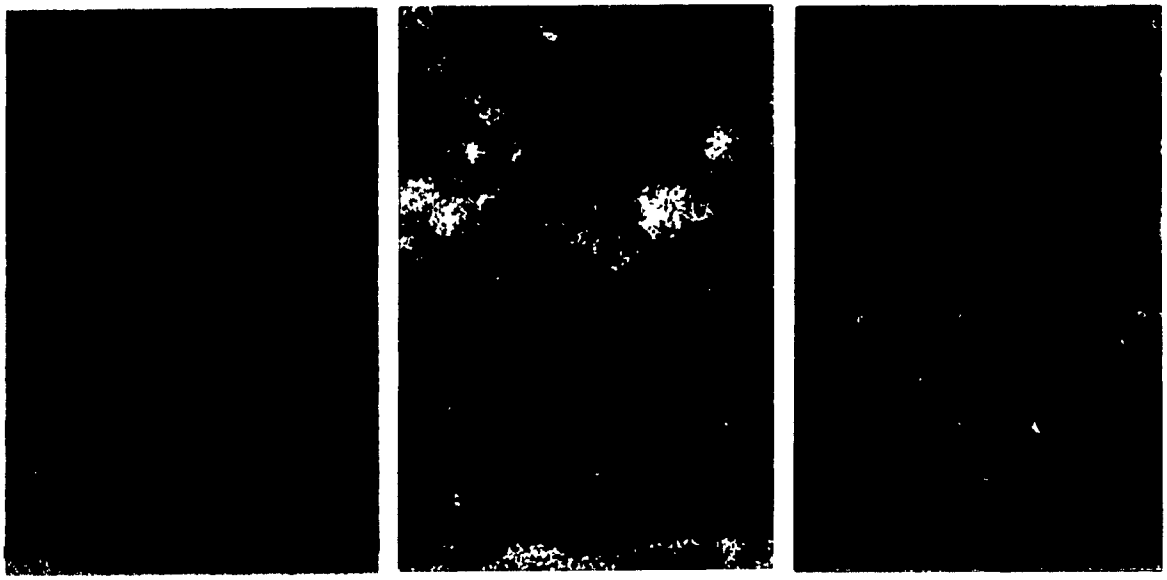

Figure 5.37. Depletion zone at the ZAS/Al-Si interface. X-ray maps of: (a) Al, (b) Si, (c) Zr.

Nevertheless, in no case was any reaction observed either with ZA/Al or with ZAT/Al and ZAT/Al-Si systems. The fact that both substrates (ZA and ZAT) contain ZrO_2 phase leads to the conclusion that SiO_2 plays a major role in the intermetallic reaction. Few thermodynamic data are available on the systems under

study. Therefore, although some hypotheses can be made, it is difficult to predict an exact mechanism for compound formation.

SiO_2 has a strong tendency to form mullite in the presence of Al_2O_3. However, it has been proposed (see section 5.1.4) that ZAS ceramic could contain non-stoichiometric mullite or unreacted SiO_2. The Al_2O_3 which forms as a product of reaction (5.5) would then either combine with non-stoichiometric mullite or SiO_2, which would therefore promote the formation of the $ZrAl_3$ or $(Zr_xSi)Al_y$ intermetallic compounds. Based on equation (5.5), possible mechanisms are proposed in Fig.5.38.

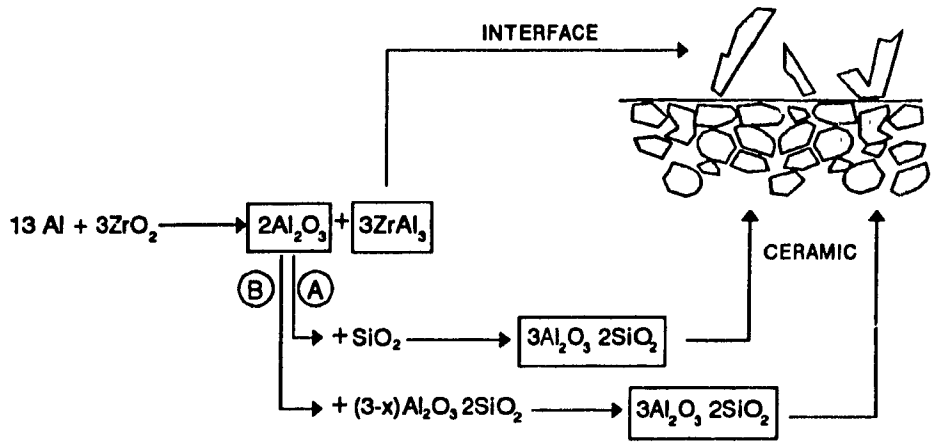

Figure 5.38. Proposed mechanisms for intermetallic compound formation.

The SiO_2 reaction (A) is the most likely to occur, since it is thermodynamically favourable in all cases, but relies on the potential amount of free SiO_2 in the ceramic.

Unlike reaction (A), the mullite reaction (B) mechanism is only thermodynamically possible if the non-stoichiometric mullite is present in a Al_2O_3:SiO_2 ratio of less than 1.5:1; according to the SiO_2-Al_2O_3 free energy diagram, whose simplified interpretation is given in Fig.5.39. Its combination with Al_2O_3 would consequently result in a more stable compound.

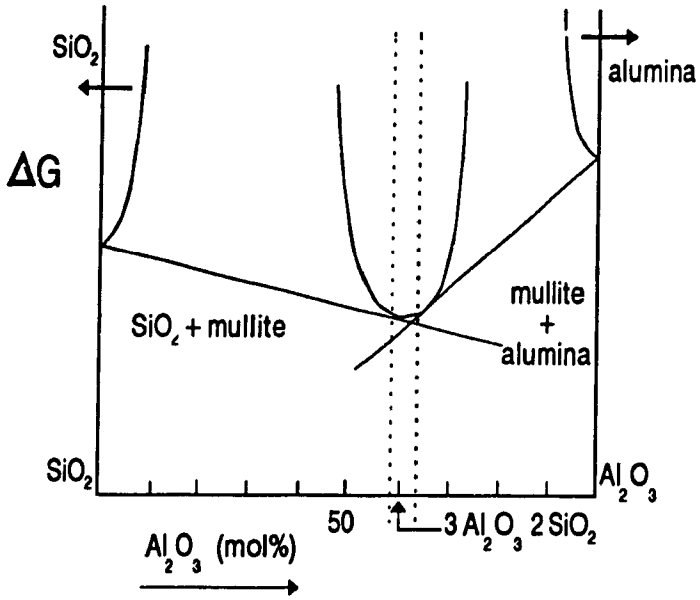

Figure 5.39. Simplified interpretation of the SiO_2-Al_2O_3 free energy diagram.

5.2.5 SUMMARY: WETTING ENHANCEMENT

5.2.5.1 Influence of the Nature of the Ceramic

It is clear that wetting behavior is strongly influenced by the nature of the ceramic substrate. The time-dependent curves, reported in Fig.5.40 for alumina, ZA, ZAT, and ZAS with pure aluminum at 900°C, illustrate this phenomenon.

Alumina/aluminum is known as a non-wetting system for temperatures below 1000°C or even 1100°C[22,29], because of the presence of a strong oxide layer at the metal surface. However, addition of ZrO_2 to Al_2O_3 brings on liquid-solid interfacial energy changes due to adsorption and diffusion of components from the bulk phase to the interface, and therefore leads to another wetting equilibrium.

A significant decrease of the equilibrium contact angle is observed when adding SiO_2 to the eutectic ZA system. This wettability improvement is due to reaction between the liquid Al and the substrate, consisting of the diffusion of elements from one phase to the other and the reaction of components to form new interfacial compounds. Such behavior involves a much larger decrease of the liquid-solid interfacial energy of the system than simple adsorption.

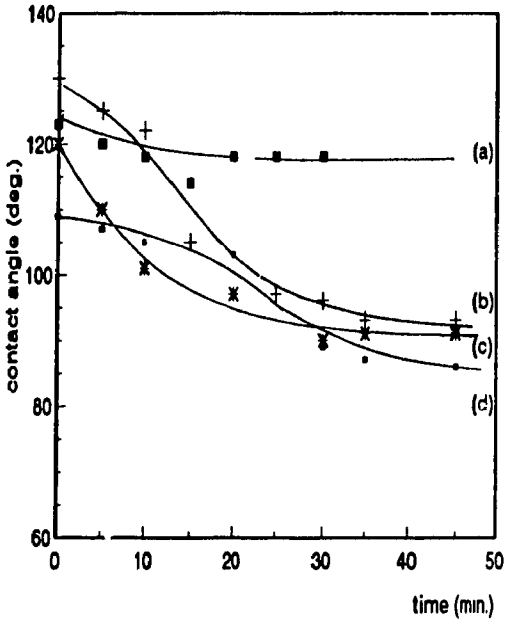

Figure 5.40. Influence of the nature of ceramic on wetting (pure Al, 900°C): (a) Al_2O_3, (b) ZA, (c) ZAT, (d) ZAS.

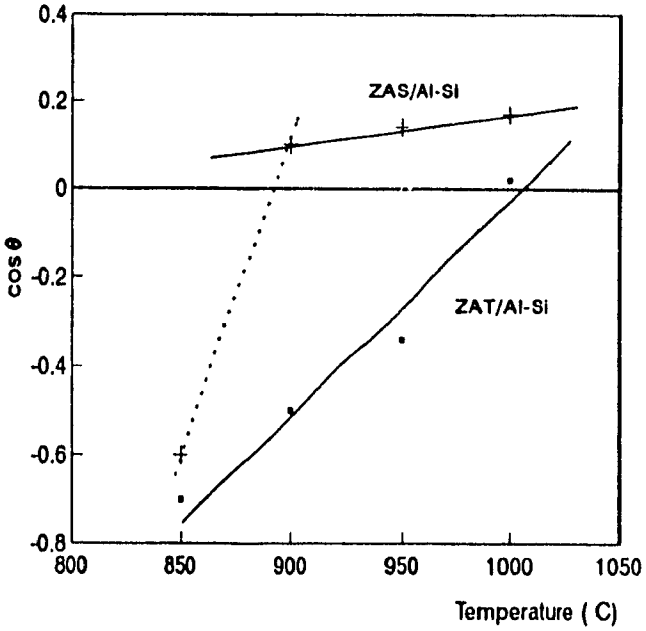

Figure 5.41.variation of cos θ with temperature.

5.2.5.2 Effect of Temperature

As a general rule, wetting angles tend to decrease with increasing temperature. As mentioned previously, this effect is partly physical, connected with transformations in the oxide layer on the metal surface and therefore with a decrease in surface energies, partly chemical (due to more rapid adsorption), and finally due to diffusion phenomena at the metal-ceramic interface and potential chemical reactions which might occur at this interface.

A linear relation between cos θ and temperature is generally applicable for liquid metal/ceramic systems and an example is given with ZAT/Al-Si system, as shown in Fig.5.41. However, when interfacial reactions occur, which involve a large decrease of the free energy of the system, the interfacial energy γ_{lv} no longer varies linearly until equilibrium is reached. As a result, the relation between cos θ and T is linear only in the temperature range where an equilibrium is achieved, as seen with ZAS/Al-Si system whose cos θ temperature relationship is also reported in Fig.5.41.

5.2.5.3 Addition of Elements to the Liquid Metal

Element additions usually provoke a reduction of the surface tension of the liquid, decreasing of the solid-liquid interfacial energy or lead to chemical reactions at the solid-liquid interface.

Mg and Si additions to aluminum are actually known to modify the characteristics of the oxide layer on the Al metal surface[63,64,67]. These data correlate well with wetting angle data, in the sense that the transition temperature from non-wetting to wetting as well as the equilibrium wetting angle are decreased by these additions, as seen in Fig.5.42 which compares the wetting behavior of ZAS with pure Al, Al-10Si, and Al-2.4Mg, at 900°C.

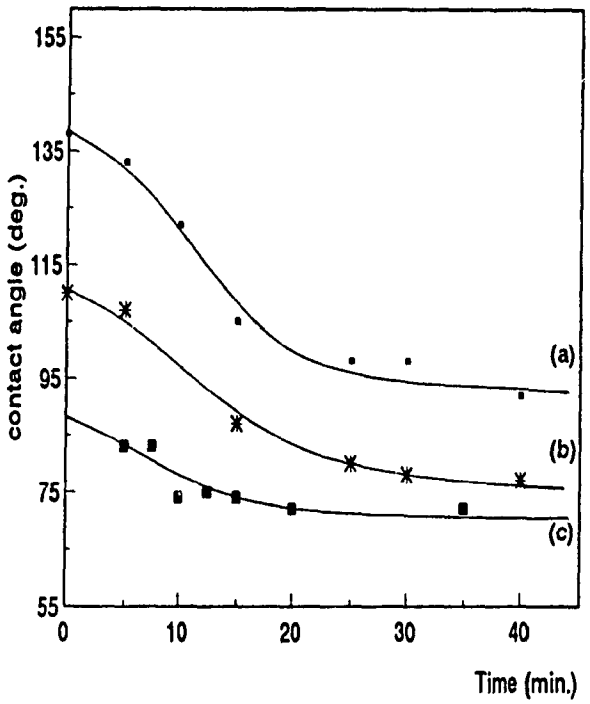

Figure 5.42. Effect of the alloying element on the wetting behavior (ZAS, 900°C).

5.2.5.4 Optimum system

Values of equilibrium contact angle obtained for different experimental systems are reported in Table 5.4.

ZAS base systems generally exhibit the best wetting contact angle. However, in most cases intermetallic compounds are obtained at the metal-ceramic interfaces. With a view to fabricating metal/ceramic composites, reactions between ceramics and metal phases are clearly undesirable since intermetallic compounds can embrittle the interface or damage the reinforcement.

Table 5.4. wetting behavior of the different experimental systems

		ZA	ZAT	ZAS
Al	wetting angle 900°C,1000°C	91°, 80°	93°, 79°	90°, 74°
	interface	clean	clean	$ZrAl_3$
Al-10Si	wetting angle 900°C,1000°C	83°, --	86°, 75°	76°, 70°
	interface	clean	clean	$(Zr_xSi)Al_y$
Al-2.4Mg	wetting angle (850°C)		73°	72°
	interface		no observed reaction	no observed reaction
Al-Mg-Si	wetting angle (950°C)		87°	79°
	interface		no observed reaction	$(Zr_xSi)Al_y$

A cleaner interface is therefore preferred to a lower wetting angle. In this way, the ZA and ZAT base systems, despite higher wetting angles, or the ZAS/Al-Mg systems appear to be the most promising combination, with regard to obtaining a good mechanical bond at the metal-ceramic interface.

The ZA composition is probably the most interesting ceramic in terms of fiber fabrication since the system presents a very simple phase relationship which leads to binary microstructures and thereby to a material with good mechanical properties. The high melting point of the eutectic composition remains the only limitation for certain fiber fabrication processes such as melt extraction; in this case, the difficulty could be overcome by using a Laser as a heat source.

Finally, it is worth noting that these experiments for the systems studied are not necessarily representative of actual experimental conditions for composite fabrication. In fact, the modification of several parameters, such as the shape and the microstructure of the ceramic phase, the experimental environment, and the way the metal and the ceramic phases are brought into contact, will have a strong effect on the wetting behavior of the metal-ceramic system.

Chapter 6:
CONCLUSIONS & RECOMMENDATIONS

6.1. CONCLUSIONS

Four major variables were tested to study the wetting behavior of definite ceramic/metal systems. Variables include holding time, melt temperature, alloy and ceramic compositions.

1. Eutectic zirconia/alumina ceramics (ZA, 38 mol% ZrO_2 + 62 mol% Al_2O_3) were sintered at 1790°C for 2.5 hours to achieved 96% of the theoretical density (D_{th}= 4.7). No phase transformation occurred during firing and ZA specimens presented a relatively homogeneous microstructure composed of a mixing of the two initial ZrO_2 and Al_2O_3 phases.

2. Zirconia/alumina/titania ceramics (ZAT, 37.8 mol% ZrO_2 + 43.6 mol% Al_2O_3 + 18.6 mol% TiO_2) were sintered at 1500°C for 2.5 hours to achieved 96% of the measured theoretical density (D_{th}= 4.65). Al_2O_3 and $ZrTiO_4$ phases were found in ZAT. In addition, non reacted ZrO_2 phase, made of both tetragonal and monoclinic forms, was detected by X-ray diffraction analysis; the phase diagram,

however, predicted the presence of Al_2TiO_5. Subsolidus relationships between constituents were considered to explain the unexpected presence of these phases; restraints were also made with respect to the integrity of the phase diagram.

3. Zirconia/alumina/silica ceramics (ZAS, 24.4 mol% ZrO_2 + 50 mol% Al_2O_3 + 25.6 mol% SiO_2) were sintered for 2.30 hours at 1680°C and reached 97% of the measured theoretical density (D_{th}= 3.5). An examination of ZAS specimen microstructure clearly revealed a mullite matrix surrounding dispersed Al_2O_3 particles and ZrO_2 grains. However, a significant difference between the measured theoretical density and the calculated one (D_{th}= 4.04) was observed, and low alumina content zones were detected in the mullite ($3Al_2O_3.2SiO_2$) phase; these zones are believed to result from the presence of either non-stoichiometric mullite or an amorphous SiO_2 phase.

In all cases, substrates exhibited a surface porosity less than 1.2%, which is suitable for wettability experiments.

The results obtained for the different metal/ceramic systems appeared to be strongly dependent on the experimental conditions, and especially on the furnace atmosphere; the results demonstrated that an oxygen partial pressure of $\sim 10^{-6}$torr is the limit for obtaining relevant wetting data with aluminum alloys.

4. For any ceramic substrate, a temperature over 950°C was necessary to observe an equilibrium wetting angle less than 90° with pure aluminum; under the present experimental conditions, 950°C is believed to be the critical temperature for the penetration of liquid aluminum through the surface oxide layer.

5. By alloying the aluminum, wetting could be observed at lower temperatures (θ= 76-86° at 900°C for Al-10wt%Si, $\theta \sim 72°$ at 850°C for Al-2.4wt%Mg); Si and Mg additions would modify the characteristics of the oxide layer on the metal surface, decrease the aluminum liquid-vapor interfacial energy γ_{lv} , and consequently improve wetting.

6. The wetting behavior is strongly related to the nature of the ceramic substrate. ZAS specimens reacted with molten Al alloys over 900°C to produce

$ZrAl_3$ and $(Zr_xSi)Al_y$, growing normal to the metal/ceramic interface in the form of faceted needles or platelets. The presence of the intermetallic particles induced decreases of the solid-liquid interfacial energy γ_{sl} which resulted in significant improvements of the equilibrium contact angles.

6.2 RECOMMENDATIONS FOR FURTHER WORK

1. Sintering experiments could be performed on ZAT systems having different compositions in order to clarify the phases present in the material after firing.

2. Wetting behavior experiments could be further investigated:

- By changing the amount of the third component in the ternary oxide system (based on the same ZrO_2:Al_2O_3 ratio).

- With high Mg content Al alloys or with other class of Al alloys (using strong oxide formers as additive elements).

3. A more comprehensive study on the production of the interfacial compounds could be carried out:

- By annealing a solidified sessile drop below the Al melting point to promote or expand the interfacial reaction, in order to understand the mechanism and the kinetics of the reaction.

- By attempting a thermodynamic approach to the compound formation.

4. TEM examinations and analyses could be performed on the metal/ceramic interfaces to detect a potential reaction when not observed by SEM (for instance, detection of Mg base interfacial spinels in ZAS/Al-Mg systems)

5. Mechanical tests (e.g. shear test) must be performed in order to explore the metal/ceramic bonding strength in case of systems presenting chemically *clean* interfaces.

REFERENCES

1. K.G. Kreider, *Metal-Matrix Composites*, **4** 1-35 (1972).
2. I. Peychès, *Verres et Réfr.*, **22** [2] 127-140 (1968).
3. T.F. Cooke, *J. Am. Ceram. Soc.*, **74** [12] 2959-78 (1991).
4. H. Westengen, D.L. Albright, A. Nygard, *SAE Trans.*, **99** [5] 606-12 (1990).
5. A. Mortensen, J.A. Cornie, M.C. Flemings, *J. Met.*, **70** [2] 12-19 (1988).
6. F. Fulgar, W.H. Kreuger, J.G. Gorge, *Am. Ceram. Soc. meeting, Cocoa Beach*, (1984).
7. T. Donomoto, K. Funatani, N. Miura, N. Miyake, *SAE Technical Paper 830252, International Congress and exposition, Detroit*, (1983).
8. T.J. Reinhart, L.L. Clements, *Engineered Materials Handbook*, **1** 1-40 (1987).
9. R. Warren, *Metal Matrix Composites for High Temperature Structural Applications*, 233-255 (1988).
10. A.R. Bunsell, C. Bathias, A. Martrenchar, D. Menkes, *Advances in Composite Materials, Pergamon Press*, **2** (1980).
11. A. Kelly, W.R. Tyson, *Proceedings of the 2nd International Materials Symposium, California* (1964).
12. C. Zweben, *AIAA J.*, **6** (1968).
13. J.E. Masters, *Engineered Materials Handbook*, **1** 765-794 (1987).
14. R. Warren, C.H. Andersson, *Composites*, **15** [1] 101-112 (1984).
15. A.K. Dhingra, *Phil. Trans. R. Soc.*, **A294** 151 (1980).
16. P.J. Geoghegan, *57th Annual TRI/Princeton Conference*, (Apr. 21-22, 1987).
17. K.K. Chawla, *Composite Material Science and Technology*, Springer-Verlag (1987).
18. H. Morita, H. Yahane, Y. Kimura, T. Kitao, *J. Appl. Pol. Sci.*, **40** 753-767 (1990).
19. D. Duwez, R.H. Willens, W. Klement, *J. Appl. Phys.*, **31** (1960).
20. P. Rudkowski, G. Rudkowska, J.O. Strom-Olsen, *Mater. Sci. Eng.*, **A133** 158-161 (1991).
21. J.P. Rocher, F. Girot, J.M. Quessinet, R. Pailler, *Mémoires et Etudes Scientifiques Revue de Métallurgie*, [2] 69-78 (1986).

22. T.W. Chou, A. Kelly, A. Okura, *Composites*, 16 [3] 187-204 (1985).
23. W.L. Lachman, S.J. Paprocki, H.D. Batha, *Engineered Materials Handbook*, 1 848 (1987).
24. M.W. Toaz, *Engineered Materials Handbook*, 1 904-909 (1987).
25. S. Rajagopal, *J. Applied Metal Working*, 1 [4] 3-12 (1981).
26. Th. Young, *Phil. Trans. R. Soc.*, 95 65 (1805).
27. J. Frenkel, *J. Exp. Theor. Phys.*, 18 [7] 659 (1948).
28. J.W. Gibbs, *Trans. Conn. Acad.*, 3 343 (1878).
29. R.E. Johnson, *J. Phys. Chem.*, 63 1650-55 (1959).
30. M. Humenik, W.D. Kingery, *J. Am. Ceram. Soc.*, 37 [18] 18-23 (1954).
31. A.M. Armstrong, S.K. Misra, *J. Am. Ceram. Soc.*, 51 968 (1968).
32. D.A. Netzel, G. Hoch, T.I. Marx, *J. Colloid. Sci.*, 19 774 (1964).
33. I.A. Aksay, C.E. Hoge, J.A. Pask, *J. Phys. Chem.*, 78 [12] 1178-83 (1974).
34. D.T. Livey, P. Murray, *2nd Plansee Seminar, edited by F. Benesusky, Reutte, Austria*, 374-404 (1956).
35. J.T. Davies, E.K. Rideal, *Interfacial Phenomena, edited by Academic Press, N.Y.*, (1963).
36. J.A. Pask, *Ceram. Bull.*, 66 1587-92 (1987).
37. W.D. Kingery, *J. Am. Ceram. Soc.*, 36 [11] (1955).
38. A. Dupré, *Théorie Mécanique de la Chaleur, Gauthier-Villars, Paris* (1869).
39. J. A. Aksay, J.A. Pask, *J. Am. Ceram Soc.*, 58 [11-12] 465-552 (1975).
40. J. V. Naidich, *Prog. Surf. Mem. Sci., edited by D.A. Cadenhead and J.F. Danielli (Academic Press)*, 14 353-484 (1981).
41. L. Ramqvist, *J. Phys. Chem.*, 30 159-172 (1969).
42. K.C. Russel, J.A. Cornie, S-Y. Oh, *Metall. Trans.*, 20A [3] 527-532 (1989).
43. J. Kinloch, *J. Mater. Sci.*, 15 2141-66 (1980).
44. P.R. Chidambaram, G.R. Edwards, D.L. Olson, *Met. Trans.*, 23B [4] 215-222 (1992).
45. J.J. Brennan, J.A. Pask, *J. Am. Ceram. Soc.*, 51 [10] 569-578 (1975).
46. C. Marumo, J. A. Pask, *J. Mat. Sci.*, 12 223-38 (1977).
47. R.E. Loehman, *Ceram. Bull.*, 68 [4] 891-896 (1989).
48. H.O. Olsen, C. Smith, E. Grittenden, *J. Appl. Phys.*, 16 405-411 (1954).
49. O.R. Pulliam, *J. Sci.*, [3] 31 (1957).
50. J.G. Li, D. Chatain, L. Coudurier, N. Eustathopoulos, *J. Mater. Sci. Lett.*, 7 961-963 (1988).
51. P.H. Brace, *J. Electrochem. Soc.*, 94 170 (1948).
52. A. Bondi, *Chem. Rev.*, 52 [2] 417-421 (1953).
53. W.D. Kingery, *J. Am. Ceram. Soc.*, 37 [2] 1-42 (1954).
54. G.A. Halden, W.D. Kingery, *J. Phys. Chem.*, 59 [6] 554-557 (1956).
55. W. Armstrong, A.C.D. Chaklader, *J. Am. Ceram. Soc.*, 45 [9] 407 (1962).
56. W.A. Weyl, *Structure and Properties of Solid Surfaces, University of Chicago Press* (1953).
57. A. Banerji, P. K. Rohatgi, W. Reif, *Metall.*, 38 [7] 656-61 (1984).
58. R.D. Carnahan, L.T. Johnson, C.H. Li, *J. Am. Ceram. Soc.*, 41 [9] 341-347 (1958).
59. J.J. Brennan, J.A. Pask, *J. Am. Ceram. Soc.*, 51 569-573 (1968).
60. J.A. Champion, B.J. Keene, J.M. Sillwood, *J. Mater. Sci.*, 4 39-49 (1969).
61. L. Coudurier, J. Adorian, D. Pique, N. Eustathopoulos, *Rev. Int. Hautes Temp. Réfr.*, 21 81-93 (1984).
62. H. John, H. Hausner, *J. Mater. Sci. Let.*, 5 549-551 (1986).
63. J.G. Li, H. Hausner, *J. European Ceram. Soc.*, [9] (1992).
64. K. Rhee, *J. Am. Ceram Soc.*, 54 [6] 332-334 (1971).
65. R. Dettre, R.E. Johnson, *Contact Angle, Wettability and Adhesion, edited by R.F. Gould, Am. Chem. Soc.*, 136-144 (1964).
66. J.F. Oliver, S.G. Mason, *J. Mater. Sci.*, 15 431-437 (1980).
67. W.A. Zisman, *pp. 1-51 in Ref. 65.*
68. S.K. Rhee, *J. Am. Ceram. Soc.*, 53 386-89 (1970).
69. F. Delannay, L. Frozen, A. Deryttere, *J. Mater. Sci.*, 22 1-16 (1987).

70. J.A. Pask, R.M. Fulrath, *J. Am. Ceram. Soc.*, 42 [12] 592-596 (1962).
71. C.R. Manning, T.B. Gurganus, *J. Am. Ceram. Soc.*, 52 [3] 115-118 (1969).
72. N. Eustathopoulos, J.C. Joud, P. Desdre, J.M. Hicter, *J. Mater. Sci.*, 9 1233-42 (1974).
73. B.F. Quigley, G.J. Abbaschian, R. Wunderlin, *Metall. Trans.*, 13A 53-99 (1982).
74. B.C. Pai, S. Rai, K.V. Prabhakar, P.K. Rohatgi, *Mater. Sci. Eng.*, 24 31 (1976).
75. T.P. Murali, M.K. Surrappa, P.K. Rohatgi, *Metall. Trans.*, 13B 31 (1982).
76. F.A. Halden, W.D. Kingery, *J. Phys. Chem.*, 59 [6] (1956).
77. P.K. Rohatgi, B.C. Pai, S.C. Panda, *J. Mater. Sci.*, 14 2227 (1979).
78. C. Garcia-Cordovilla, E. Louis, A. Pamies, *J. Mater. Sci.*, 21 2787-92 (1986).
79. A. Banerji, P.K. Rohatgi, *J. Mater. Sci.*, 17 335 (1982).
80. A. Munitz, M. Metzger, *Met. Trans.*, 10A 697 (1979).
81. B. Hallstedt, Z. K. Liu, J. Agren, *Mat. Sci. Eng.*, 58 183 (1990).
82. J.A. Cornie, A. Mortensen, M.C. Flemmings, *ICCM6/ECCM2 Conf., London*, 2 297-344 (1987).
83. F. Bashforth, S.C. Adams, *An Attempt to Test Theories of Capillarity, Cambridge University Press, London* (1883).
84. B.S. Ellefson, N.W. Taylor, *J. Am. Ceram. Soc.*, 21 [6] 193-213 (1938).
85. N.E. Dorsey, *Ceram. Abstr.*, 8 (1929).
86. J. Guastalla, *Bull. Soc. Chim.*, 3211 (1970).
87. A.I. Kingon, R.F. Davis, M.M. Thackeray, *ASM Engineered Materials Handbook*, 4 758-775 (1991).
88. C.T. Lynch, *Handbook of Material Science, CRC Press*, 2 (1971).
89. Y. Shiraki, *Fine Ceramics: Sintered Ceramics 4, Gihodo* (1976).
90. Engineering Property Data on Selected Ceramics, *MCIC Report, Batelle Lab.* (1981).
91. A.H. Heuer, L.K. Lenz, *J. Am. Ceram. Soc.*, 192 (1982).
92. R.M. McMeeking, A.G. Evans, *J. Am. Ceram. Soc.*, 65 [5] 949-954 (1982).
93. A.G. Evans, R.M. Cannon, *Acta Metall.*, 34 [5] 949-954 (1986).
94. A.G. Evans, *Advances in Ceramics*, edited by N. Claussen, M. Ruhle, H. Heuer, Am. Ceram. Soc., 12 193-212 (1983).
95. W.S. Young, I.B. Cutler, *J. Am. Ceram. Soc.*, 53 [12] 659-63 (1970).
96. J. Wang, R. Raj, *J. Am. Ceram. Soc.*, 73 [5] 1172-75 (1990).
97. S. Kraus, A.H. Heuer, T.E. Mitchell, *J. Am. Ceram. Soc.*, 68 [12] back cover (1985).
98. P. Pilate, F. Cambier, *Journal de Physique*, 47 col.C1 (1986).
99. T. Ando, Y. Shiohara, *J. Am. Ceram. Soc.*, 74 [2] 410-417 (1991).
100. B.H. Mussler, M.W. Shafer, *J. Am. Ceram. Soc.*, 70 [10] 699-704 (1987).
101. Y. Ohya, Z. Nakagawa, *J. Am. Ceram. Soc.*, 73 [11] 3476-80 (1990).
102. F.J. Parker, *J. Am. Ceram. Soc.*, 73 929 (1990).
103. H.A.J. Thomas, R. Steven, E. Gilbart, *J. Mat. Sci.*, 26 3613-16 (1991).
104. F.F. Lange, *J. Mater. Sci.*, 17 240 (1982).
105. Y. Shindo, W.C. Moffat, H.K. Bowen, *Mater. Sci. Let.*, 10 [1-2] 79-83 (1990).
106. M.I. Osendi, B.A. Bender, D. Lewis, *Adv. Ceram. Mater.*, 3 [6] 563-68 (1988).
107. M.I. Osendi, J.S. Moya, *J. Mater. Sci. Let.*, 7 [1] 15-18 (1988).
108. R.F. Davis, J.A. Pask, *J. Am. Ceram. Soc.*, 55 525 (1972).
109. P.C. Dokko, J.A. Pask, K.S. Mazdiyasni, *J. Am. Ceram. Soc.*, 60 150 (1977).
110. D.L. Porter, A.H. Heuer, *J. Am. Ceram. Soc.*, 60 183 (1977).
111. F.F. Lange, *J. Mater. Sci.*, 17 235-239 (1982).
112. J.S. Moya, M.I. Osendi, *J. Mater. Sci.*, 19 2909-2914 (1984).
113. Q.M. Yuan, J.Q. Tan, Z.G. Jin, *J. Am. Ceram. Soc.*, 19 [3] 265-267 (1984).
114. E. Di Rupo, E. Gilbart, T.G. Carruthers, R.J. Brook, *J. Mater. Sci.*, 14 705-711 (1979).
115. E. Di Rupo, T.G. Carruthers, *J. Am. Ceram. Soc.*, 61 468 (1978).
116. N. Claussen, J. Jahn, *J. Am. Ceram. Soc.*, 63 [3-4] 228-229 (1980).
117. E. Di Rupo, M.R. Anseau, *J. Mater. Sci.*, 15 114-118 (1980).
118. M. Yoshimura, M. Kaneko, S. Somiya, *Journal de Physique*, 47 [2] C1-473 (1986).
119. M. Nogami, K. Nagasaka, *J. Mater. Sci.*, 26 3665-69 (1991).

120. I. M. Low, R. McPherson, *J. Mater. Sci.*, 24 1648-52 (1989).
121. C.N. Cochran, W.C. Sleppy, J. Electrochem. Soc., 108 [4] 322-327 (1961).
122. D.J. Green, *J. Am. Ceram. Soc.*, 65 610 (1982).
123. A.S. Berezhnoi, N.V. Gul'ko, *Dopovidi Akad. Nauk Ukr. R.S.R.*, 1 [78] (1955).
124. T. Noguchi, M. Mizuno, *Bull. Chem. Soc. Jap.*, 41 [12] 2838 (1968).
125. M.R. Anseau, J.P. Bilodeque, P. Fierens, *J. Mater. Sci.*, 11 578 (1976).
126. J.A. Champion, B.J. Keene, J.M. Sillwood, J. Mater. Sci., 4 39-49 (1969).
127. W.W. Smeltzer, *J. Electrochem. Soc.*, 103 [2] 67-71 (1958).
128. R.J. Kematick, H.F. Franzen, *J. Solid State Chem.*, 54 226-234 (1984).
129. J.A. Isaacs, F. Taricco, V.J. Michaud, A. Mortensen, *Met. Trans.*, 22A 2855-62 (1991).